# THE ROLES OF AUGMIN AND SPINDLE ACTIN IN CHROMOSOME CONGRESSION, SPINDLE ARCHITECTURE AND MITOTIC FIDELITY

**Štimac, Valentina**

**Doctoral thesis / Doktorski rad**

**2024**

University of Zagreb

FACULTY OF SCIENCE
DEPARTMENT OF BIOLOGY

Valentina Štimac

# THE ROLES OF AUGMIN AND SPINDLE ACTIN IN CHROMOSOME CONGRESSION, SPINDLE ARCHITECTURE AND MITOTIC FIDELITY

DOCTORAL THESIS

Zagreb, 2024.

Sveučilište u Zagrebu

PRIRODOSLOVNO-MATEMATIČKI FAKULTET

BIOLOŠKI ODSJEK

Valentina Štimac

# ULOGE AUGMINA I AKTINA UNUTAR DIOBENOG VRETENA U KONGRESIJI KROMOSOMA, ARHITEKTURI VRETENA I VJERNOSTI MITOZE

DOKTORSKI RAD

Zagreb, 2024.

This work was done in the Laboratory of Cell Biophysics at the Ruđer Bošković Institute, Zagreb, under the supervision of Iva M. Tolić, PhD, Full Professor and Head of Laboratory. As a part of the Postgraduate doctoral programme in Biology, this thesis is submitted for review to the Department of Biology at the Faculty of Science, University of Zagreb, in order to achieve the academic degree Doctor of Biology.

## Supervisor biography

Professor Iva M. Tolić was born in Zagreb, Croatia. She graduated Molecular biology at Faculty of Science, University of Zagreb, Croatia in 1996. During graduate studies, Prof Tolić worked as research assistant in the group of Prof Nenad Trinajstić at Ruđer Bošković Institute. Her PhD work was done with Prof Ning Wang at Harvard School of Public Health, Boston, MA, USA. She achieved the academic degree Doctor of biology at University of Zagreb in 2002. After this, she worked as a postdoctoral fellow with Prof Kirstine Berg-Sørensen at Niels Bohr Institute, Copenhagen, Denmark, and later with Prof Francesco Pavone at European Laboratory for Non- Linear Spectroscopy, Florence, Italy. From 2005 to 2014, Prof Tolić worked as a research group leader at Max Planck Institute of Molecular Cell Biology and Genetics in Dresden, Germany. Her research areas are mitosis, mitotic spindle mechanics, microtubules, motor proteins and aneuploidy. Currently she is a Senior Research Group Leader with tenure at Ruđer Bošković Institute (RBI) in Zagreb. Professor Tolić has received 16 research grants including prestigious projects funded by the European Research Council (ERC), Consolidator and Synergy. She has published more than 100 papers in peer-reviewed journals including Nature, Science, Cell, and Nature Cell Biology, cited more than 4500 times, and served as a reviewer for these and various other journals. To this date, she has mentored 15 PhD and 24 Master theses. Professor Tolić has been elected member of Academia Europaea (since 2022), an elected associate member of the Croatian Academy of Sciences and Arts – HAZU (since 2020) and an elected member of the European Molecular Biology Organization – EMBO (since 2018). She received numerous awards such as the Ignaz Lieben Award of the Austrian Academy of Sciences, the European Biophysical Societies Association (EBSA) Young Investigators' Medal and Prize, the Outstanding Paper Award of the European Microscopy Society in the category Life Sciences and National Science Award of the Republic of Croatia. As an invited speaker, she has participated in more than 150 conferences and research seminars worldwide. She organized several scientific meetings including the EMBO Conference on Meiosis (2017) and Mitotic spindle: From living and synthetic systems to theory (2019, 2021 and 2023).

# Acknowledgments

*First, I would like to express my sincere gratitude to my mentor, Iva Tolić, for giving me the opportunity to be part of her research group. I am deeply thankful for her guidance and for showing me the true values every scientist should aspire to.*

*I would also like to thank all the committee members for reading my thesis and providing valuable feedback that improved it.*

*Special thanks to Isabella Koprivec for working and tackling the challenges of various projects together with me during the last five years. Big thanks to all my office members, past and present, who became my friends during this journey. Thank you all for the scientific discussions, celebrations, hiking trips and gatherings. I would also like to thank all members of the Tolić and Pavin groups who participated in the scientific discussions over these past five years.*

*I would like to thank everyone who has inspired me to take a scientific career during my time at university. Special thanks to Nikolina, who showed me the first steps in cell culture and was always there when things did not go as planned. I would also like to thank Ljerka, who always found a way to make us smile during challenging scientific situations in our careers.*

*The biggest gratitude goes to my family for the unconditional love and support throughout all these years. Big thanks to my "small circle of great people", you know who you are, for believing in me and hyping me to always follow my dreams. Your belief in me has shaped me into the person I am today, and because of you all, I know that anything is possible.*

*Finally, I would like to thank L'Oréal ADRIA and the Croatian Commission for UNESCO at the Ministry of Culture and Media for recognizing the importance of my scientific work and rewarding me with the L'Oréal-UNESCO "For Women in Science" national fellowship in 2024.*

University of Zagreb Doctoral thesis

Faculty of Science

Department of Biology

# THE ROLES OF AUGMIN AND SPINDLE ACTIN IN CHROMOSOME CONGRESSION, SPINDLE ARCHITECTURE AND MITOTIC FIDELITY

VALENTINA ŠTIMAC

Ruđer Bošković Institute

The human mitotic spindle is made of microtubules nucleated at centrosomes, at kinetochores, and from pre-existing microtubules by the augmin complex. Recently, spindle actin also emerged as a possible player in spindle assembly. However, it is unknown how augmin-mediated nucleation affects distinct microtubule classes, what the spatial distribution of spindle actin and microtubules is, and, finally, what the roles of these two proteins are in spindle architecture and mitotic progression. Here, by using superresolution microscopy and cutting edge live-cell imaging, I found that augmin promotes mitotic fidelity by generating assemblies consisting of bridging and kinetochore fibers that align sister kinetochores to face opposite poles, thereby preventing erroneous attachments. Furthermore, I showed that spindle actin, by forming fine filaments in the polar region and along spindle microtubules, promotes spindle pole focusing and bipolar cell division.

(125 pages, 48 figures, 0 tables, 187 references, original in English)

Keywords: mitotic spindle, augmin, spindle actin, microtubule nucleation, chromosome congression, chromosome segregation

Supervisor: Iva M. Tolić, PhD, Full Professor and Head of Laboratory

Reviewers: Andreja Ambriović Ristov, PhD, Full Professor and Head of Laboratory

Alexey Khodjakov, PhD, Research Scientist and Adjunct Professor

Maja Matulić, PhD, Full Professor

Sveučilište u Zagrebu Doktorski rad

Prirodoslovno-matematički fakultet

Biološki odsjek

# ULOGE AUGMINA I AKTINA UNUTAR DIOBENOG VRETENA U KONGRESIJI KROMOSOMA, ARHITEKTURI VRETENA I VJERNOSTI MITOZE

VALENTINA ŠTIMAC

Institut Ruđer Bošković

Mikrotubuli diobenog vretena se u ljudskim stanicama nukleiraju na centrosomu, kinetohorama te na površini već postojećih mikrotubula pomoću augminskog kompleksa. Nedavno je predloženo da i aktin unutar diobenog vretena ima ulogu u njegovom sastavljanju. Međutim, još uvijek nije poznato na koji način nukleacija pomoću augmina utječe na različite klase mikrotubula, koja je prostorna raspodjela aktina i mikrotubula unutar vretena te koja je uloga ova dva proteina u arhitekturi vretena i progresiji mitoze. Koristeći superrezolucijsku mikroskopiju te najnoviju tehnologiju snimanja živih stanica pokazala sam da augmin ima ulogu u pravilnoj podjeli kromosoma. Augmin stvara sklopove mikrotubula koji se sastoje od premošćujućih i kinetohornih vlakana što poravnava sestrinske kinetohore na način da su okrenute prema suprotnim polovima, te tako sprječava pogrešna vezanja s mikrotubulima. Nadalje, pokazala sam da aktin unutar vretena promiče fokusiranje polova vretena te bipolarnu mitozu tako što formira filamente u polarnoj regiji te uzduž mikrotubula.

(125 stranica, 48 slika, 0 tablica, 187 referenci, jezik izvornika engleski)

Ključne riječi: diobeno vreteno, augmin, aktin unutar vretena, nukleacija mikrotubula, kongresija kromosoma, podjela kromosoma

Mentor: prof. dr. sc. Iva M. Tolić, voditeljica laboratorija i znanstvena savjetnica u trajnom zvanju

Ocjenjivači: prof. dr. sc. Andreja Ambriović Ristov, voditeljica laboratorija i znanstvena savjetnica u trajnom zvanju

prof. dr. sc. Alexey Khodjakov, znanstveni suradnik

prof. dr. sc. Maja Matulić

# Table of contents

# 1. INTRODUCTION

The mitotic spindle has a sophisticated architecture that enables it to accurately segregate chromosomes during cell division. It consists of three major classes of microtubules: kinetochore microtubules that form kinetochore fibers (k-fibers) connecting chromosomes to the spindle pole through kinetochores, midplane-crossing microtubules that form antiparallel arrays in the central part of the spindle, and astral microtubules that extend from the spindle poles towards the cell cortex (McIntosh, 2016; O'Toole et al., 2020; Prosser and Pelletier, 2017). During metaphase and early anaphase, the majority of midplane-crossing microtubule bundles are laterally attached to a pair of sister k-fibers resembling a bridge between them, which is why they are called bridging fibers (Kajtez et al., 2016; Vukušić et al., 2017). These fibers balance the tension between sister kinetochores and maintain the curved shape of the metaphase spindle (Kajtez et al., 2016; Polak et al., 2017; Tolić and Pavin, 2016). In addition to linking sister k-fibers, some midplane-crossing microtubules can also form connections between neighboring k-fibers (O'Toole et al., 2020).

Spindle microtubules in human somatic cells are generated by several nucleation mechanisms, including centrosome-dependent and augmin-dependent nucleation (Kirschner and Mitchison, 1986; Pavin and Tolić, 2016; Petry, 2016; Prosser and Pelletier, 2017; Wu et al., 2008; Zhu et al., 2008), with an addition of chromatin- and kinetochore-dependent nucleation as the third mechanism that contributes to the directional formation of k-fibers (Maiato et al., 2004; Sikirzhytski et al., 2018; Tulu et al., 2006). Centrosome-dependent nucleation was long thought to be predominant in spindle assembly; however, numerous studies revealed that a significant number of microtubules also arise from pre-existing microtubules, through augmin, an eight-subunit protein complex that serves as a recruiter of the γ-tubulin ring complex (γ-TuRC) required for microtubule nucleation (David et al., 2019; Goshima et al., 2008; Kamasaki et al., 2013; Lawo et al., 2009; Song et al., 2018; Uehara et al., 2009). Augmin-nucleated microtubules grow at an angle of 0-30° relative to the pre-existing microtubule (Kamasaki et al., 2013; Petry et al., 2013; Verma and Maresca, 2019) and show a directional bias towards kinetochores, resulting in the preserved polarity of the spindle once the initial kinetochore-microtubule attachments form (David et al., 2019; Kamasaki et al., 2013). Depletion of augmin complex in different cell types results in impairment of microtubule bundles within the spindle accompanied by the formation of long, curved bundles on the spindle periphery, loss of spindle bipolarity, shorter interkinetochore distance, chromosome misalignment, mitotic delays, and a higher incidence of aneuploidy and cytokinesis failure (Almeida et al., 2022; Hayward et al., 2014; Uehara et al., 2009; Uehara and Goshima, 2010; Wu et al., 2008; Zhu et al., 2008). Of the eight subunits in the complex, the two directly interacting subunits HAUS6 (hDgt6/FAM29A) and HAUS8 (hDgt4/Hice1) have been extensively studied because of their ability to interact with a γ-TuRC adapter protein NEDD1 and pre-existing microtubules, respectively (Song et al., 2018; Uehara et al., 2009). While previous studies mainly focused on the effect of augmin on astral and kinetochore microtubules, the effect on midplane-crossing microtubules remains largely unexplored (Almeida et al., 2022; Hayward et al., 2014; Song et al., 2018; Uehara et al., 2016, 2009; Uehara and Goshima, 2010; Wu et al., 2008; Zhu et al., 2008). Recent electron tomography work on spindles in human cells showed that ends of midplane-crossing microtubules interact with the wall of kinetochore microtubules (O'Toole et al., 2020), indicating that augmin-dependent nucleation might play an important role in their formation.

Augmin depletion has previously been linked to higher incidence of segregation errors (Wu et al., 2008) and the appearance of lagging chromosomes (Almeida et al., 2022; Viais et al., 2021), which were connected to impaired brain development in a recent study (Viais et al., 2021). Homozygous loss of HAUS6 subunit of the augmin complex was also seen in several cancer types, such as sarcomas, pancreatic adenocarcinomas, gliomas, and glioblastomas (ICGC/TCGA, 2020, retrieved by using cBioPortal (Cerami et al., 2012; Gao et al., 2013)). However, the origin of segregation errors in augmin depletion remains largely unexplored due to extensive mitotic delays often experienced by these cells (Wu et al., 2008).

Actin filaments have long been proposed to play a role in centrosome separation, spindle positioning, orientation, and assembly (Dogterom and Koenderink, 2019; Uzbekov et al., 2002; Whitehead et al., 1996). There are at least 5 distinct actin structures present during mitosis – cortical actin that forms a network with other proteins right below the plasma membrane (di Pietro et al., 2016), retraction fibers that extend from the cytoplasm and provide a link to the areas with strong cell-substrate adhesion (Mitchison, 1992; Théry et al., 2005; Théry and Bornens, 2006), subcortical actin clouds that organize in response to retraction fibers and revolve along the cell cortex (Kwon et al., 2015; Mitsushima et al., 2010), and a newly discovered perinuclear (Booth et al., 2019; Plessner et al., 2019) and spindle actin (Kita et al., 2019; Plessner et al., 2019). The importance of actin during early mitosis was confirmed in experiments using latrunculin, as actin depolymerisation resulted in a reduced distance between centrosomes and a prolonged prometaphase (Uzbekov et al., 2002). However, many of processes during early mitosis depend not only on the presence of actin, but also on the activity of myosin II or myosin X which play distinct and important roles (Rosenblatt et al., 2004; Toyoshima and Nishida, 2007).

It was recently observed that spindle actin precedes k-fibers during their growth (Plessner et al., 2019). At the time of its formation throughout prometaphase, spindle actin has been found to concentrate around the poles, with some interpolar actin bundles extending from pole to pole (Kita et al., 2019). Centrosomes were also recognized as actin organizing centers where the assembly of actin filaments is induced in response to Arp2/3 (nucleating factor that enables actin branching) recruitment to the centrosome with actin filaments density regulated by the levels of cellular adhesion (Farina et al., 2016). A higher level of cell adhesion causes a decreased availability of actin monomers at the centrosome, resulting in lower density of centrosomal actin and higher density of microtubules (Inoue et al., 2019). While myosin activity in these processes remains largely unexplored, the ability of myosin X to bind to actin (Homma et al., 2001), microtubules (Weber et al., 2004) and spindle assembly factors, such as TPX2 (Woolner et al., 2008), make it a potential candidate for modulation of actin-microtubule interactions during spindle assembly (Woolner et al., 2008).

Recently, the role of spindle actin and the Arp2/3 complex was also proposed in chromosome congression, as different Arp2/3 complex inhibitors slowed down and disordered the process of chromosome congression, ultimately resulting in a dissipated chromosome organization and mitotic defects (Plessner et al., 2019). Myosin-II mediated contraction of perinuclear actin, located at the nuclear envelope prior to prometaphase, also showed a role in the congression of chromosomes situated outside the spindle area at NEBD (Booth et al., 2019). However, these mechanisms were just recently discovered, and the exact extent of their contribution in congression and spindle assembly remains to be explored.

The main objective of this study is to explore the role of augmin complex in the formation and maintenance of spindle microtubules, as well as the role of augmin and spindle actin in the process of chromosome congression and segregation. The study will investigate the relative contribution of the augmin complex to the nucleation of distinct spindle microtubules. Additionally, it will determine the spatial distribution of actin filaments with respect to bridging and k-fibers. The central hypothesis is that augmin and actin are involved in nucleation and establishing the architecture of distinct microtubule classes, thereby ensuring proper congression of chromosomes during prometaphase, spindle architecture during metaphase, and consequently, accurate chromosome segregation during anaphase.

To explore the relative contribution of augmin complex in nucleation of distinct spindle microtubules and precise spatial distribution of microtubules and actin filaments within the spindle, new protocols for superresolution microscopy will be developed. Furthermore, cutting-edge live cell microscopy techniques will be used to investigate the dynamic processes of chromosome congression during prometaphase and chromosome segregation during anaphase. This research will give deeper insight into the role of augmin along with the spindle actin from the largely unexplored process of prometaphase until chromosome segregation in anaphase.

# 2. RESEARCH OVERVIEW

## 2.1. Mitosis

### 2.1.1. Cell cycle

The cell cycle is a process in which cell duplicates and ultimately segregates chromosomal DNA, resulting in two genetically identical daughter cells. It can be divided in four precisely regulated and distinct phases – G1 (gap 1), S (synthesis), G2 (gap 2) and M (mitosis) (Figure 1). In the G1 phase cell grows and synthesizes molecules needed for DNA replication. After that, cell duplicates its genetic material in the S phase and prepares for division in the G2 phase. Finally, in the M phase, the cell is in mitosis and equally distributes genetic material into two daughter cells. The cell cycle lasts around 24 hours in human cells, with interphase (G1, S and G2 phases) that takes 23 hours and mitosis that lasts around 1 hour (Alberts et al., 2015).

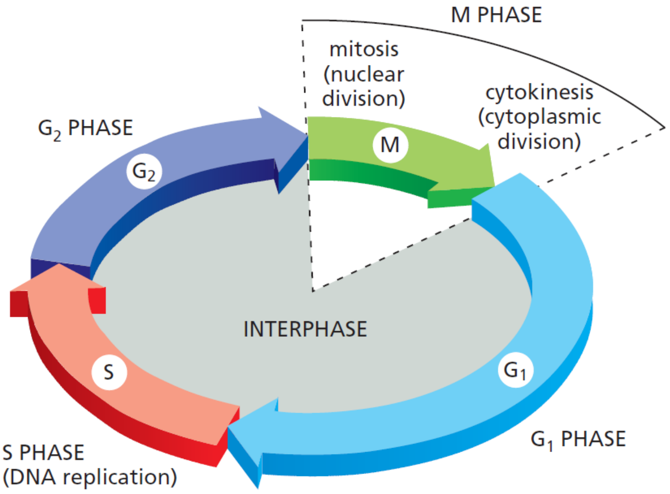

**Figure 1**. **The cell cycle phases.** The cell cycle is divided into two phases: interphase (consisting of G1, S and G2 phase) and M phase (comprise of mitosis and cytokinesis). In interphase, the cell prepares for mitosis and duplicates its genetic material. In M phase, the cell first undergoes nuclear division and then cytoplasmic division, which results in two genetically identical daughter cells. Taken from (Alberts et al., 2015).

### 2.1.2. Mitotic phases

The main goal of mitosis is to separate duplicated DNA into two daughter cells. To achieve that, the cell needs to build mitotic spindle that captures all chromosomes and aligns them between the two spindle poles to subsequently segregate duplicated genetic material. Based on chromosome behaviour and spindle morphology, mitosis can be divided into five distinct phases: prophase, prometaphase, metaphase, anaphase and telophase (Walczak et al., 2010) (Figure 2).

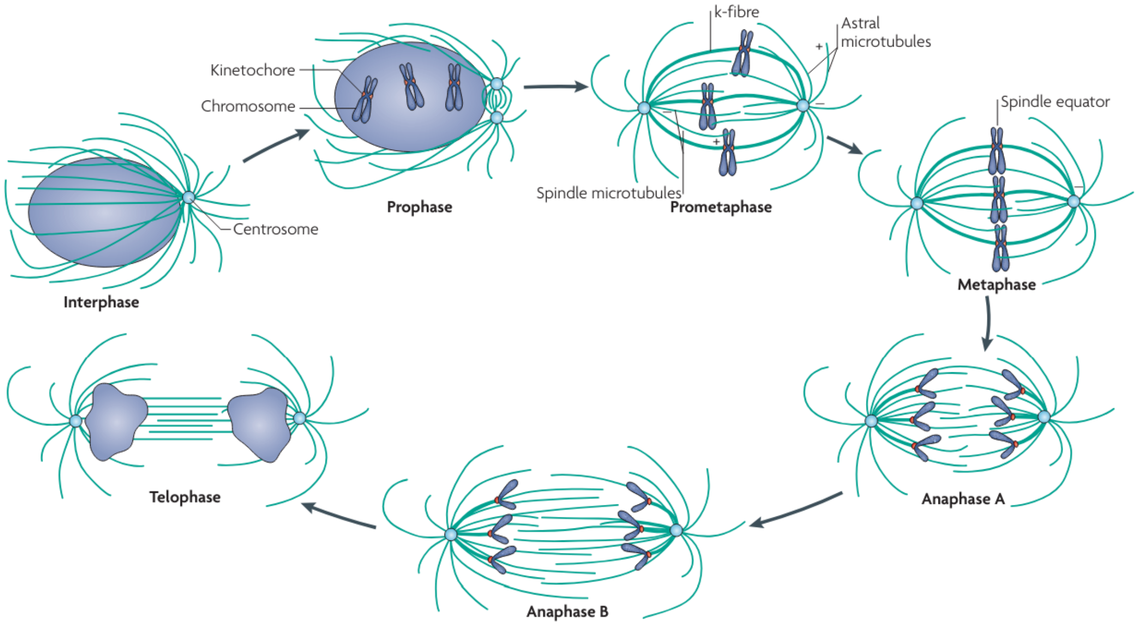

**Figure 2. The phases of mitosis.** Mitosis can be divided into five phases: prophase, prometaphase, metaphase, anaphase and telophase. In interphase, which precedes mitosis, cells duplicate their genetic material. Prophase is characterized by chromosome condensation and formation of kinetochores. Kinetochores are captured by microtubules in prometaphase and spindle starts to assemble. Metaphase represents a phase when all chromosomes are aligned at the spindle equator. When all kinetochore-microtubule attachments are properly formed, anaphase A (segregation of chromosomes) and B (segregation of spindle poles) start. In telophase chromosomes are decondensed and nuclear envelope reassembles. Taken from (Walczak et al., 2010).

The onset of mitosis is characterized by chromosome condensation, reorganization of interphase microtubules and separation of duplicated centrosomes during prophase. Microtubules start to gradually appear on centrosomes that will become two spindle poles during later mitotic phases (Prosser and Pelletier, 2017). Kinetochores, protein complexes that attach to microtubules, are assembled at the centromeric region of each sister chromatid (Musacchio and Salmon, 2007). Prometaphase starts when nuclear envelope breakdown (NEBD) occurs, which allows microtubules to search the space for chromosomes and attach to them via kinetochores (Kirschner and Mitchison, 1986). During prometaphase, bipolar mitotic spindle assembles and attached chromosomes congress towards the spindle equator between the two spindle poles. Their alignment at the equatorial plane of the mitotic spindle marks metaphase (Prosser and Pelletier, 2017). When all chromosomes are properly attached to the microtubules, spindle assembly checkpoint is satisfied, and anaphase starts (Cheeseman and Desai, 2008). First, during anaphase A, sister chromatids separate and later, during anaphase B, spindle poles move apart (Vukušić and Tolić, 2021). During telophase chromatids decondense and nuclear envelope reassembles. Lastly, the contractile ring divides cytoplasm and forms two daughter cells in a process that takes place during cytokinesis (Prosser and Pelletier, 2017).

### 2.1.3. Mitotic spindle architecture

During mitosis cell builds a mitotic spindle, a molecular macromachine that is composed of microtubules. Microtubules within the mitotic spindle can be divided into three classes that build up spindle's sophisticated structure required for accurate chromosome segregation (Figure 3). Kinetochore microtubules form k-fibers that connect chromosomes to the spindle pole through kinetochores. Interpolar microtubules form antiparallel arrays in the central part of the spindle, and the last class, astral microtubules, extend from the spindle poles towards the cell cortex (Prosser and Pelletier, 2017). During metaphase and early anaphase, interpolar microtubule bundles are laterally attached to a pair of sister k-fibers resembling a bridge between them, which is why they are called bridging fibers (Kajtez et al., 2016; Vukušić et al., 2017). These fibers balance the tension between sister kinetochores and maintain the curved shape of the metaphase spindle (Kajtez et al., 2016; Polak et al., 2017; Tolić and Pavin, 2016).

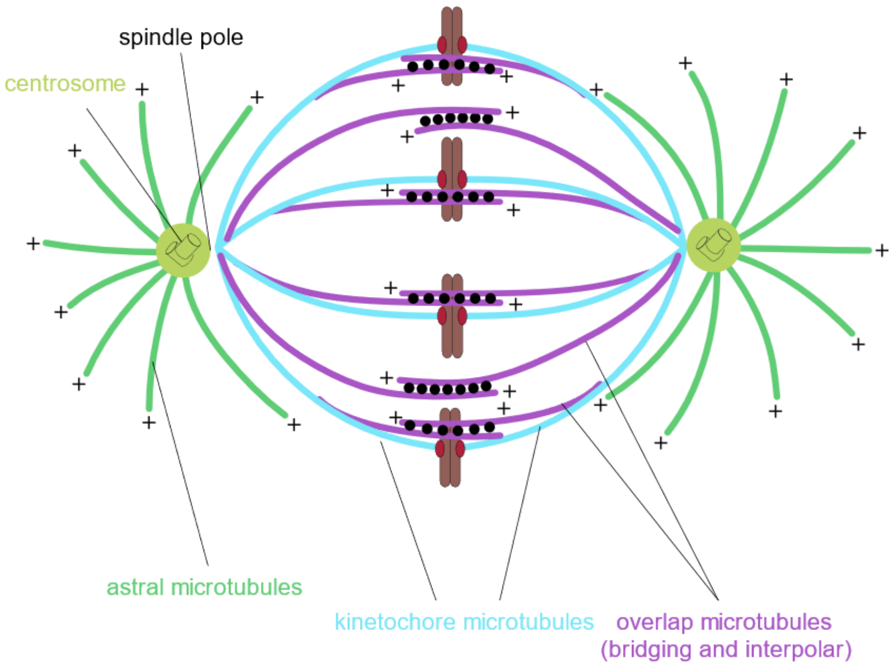

**Figure 3. Three classes of microtubules within the mitotic spindle.** Microtubules within the mitotic spindle can be divided into astral microtubules (green) that emanate from the spindle poles and extend towards the cell cortex. The second class of microtubules are kinetochore microtubules (blue) that attach to chromosomes via kinetochores and connect them with the spindle poles. Lastly, overlap microtubules (purple) make antiparallel arrays in the central part of the spindle (interpolar) or are laterally attached to a pair of sister k-fibers resembling a bridge between them (bridging fibers). Taken and modified form (Alberts et al., 2015).

### 2.1.4. Pathways of microtubule nucleation

Microtubules are composed of α- and β-tubulin dimers that are assembled in a GTP-dependent manner (Figure 4). Every tubulin subunit within a filament makes longitudinal contact, forming a protofilament, and lateral contact between the protofilaments to make a cylindrical structure of 13 protofilaments characteristic for microtubules (Kollman et al., 2011). Microtubules are polar structures with slow-growing minus ends and fast-growing plus ends that undergo constant polymerization and depolymerization cycles, which enables their growth and shrinkage. The γ-tubulin ring complex (γ-TuRC) is required for microtubule assembly within the cell (Prosser and Pelletier, 2017).

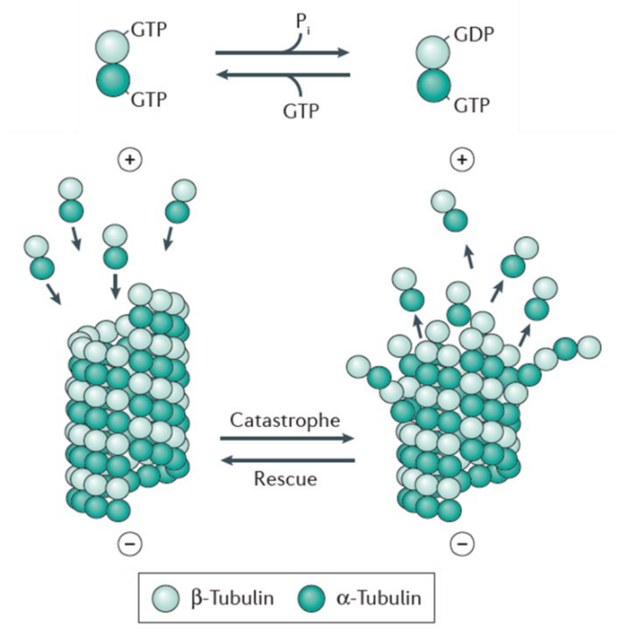

**Figure 4. GTP-dependent microtubule assembly.** Each tubulin subunit can bind one molecule of GTP. Since α-tubulin is trapped in the structure, only GTP on β-tubulin subunits can be hydrolysed to GDP and is more prone to depolymerization. During polymerization, β-tubulin subunits are in GTP-bound state. Microtubules dynamically switch between growing (rescue) and shrinking (catastrophe) phases. Taken from (Prosser and Pelletier, 2017).

Spindle microtubules in human cells are generated from the specific microtubule-organizing centers (MTOCs) that can be found at the centrosomes, chromosomes/kinetochores, and at the surface of existing microtubules (Khodjakov et al., 2003; Kirschner and Mitchison, 1986; Maiato et al., 2004; Petry, 2016; Sikirzhytski et al., 2018; Wu et al., 2008; Zhu et al., 2008) (Figure 5). Both centrosomal and acentrosomal pathways rely on γ-tubulin found in γ-TuRC complex and microtubule-based motors required to initiate microtubule nucleation and assemble bipolar spindle, respectively (Prosser and Pelletier, 2017).

Centrosome-dependent microtubule nucleation was long thought to be predominant contributor in microtubule generation since centrosomes were early recognized as the major MTOCs. Centrosomes are a complex of two centrioles surrounded with pericentriolar material that contains numerous proteins (including γ-tubulin) and sites required for microtubule nucleation (Conduit et al., 2015). Centrosomes generate microtubules that constantly polymerize and depolymerize and randomly search the space in the cell with the goal to make connections with chromosomes. This “search and capture model” was the first proposed mechanism for the spindle assembly in animal cells (Kirschner and Mitchison, 1986). Although this model remained the basis for the spindle assembly, it was soon demonstrated that it does not consider the barriers and positions of the chromosomes in real situations, as well as the number of chromosomes (Wollman et al., 2005). If only "search and capture model" was present during the spindle assembly, mitotic durations would be significantly longer than experimentally observed, suggesting that additional mechanisms must exist to facilitate the spindle assembly. The strong evidence suggesting that acentrosomal microtubule generation pathways are present in the cell was demonstrated when bipolar spindle assembled upon ablation of one or both centrosomes in the cell (Khodjakov et al., 2000). This experiment confirmed the speculations that acentrosomal pathways, seen previously in acentrosomal meiotic systems (Calarco-Gillam et al., 1983; Heald et al., 1996; Matthies et al., 1996), exist even in cells where centrosomes are normally present.

Chromosomes can also create environment favourable for microtubule generation and spindle assembly during prometaphase. Two distinct mechanisms are involved in microtubule generation near chromosomes - the Ras-related nuclear protein (Ran)GTP gradient and the chromosome passenger complex (CPC) (Carazo-Salas et al., 1999; Maresca et al., 2009; Sampath et al., 2004). During mitosis, RanGTP binds to importin-β which causes release of spindle assembly factors, where the most important one is a targeting protein for xklp2 (TPX2). TPX2 recruits Aurora A to the spindle, which is required for interaction and phosphorylation of γTuRC adaptor protein neural precursor cell-expressed developmentally down-regulated protein 1 (NEDD1). This cascade results in microtubule nucleation near the chromatin. The CPC consists of inner centrosome protein (INCENP), borealin, survivin and Aurora B kinase. Briefly, activation of Aurora B by autophosphorylation, promotes inactivation of microtubule-destabilizing proteins, such as mitotic centromere-associated kinesin (MCAK) and stathmin (STMN1) (Prosser and Pelletier, 2017). Kinetochores also serve as a site for microtubule nucleation. The experiments where k-fibers were ablated revealed that its regrow happened via microtubule plus-end polymerization at the kinetochore (Maiato et al., 2004). Dynein and CENP-E showed substantial role in this process, by capturing and incorporating distal ends of short k-fibers into the spindle and establishing end-on attachments on kinetochores, respectively (Khodjakov et al., 2003; Sikirzhytski et al., 2018).

The third pathway, which will also be a focus of this thesis, is microtubule-mediated microtubule nucleation. Numerous studies revealed that a significant number of microtubules arises near pre-existing microtubules, via augmin, an eight-subunit complex that serves as a recruiter of the γ-TuRC that is required for microtubule nucleation (David et al., 2019; Goshima et al., 2008; Kamasaki et al., 2013; Lawo et al., 2009; Song et al., 2018). Augmin-nucleated microtubules grow at an angle of 0-30° with the respect to the pre-existing microtubule (Kamasaki et al., 2013; Petry et al., 2013; Verma and Maresca, 2019). Depletion of augmin complex in different cell types results in impairment of microtubule bundles within the spindle accompanied by the formation of long, curved bundles on the spindle periphery, loss of spindle bipolarity, shorter interkinetochore distance, chromosome misalignment, mitotic delays, and a higher incidence of aneuploidy and cytokinesis failure (Almeida et al., 2022; Hayward et al., 2014; Uehara et al., 2009; Uehara and Goshima, 2010; Wu et al., 2008; Zhu et al., 2008), highlighting the role of acentrosomal spindle assembly in proper progression of mitosis.

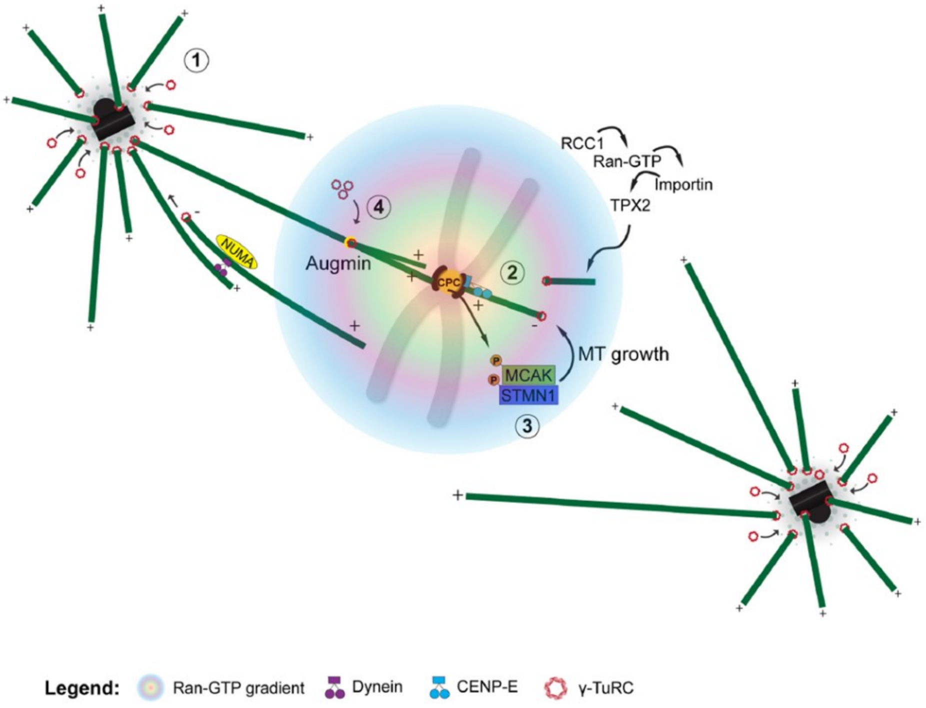

**Figure 5. Pathways of microtubule nucleation in the spindle.** Microtubules within the mitotic spindle can be nucleated at centrosomes (1), near chromosomes (2, 3) and along pre-existing microtubules with the help of augmin complex (4). Microtubules nucleated at centrosomes search the space to make attachments with kinetochores on chromosomes. Chromosome dependent nucleation depends on RanGTP gradient that activates proteins required for spindle assembly, or the chromosome passenger complex (CPC) that inactivates microtubule-destabilizing proteins. Microtubules nucleated from augmin grow at variety of angles making branched structure within the spindle. Taken from (Ferreira and Maiato, 2021).

### 2.1.5. Chromosome congression during prometaphase

After NEBD, chromosomes start to condense and move towards the spindle equator with the goal to align at the metaphase plate. This movement of chromosomes towards the spindle equator during prometaphase is called chromosome congression and happens concurrently with spindle assembly (Maiato et al., 2017). During congression, chromosomes attach to microtubules of the growing spindle and over time achieve biorientation, i.e. their kinetochores attach to microtubules coming from the opposite spindle poles (Figure 6). Spindle assembly checkpoint (SAC) delays anaphase onset and prevents premature segregation of incorrectly attached chromosomes (Joglekar, 2016).

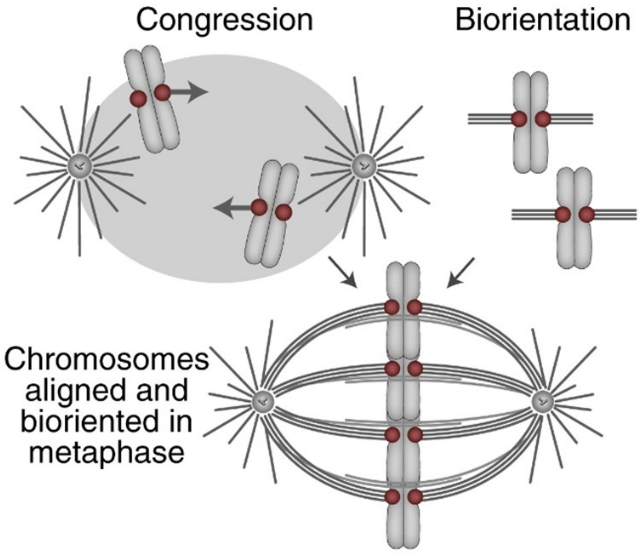

**Figure 6. Chromosome congression and alignment at the metaphase plate.** During prometaphase, chromosomes travel towards the spindle equator to align at the metaphase plate, a process called chromosome congression. During this time, chromosomes make attachments with microtubules while spindle assembles, and ultimately achieve biorientation and align at the metaphase plate. Taken from (Risteski et al., 2021).

The position of chromosomes with the respect to the two spindle poles defines which mechanism chromosomes will take to congress to the metaphase plate. Chromosomes positioned between the two poles at the beginning of mitosis (Figure 7), are already favourably positioned to achieve biorientation from separate poles and align to the metaphase plate (Vukušić and Tolić, 2022). The polymerization and depolymerization at the plus ends at kinetochore-microtubule attachments causes chromosome oscillations at the metaphase plate (Skibbens et al., 1993). On the other hand, peripheral polar chromosomes require well-coordinated action of different motors to first bring them towards the spindle pole and, once they reach the spindle, to congress them towards the spindle equator (Figure 8). Kinetochore dynein is required to bring peripheral polar chromosomes towards the spindle pole, while Centromere Protein E (CENP-E) takes over once chromosomes reach the spindle and helps in their biorientation required for congression towards the metaphase plate (Barisic et al., 2014; Kapoor et al., 2006; Li et al., 2007; Schaar et al., 1997; Vukusic and Tolic, 2024). Aurora A gradient at the poles ensures that no stable attachments happen prematurely, because that would impede congression of polar chromosomes (Barisic et al., 2014; Ye et al., 2015). Additionally, chromokinesins exert polar ejection forces that act on chromosome arms and move them away from the spindle poles. Those motors are well balanced with others to prevent chromosomes being randomly pushed away from the spindle during congression (Antonio et al., 2000; Barisic et al., 2014; Wandke et al., 2012).

A substantial role in chromosome congression have tubulin posttranslational modifications (PTMs) that navigate molecular motors. One of the PTMs, detyrosination, involves the removal of tyrosine at the C-terminal tail of α-tubulin by the enzymes tubulin carboxypeptidases (Aillaud et al., 2017; Nieuwenhuis et al., 2017). This modification can be reversed by the action of enzyme tubulin tyrosine ligase (Prota et al., 2013; Raybin and Flavin, 1975). It was demonstrated that this PTM is necessary for congression of peripheral polar chromosomes. Spindle microtubules are detyrosinated which has been proposed to serve as a navigation map for CENP-E to congress chromosomes towards the metaphase plate (Barisic et al., 2015).

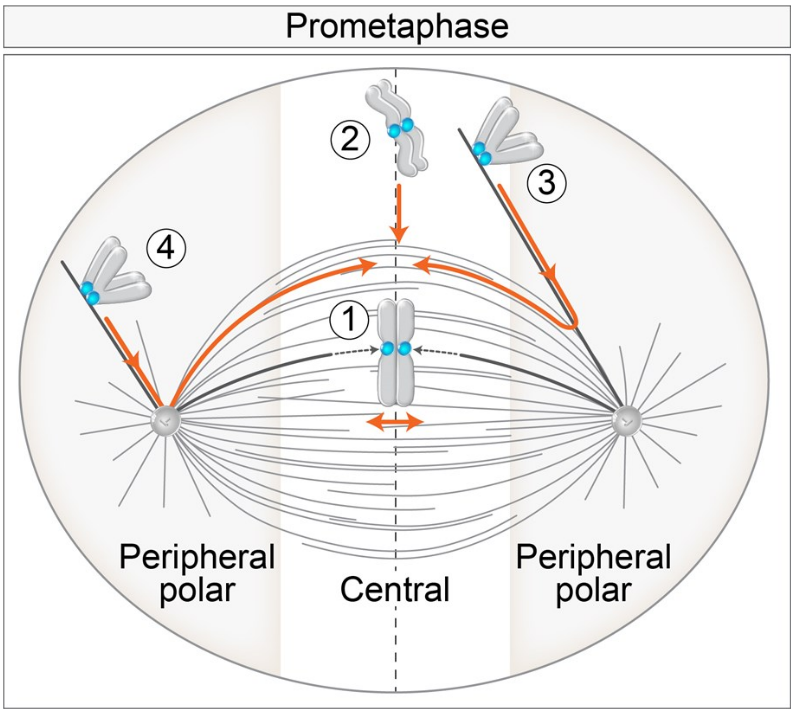

**Figure 7. Position of chromosomes during prometaphase with respect to the spindle poles.** Based on the chromosome's position with respect to the spindle poles, chromosomes can be divided into peripheral polar and central chromosomes. Central chromosomes are rapidly attached to microtubules from two poles and soon become bioriented and aligned at the metaphase plate (pathway 1). Central chromosomes located away from the nascent spindle are transported towards the spindle and then congress to metaphase plate (pathway 2 and 3). Lastly, peripheral polar chromosomes first need to take poleward movement and then subsequently travel towards the metaphase plate where they become bioriented (pathway 4). Taken from (Vukušić and Tolić, 2022).

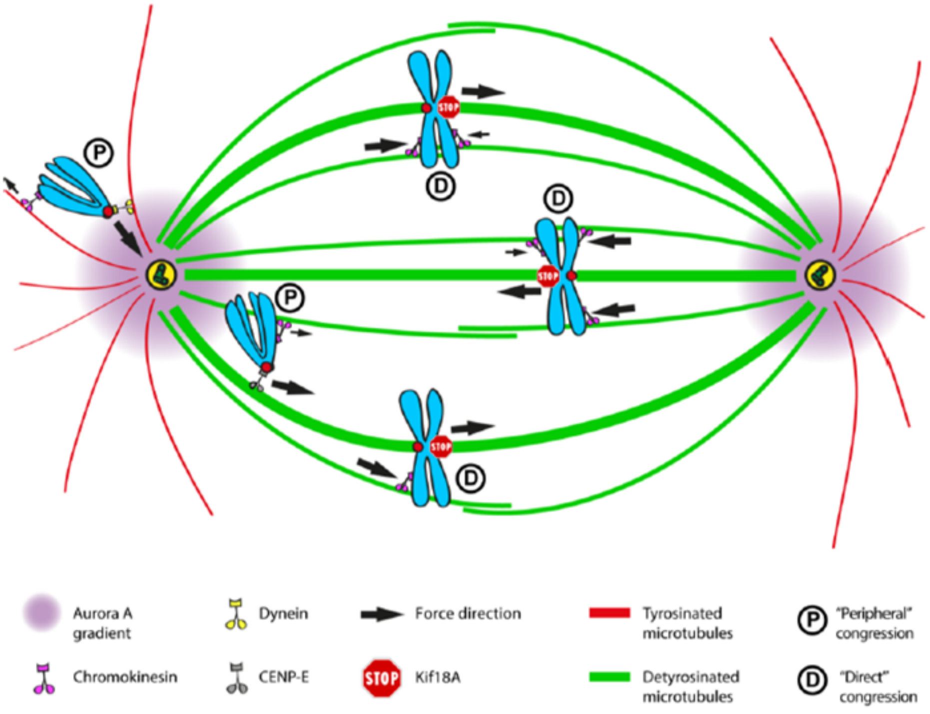

**Figure 8. Mechanisms involved in chromosome congression.** Central chromosomes (D) become rapidly bioriented and coordination of polar ejection forces together with microtubule dynamics and length at kinetochores cause chromosome oscillations at the metaphase plate. If chromosomes are positioned behind the pole (P), they first need to move poleward with the help of the minus-end directed motor dynein, probably along the tyrosinated microtubules. At the poles, Aurora A gradient prevents premature stabilization of kinetochore-microtubule attachments, which would impair their congression. Aurora A also phosphorylates CENP-E at the poles, that takes over and brings polar chromosomes to the metaphase plate along the detyrosinated microtubules. Chromokinesins exert polar ejection forces to the chromosome arms and are well balanced with other motors during congression. Taken from (Maiato et al., 2017).

### 2.1.6. Kinetochore-microtubule attachments and error correction

The ultimate goal of chromosome congression is to establish proper kinetochore-microtubule attachments required for a faithful segregation of chromosomes during anaphase. Microtubules attach to chromosomes on the region called centromere, which is defined by the H3 variant centromere protein A (CENP-A). During the cell cycle, constitutive centromere-associated network (CCAN) localizes to centromere and binds directly to CENP-A (McKinley et al., 2015). Inner kinetochore is assembled during mitosis and serves as a connection with the chromosomes (Figure 9). Outer kinetochore, that consists of KNL1–MIS12–NDC80 (KMN) complex, serves as an attachment site for microtubules where k-fibers are formed (Cheeseman et al., 2006).

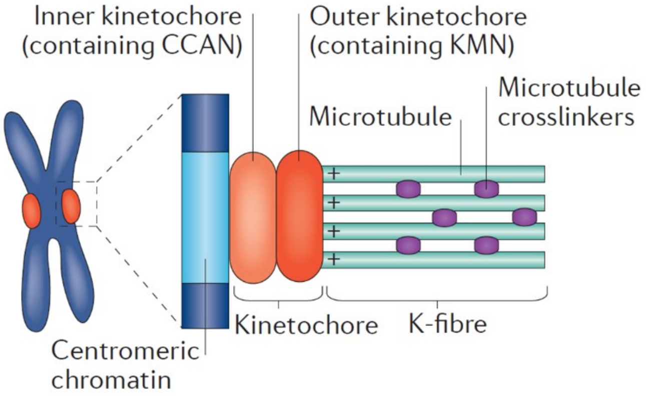

**Figure 9. The site of microtubule-kinetochore attachment.** During mitosis, kinetochore assembles at centromere region of chromosome. Inner kinetochore is connected to chromosome, while the outer serves as a microtubule attachment site. Taken from (Prosser and Pelletier, 2017).

The only situation that ensures correct chromosome segregation is when sister kinetochores are end-on attached to microtubules from the opposite poles (biorientation). This type of kinetochore-microtubule attachment is called the amphitelic attachment (Figure 10). However, during prometaphase erroneous attachments can occur and if they are not corrected during the metaphase, they can lead to errors in chromosome segregation during anaphase. Those situations include one kinetochore of a pair being attached to one pole (monotelic attachment) or both kinetochores being attached to one pole (syntelic attachment) (Figure 10). Additionally, one kinetochore can be attached to both poles at the same time, an attachment called merotely (Figure 10) (Gregan et al., 2011; Prosser and Pelletier, 2017).

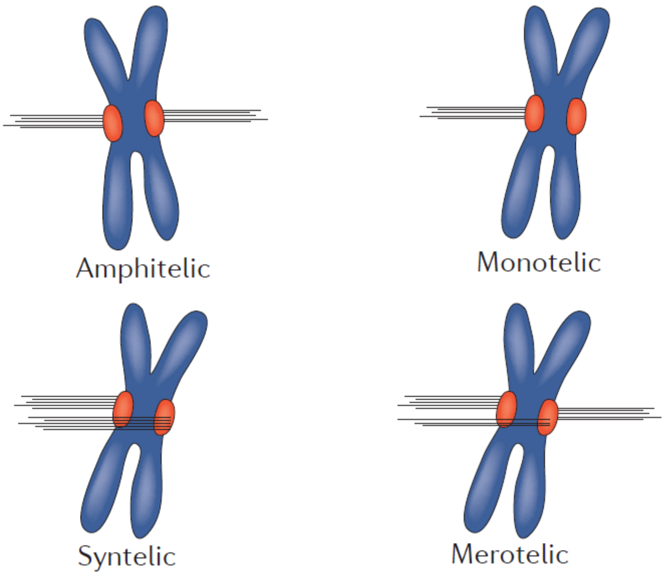

**Figure 10. Types of kinetochore-microtubule attachments.** The only favourable kinetochore-microtubule attachment to properly segregate chromosomes is amphitelic attachment when each sister kinetochore attaches to microtubules from the opposite spindle poles. Erroneous attachments include monotelic (one kinetochore is attached to microtubules from one pole), syntelic (both kinetochores are attached to microtubules from one pole) and merotelic (one kinetochore is attached to microtubules from both poles). Taken from (Prosser and Pelletier, 2017).

SAC ensures that all kinetochores are properly attached to microtubules before anaphase starts. Unattached kinetochores generate diffusible signal that blocks APC/C and Cdc20 complex, required for ubiquitination of securin and cyclin B that promote separation of sister chromatids (Barford, 2020; Watson et al., 2019). Formation of Mitotic Checkpoint Complex (MCC), composed of Mad2, Cdc20, BubR1 and BubR3, on unattached kinetochores inhibits APC/C and Cdc20 complex (Hardwick et al., 2000; Sudakin et al., 2001). SAC is silenced by microtubule attachments to kinetochores. Microtubule attachments cause stripping of Mad proteins from kinetochores regulated by dynein (Howell et al., 2001; Wojcik et al., 2001), and removal of other SAC components, like BuB proteins, from kinetochore (Ji et al., 2015; Vanoosthuyse and Hardwick, 2009).

Additionally, the tension between sister kinetochores has also a significant part in regulating proper kinetochore-microtubule attachments, where Aurora B plays a central role. It regulates phosphorylation of Ndc80 complex and kinesin-13 proteins involved in microtubule depolymerization to correct erroneous attachments. When chromosomes are bioriented and the tension between the sister kinetochores increases, Aurora B detaches from inner kinetochore, blocking further phosphorylation cascade and promoting anaphase onset (Andrews et al., 2004; DeLuca et al., 2006; Lan et al., 2004; Liu et al., 2009; Liu and Lampson, 2009). This mechanism is not silenced if kinetochores have syntelic or monotelic attachments; however, merotelic attachments generate tension that satisfies SAC, leading to lagging chromosomes in anaphase, which is a main cause of aneuploidy (Cimini et al., 2001).

## 2.2. The role of augmin in maintaining spindle architecture and dynamics

### 2.2.1. The structure of augmin complex

The augmin complex was first discovered in *Drosophila melanogaster* when genome-wide RNA interference revealed five genes (dim γ-tubulin (Dgt)2 – Dgt6) that have a role in recruiting γTuRC to spindle microtubules, but not centrosomes (Goshima et al., 2008, 2007). Augmin was later described also in plant (Kimmy Ho et al., 2011) and human cells (Lawo et al., 2009; Uehara et al., 2009). Augmin complex consists of eight homologous to augmin subunits (HAUS) subunits termed HAUS1 – 8. The depletion of augmin subunits resulted in impairment of spindle microtubules and, consequently, mitotic defects (Goshima et al., 2007; Lawo et al., 2009; Uehara et al., 2009). Two functionally distinct hetero-tetrameric subcomplexes of augmin, tetramer II (consisting of HAUS2, 6, 7 and 8) and tetramer III (consisting of HAUS1, 2, 4 and 5), are defined based on their ability to bind pre-existing microtubules or NEDD1, respectively (Song et al., 2018). Recently, the whole molecular structure of augmin complex was determined using single particle cryo-electron microscopy (cryo-EM) (Gabel et al., 2022; Zupa et al., 2022). The cryo-EM revealed that augmin is a flexible structure that contains a V-shaped head with two branches and a filamentous tail (Figure 11). The V-shaped head contains two branches and is a functional tetramer of HAUS2/6/7/8 subunits, while the tail consists of HAUS1/3/4/5 subunits, in agreement with previously described two hetero-tetrameric subcomplexes of augmin.

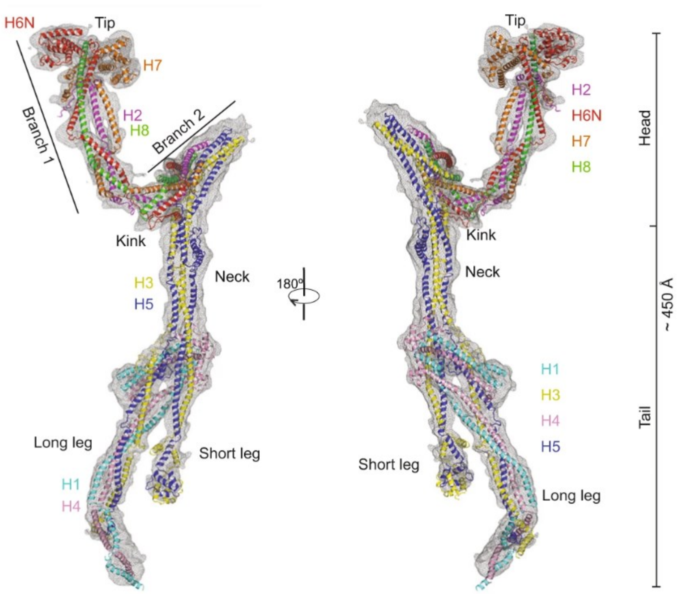

**Figure 11. Cryo-electron microscopy structure of the augmin complex.** Augmin consists of the V-shaped head (with HAUS2/6/7/8 subunits) and the tail (HAUS1/3/4/5 subunits). Taken from (Gabel et al., 2022).

### 2.2.2. Mechanism of augmin-dependent microtubule nucleation

Augmin regulates microtubule nucleation from pre-existing microtubules by targeting NEDD1, which interacts with γTuRC and generates new microtubules at ~30° angle with respect to the mother microtubule (Uehara et al., 2009; Verma and Maresca, 2019; Zhu et al., 2008). Depletion of HAUS6 and HAUS8 resulted in decreased levels of NEDD1 and γTuRC within the spindle and caused impaired chromosome congression, reduced spindle microtubule density, abnormal spindle configuration and mitotic delay (Song et al., 2018; Uehara et al., 2009; Wu et al., 2008; Zhu et al., 2008). It was demonstrated that HAUS6 (also known as FAM29A) recruits the NEDD1-γ-tubulin complex to the spindle to amplify microtubules (Song et al., 2018; Zhu et al., 2008). HAUS8 was found to directly interact with microtubules through its amino terminus that is modulated by Aurora A and Polo-like kinase 1 phosphorylation (Wu et al., 2008). It was recently demonstrated that RanGTP also plays a role in recruiting augmin near the chromosomes. By relieving importin binding from augmin, augmin can bind to microtubules and initiate branching microtubule nucleation near chromosomes (Kraus et al., 2023; Ustinova et al., 2023).

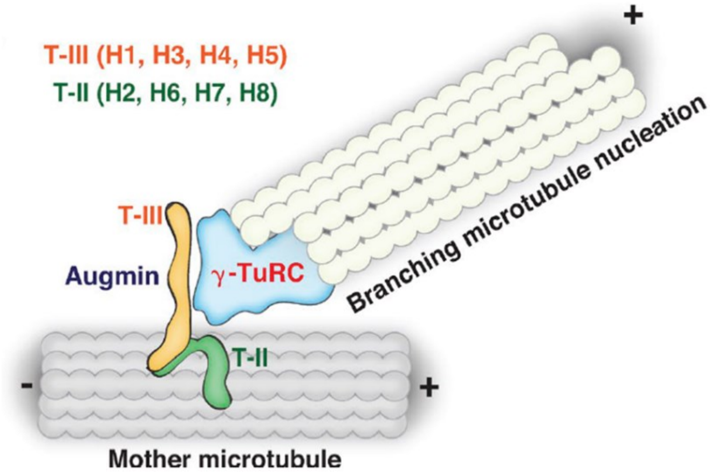

**Figure 12. Augmin interaction with microtubules and γTuRC.** Augmin complex has two distinct functional parts - tetramer-II that binds to mother microtubules and tetramer-III that makes interactions γ-TuRC. Within the tetramers, HAUS6 and HAUS8 bind to γ-TuRC and mother microtubules, respectively. Taken from (Song et al., 2018).

### 2.2.3. Consequences of augmin depletion in cells

Augmin is required for directional growth of noncentrosomal microtubules towards the kinetochores and establishing proper k-fibers (David et al., 2019). While previous studies mainly focused on the effect of augmin on astral and kinetochore microtubules, the effect on midplane-crossing microtubules remains largely unexplored (Almeida et al., 2022; Hayward et al., 2014; Song et al., 2018; Uehara et al., 2009; Uehara et al., 2016; Uehara and Goshima, 2010; Wu et al., 2008; Zhu et al., 2008). Depletion of HAUS8 also had an impact on spindle pole integrity, which was alleviated by NuMa depletion suggesting that those two proteins have opposing activities and in normal conditions regulate pole structure and clustering (Lawo et al., 2009).

Augmin depletion has previously been linked to higher incidence of segregation errors (Wu et al., 2008) and the appearance of lagging chromosomes (Almeida et al., 2022; Viais et al., 2021). Homozygous loss of HAUS6 subunit of the augmin complex was also seen in several cancer types, such as sarcomas, pancreatic adenocarcinomas, gliomas, and glioblastomas (ICGC/TCGA, 2020, retrieved by using cBioPortal (Cerami et al., 2012; Gao et al., 2013)). When HAUS6 was depleted in colorectal cancer cell lines, cell growth was decreased which was dependent on p53/p21 signalling pathway (Shen et al., 2022). Moreover, depletion of

HAUS6 has been linked to brain development in mouse embryos through spindle defects and mitotic delays (Viais et al., 2021). However, the origin of segregation errors in augmin depletion remains largely unexplored due to extensive mitotic delays often experienced by these cells (Wu et al., 2008).

## 2.3. The role of actin in maintaining spindle architecture and dynamics

### 2.3.1. Actin nucleation

Filamentous or F-actin structures consist of actin subunits called globular or G-actin. Actin subunits carry either ATP or ADP molecule depending on whether they are in a form of a monomer or part of a filament, respectively (Figure 13). F-actin is a right-handed helix where asymmetrical actin subunits are assembled head-to-tail and contribute to polar filamentous structure, with a slower-growing minus end (“pointed end”) and a faster-growing plus end (“barbed end”). Filament nucleation happens when actin subunits assemble into the initial aggregate stabilized by subunit–subunit contacts and subsequently elongate by addition of more subunits (Figure 14) (Alberts et al., 2015).

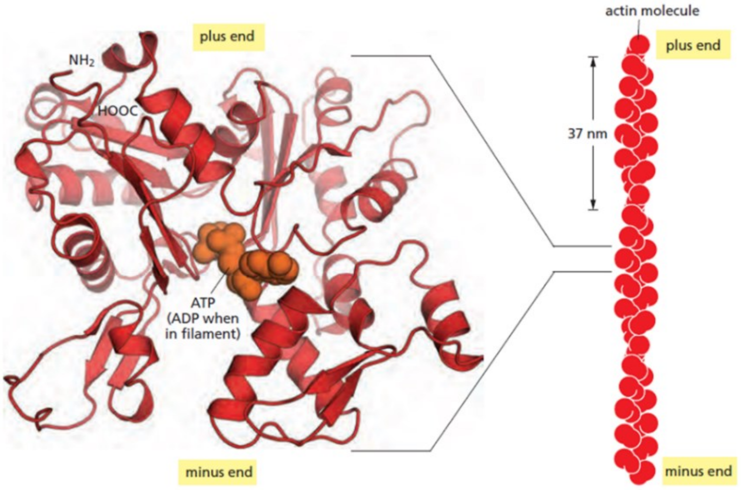

**Figure 13. G-actin and F-actin structures.** The actin subunit, G-actin (left), has either ATP or ADP molecule bound in the center of the molecule. If G-actin is found free in a form of monomer, it carries the ATP molecule and its hydrolysis occurs rarely. When subunits are incorporated into the filament (right), ATP hydrolysis is accelerated, and ADP remains as a part of the filament structure. Actin subunits make two protofilaments that are laterally connected and form a right-handed helix. Each actin filament has a slower-growing minus and a faster-growing plus end. Taken from (Alberts et al., 2015).

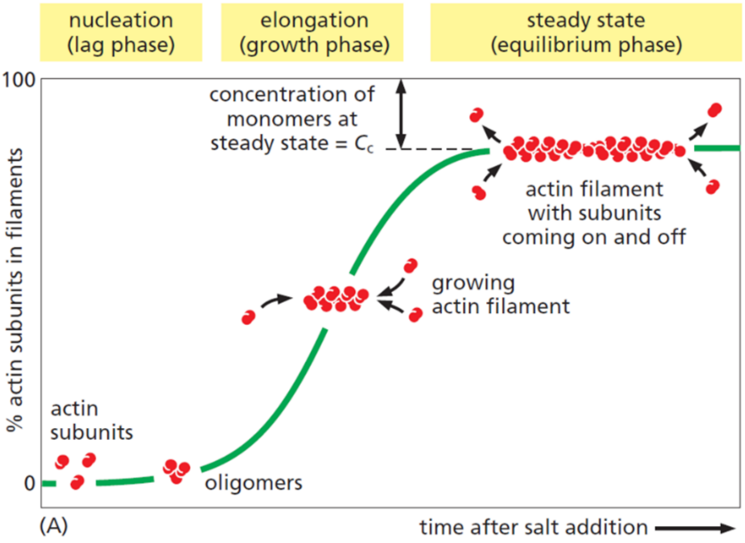

**Figure 14. Actin filament nucleation.** During the lag phase, actin monomers assemble spontaneously into oligomers. The growth phase starts when the initial aggregate (nucleus) forms by assembly of oligomers into a form that resembles actin filament. A that point rapid filament elongation occurs during which new actin subunits are added to the ends of a growing filament. The steady state is achieved when the concentration of actin monomers decreases, and addition and dissociation of actin subunits is balanced. Taken from (Alberts et al., 2015).

Actin filament dynamics is precisely regulated by actin-binding proteins that control monomer concentrations in the cell, filament nucleation, elongation and depolymerization. Proteins thymosin and profilin compete for the same binding site on the actin monomer but regulate opposite activities. When thymosin is bound to actin, it prevents it from binding to actin filament and elongation, while profilin binding promotes binding of actin to plus end of the filament and its elongation (Figure 15) (Goldschmidt-Clermont et al., 1992). The actin-nucleation proteins, Arp2/3 complex and formin, promote filament nucleation by bringing several actin subunits in a form of a seed. Arp2/3 complex attaches to the side of the existing filament and nucleates branched filament from the minus end (Figure 16) (Goley and Welch, 2006). Formin comes in a form of a dimer and binds to the plus end of actin filament allowing the new subunits to incorporate (Figure 17) (Breitsprecher and Goode, 2013). Tropomodulin, tropomyosin and capping protein stabilize actin filaments, while cofilin and gelsolin promote filament disassembly and severing, respectively (Alberts et al., 2015).

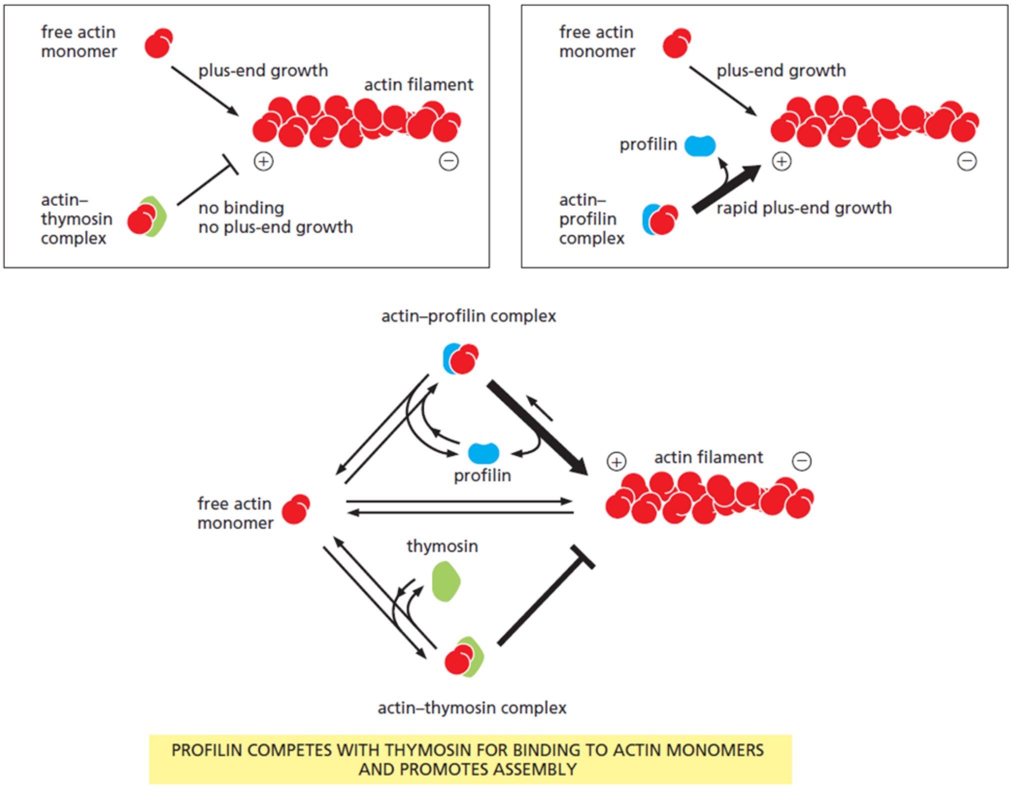

**Figure 15. Actin polymerization with profilin and thymosin.** Thymosin bound to actin monomers prevents them to bind to actin filament, while profilin bound to actin monomers promotes actin polymerization. Either thymosin or profilin can be bound to actin monomers. Taken from (Alberts et al., 2015).

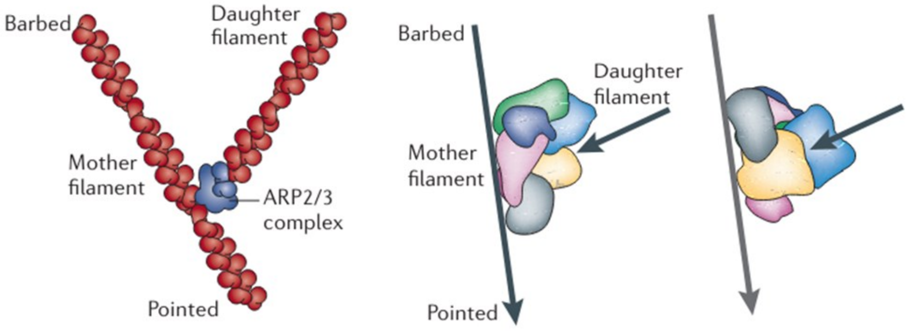

**Figure 16. Actin branching mediated by Arp2/3 complex.** Arp2/3 complex binds to the side of the mother actin filament and promotes nucleation of daughter actin filament at 70° angle with respect to the mother filament (left). On the right are two models of Arp2/3 orientation with respect to the mother filament. ARP2 (blue) and ARP3 (yellow) are connected to the pointed end of the daughter filament. Other subunits make contacts with the mother filament. Taken from (Goley and Welch, 2006).

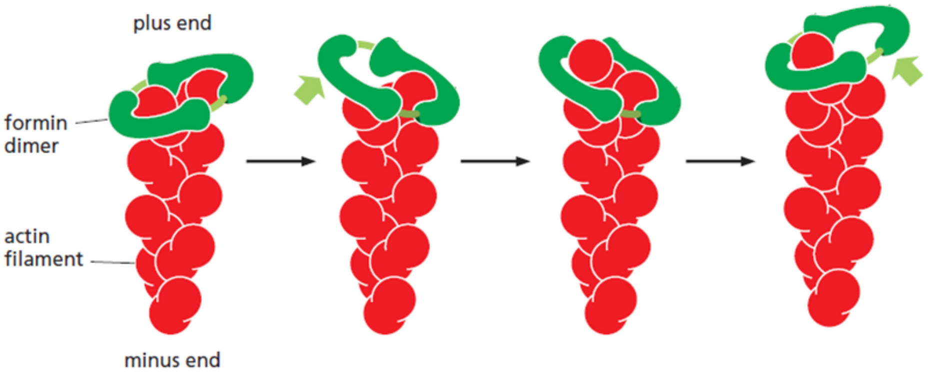

**Figure 17. Mechanism of formin mediated actin polymerization.** Formin (green) is a dimer associated to the plus end of actin filament (red) and promotes binding of new actin subunits to the filament and, consequently, its elongation. Taken from (Alberts et al., 2015).

Actin filaments can also form contractile structures with myosin motors. In these structures, actin filaments are cross-linked and slide apart leading to contraction. Myosin II, a motor required for muscle contraction, is also found as a part of contractile ring required for cytokinesis and as a part of fibers required for cell adhesion and mechanical support (Dogterom and Koenderink, 2019). Myosin II consists of globular head domain that generates force and long coiled-coil tail that can make tail-tail interactions with other myosin molecules. By binding ATP and its hydrolysis, myosin goes through structural changes where it is at one point bound to actin filament and at another not, causing the movement of single actin filament (more detailed on Figure 18) (Alberts et al., 2015).

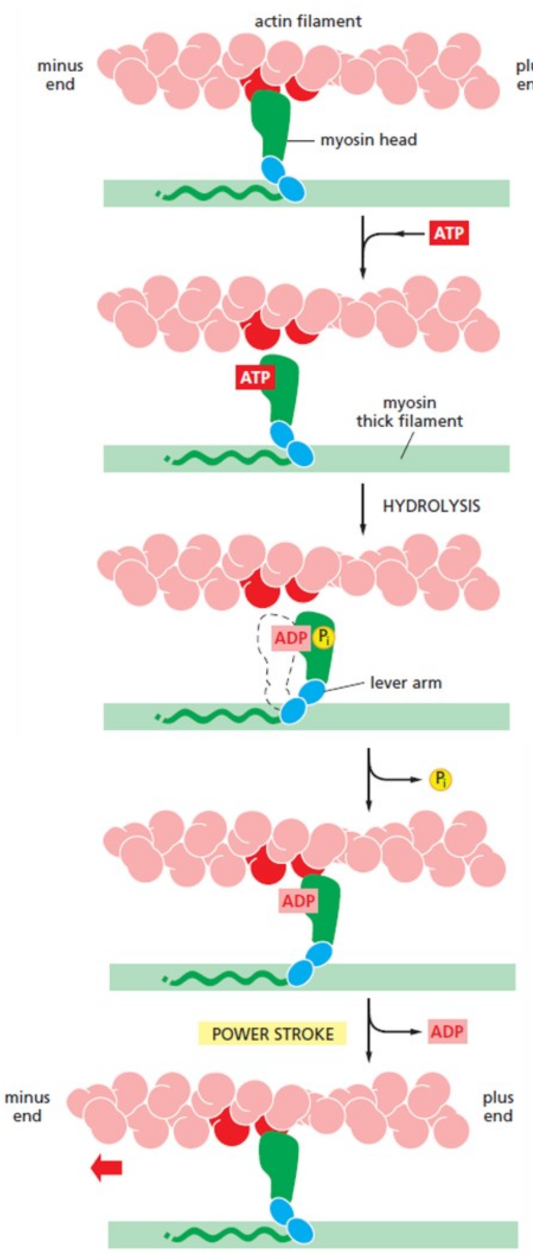

**Figure 18. Mechanism of myosin II walking along the actin filament.** Myosin without any bound nucleotides is tightly attached onto the actin filament. ATP binding to the large cleft on myosin head causes conformational change and a decrease in myosin affinity to bind actin filaments. Upon ATP binding, cleft closes and moves lever arm displacing myosin head along the actin filament. After hydrolysis and release of inorganic phosphate, myosin head is again tightly bound to the actin. This causes power stroke where myosin head loses ADP and is again locked tightly to the actin filament in a new position. This cycle enables movement of actin filaments. Taken from (Alberts et al., 2015).

### 2.3.2. Actin inhibitors

Several chemical compounds can modulate actin filament dynamics and can be used to investigate the role of actin within the cell. Latrunculins (toxins derived from sponges) and cytochalasins (toxins derived from fungi) prevent actin polymerization by binding to actin subunits or plus ends of actin filaments, respectively (Coué et al., 1987; MacLean-Fletcher and Pollard, 1980). Small molecule inhibitor, CK666, is used to inhibit Arp2/3 complex by stabilizing its inactive state. In that way, CK666 is used to impair actin branching in the cell (Hetrick et al., 2013). Phalloidins are bicyclic peptides isolated from *Amanita* mushroom and stabilize actin from depolymerization by tightly binding along the filament (Dancker et al., 1975). Another macrocyclic peptide isolated from marine sponge *Jaspis johnstoni*, jasplakinolide, competes for the same spots on the actin filament and stabilizes them *in vitro* (Bubb et al., 1994). *In vivo*, this stabilization disrupts actin filaments and induces polymerization of actin subunits into aggregates (Bubb et al., 2000). Both drugs, phalloidin and jasplakinolide, are commonly used as a part of probes to visualize F-actin in cells. Phalloidin is usually conjugated to fluorophores but can be only used in fixed samples since it is not cell permeable (Wulf et al., 1979). Recently introduced probes for live-cell imaging are based on silicon-rhodamine (SiR) derivatives and are applicable for superresolution imaging (Lukinavičius et al., 2014). In this thesis, I used SiR-actin, desbromo-desmethyl-jasplakinolide conjugated to SiR, for labelling F-actin structures that I imaged on STED microscope.

### 2.3.3. Actin and microtubule crosstalk during mitosis

During mitosis, the cell needs to reorganize not only the interphase microtubules into the mitotic spindle, but it also needs to reconstruct the interphase actin cytoskeleton. Actin plays a crucial role during mitosis, firstly taking part in mitotic cell rounding where actomyosin cortex ensures proper tension throughout the cell, and then in forming actomyosin contractile ring required for cytokinesis (Dogterom and Koenderink, 2019).

The mitotic rounding is driven by myosin-II contraction on the actin cortex. For proper cell rounding during mitosis, actomyosin cortex needs to be anchored to the cell membrane by ezrin–radixin–moesin (ERM) proteins (Figure 19). The cell rounding is crucial for providing a space for microtubules to search and capture the chromosomes (Lancaster et al., 2013). The actin cortex also provides cortical anchors for astral microtubules required for spindle orientation. These “subcortical actin clouds” are connected to retraction fibers and serve as a direct interaction site with astral microtubules (Kunda and Baum, 2009). The connection of astral microtubules and cortex is also achieved through G protein $\alpha_i$ subunit ($G\alpha_i$) - Leu–Gly–Asn repeat-enriched protein (LGN) and NuMA (Figure 19). NuMA is released into the cytoplasm during NEBD and binds on one side $G\alpha_i$ and LGN and on another dynein that captures astral microtubules (Gloerich et al., 2017). Dynein exerts pulling forces on astral microtubules and contributes to spindle positioning within the cell (Redemann et al., 2010).

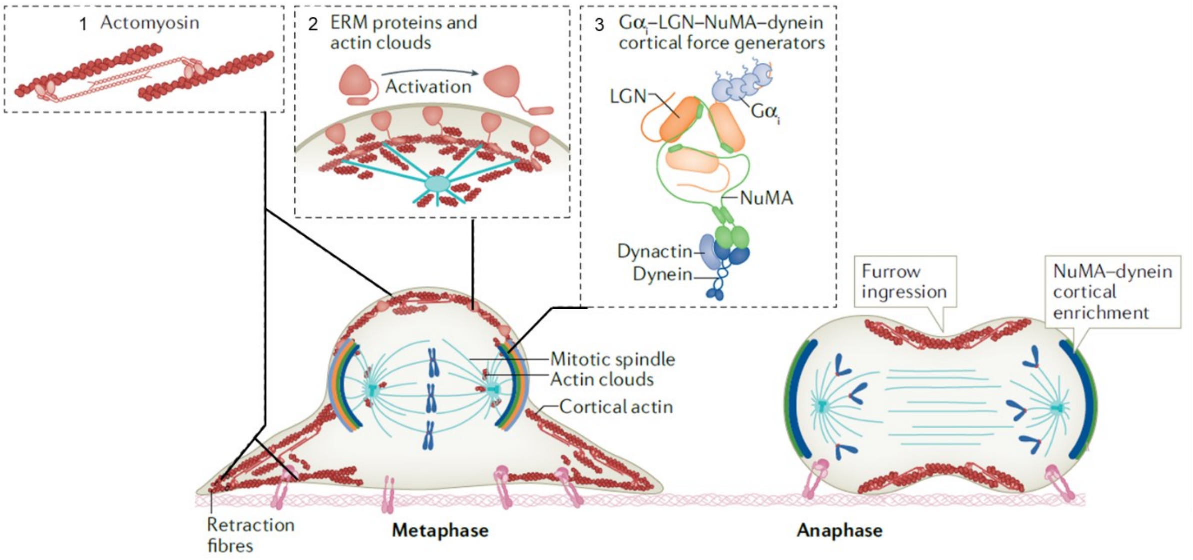

**Figure 19. Actin-microtubule interplay during mitosis.** The rounding of mitotic cells is driven by actomyosin cortex (1) that is anchored to the cell membrane by ERM proteins (2). The connection between astral microtubules is achieved through subcortical actin clouds (2) and $G\alpha_i$–LGN–NuMA complex which binds dynein (3). During anaphase, contractile actomyosin ring is formed and cytokinesis is initiated by formation of furrow ingression. Taken and modified from (Lechler and Mapelli, 2021).

During cytokinesis, contractile actomyosin ring is always formed to ensure symmetrical cell division. The assembly of contractile ring is regulated by RHOA activator, which is delivered by kinesin VI motors (Foe and von Dassow, 2008; Yüce et al., 2005). RHOA activator promotes polymerization of unbranched actin via mammalian Diaphanous-related (mDia) formins. Furthermore, RHOA activates anilin required for scaffolding contractile ring (by interacting with F-actin, myosin II and plasma membrane) and recruits more RHOA in the spindle midzone contributing to the positive feedback loop between the RHOA and anilin (Gregory et al., 2008). Finally, anilin is found to crosslink microtubules in the spindle with the contractile ring therefore making a connection between those two structures (van Oostende Triplet et al., 2014).

### 2.3.4. The roles of spindle actin

Cytoplasmic or spindle actin has lately emerged as a distinct type of actin in mitotic spindles (Lu et al., 2014). After many years of defining centrosomes as microtubule organizing centers, it has recently been proven that they also serve as actin organizing centers. In this case, the assembly of actin filaments is induced in response to WASH and Arp2/3 recruitment to the centrosome, with actin filaments predominantly observed in less adherent cells. Therefore, centrosome-mediated actin nucleation might indicate an additional level of actin assembly regulation at the centrosome by sensing the changes in cell adhesion (Farina et al., 2016). This is further supported by a direct negative correlation observed between microtubule density and centrosomal actin density in resting lymphocytes. In this case, higher level of cell adhesion causes a decreased availability of actin monomers at the centrosome, resulting in lower density of centrosomal actin and higher density of microtubules (Inoue et al., 2019). During in vitro experiments with purified proteins, actin filaments have also been found to impact the growth rates and lengths of microtubules they align with. In these experiments, branching of actin filaments prevents rescue and causes catastrophe, whereas unbranched actin filaments have an opposite effect and stabilize microtubule growth. The observed effect is independent of the activity of Arp2/3 or actin monomers and can be solely attributed to the role of actin as a physical barrier (Colin et al., 2018). This effect of actin filaments aligns with a recent observation that spindle actin precedes k-fibers during their growth, potentially affecting chromosome congression (Plessner et al., 2019). At the time of its formation throughout prometaphase, spindle actin has been found to concentrate around the poles, with some interpolar actin bundles extending from pole to pole (Kita et al., 2019). Actin is known to attach to the centrosome through a phosphorylated form of an actin-associated protein cortactin, with their association levels rising from G2-M transition preceding NEBD up until the end of metaphase (Wang et al., 2008). However, the exact mechanism by which the spindle actin forms remains largely unexplored, and both formins (Kita et al., 2019) and Arp2/3 complex (Plessner et al., 2019) have been implicated in the process. While myosin activity in these processes remains largely unexplored, the ability of myosin X to bind to actin (Homma et al., 2001), microtubules (Weber et al., 2004) and spindle assembly factors, such as TPX2 (Woolner et al., 2008), make it a potential candidate for modulation of actin-microtubule interactions during spindle assembly (Woolner et al., 2008).

Lastly, perinuclear actin was observed in most recent studies as another type of actin structure in prometaphase (Booth et al., 2019; Plessner et al., 2019). It has been discovered that perinuclear actin plays an important role soon after NEBD, when it contributes to chromosome congression through a mechanism independent of microtubules (Booth et al., 2019). The congression happens in response to myosin II activity, which causes a contraction of the actomyosin network that remains on the top of nuclear envelope remnants. Although this contraction primarily ensures that all chromosomes gather within pole-to-pole region once initial chromosome-microtubule connections form, it likely also facilitates initial chromosome-microtubule interactions. Interestingly, the presence of perinuclear actin varies between different cell lines, and cells without perinuclear actin exhibit higher levels of aneuploidy compared to cells with perinuclear actin around the nuclear envelope (Booth et al., 2019).

### 2.3.5. The roles of actin during meiosis

The substantial role of actin was demonstrated during oocyte (female gametes) meiosis, and in this part, I will describe its role in mouse oocytes. Oocytes undergo two cycles of asymmetric meiotic divisions. The first division produces the fertilizable egg and a polar body, while the second division happens during fertilization and also results in the large egg and the polar body. Oocytes are stored in ovaries from birth onwards and are arrested in prophase of meiosis I (Figure 20). Every menstrual cycle, an oocyte continues meiosis by first assembling meiotic spindle, which then migrates towards the cell cortex to segregate homologues chromosomes and extrude the first polar body. After assembling spindle, oocyte is arrested in metaphase of meiosis II until fertilization when second meiosis starts and the second polar body is extruded. After that, the two haploid female and male pronuclei migrate towards the zygote center and the first mitotic division of the embryo starts (Uraji et al., 2018).

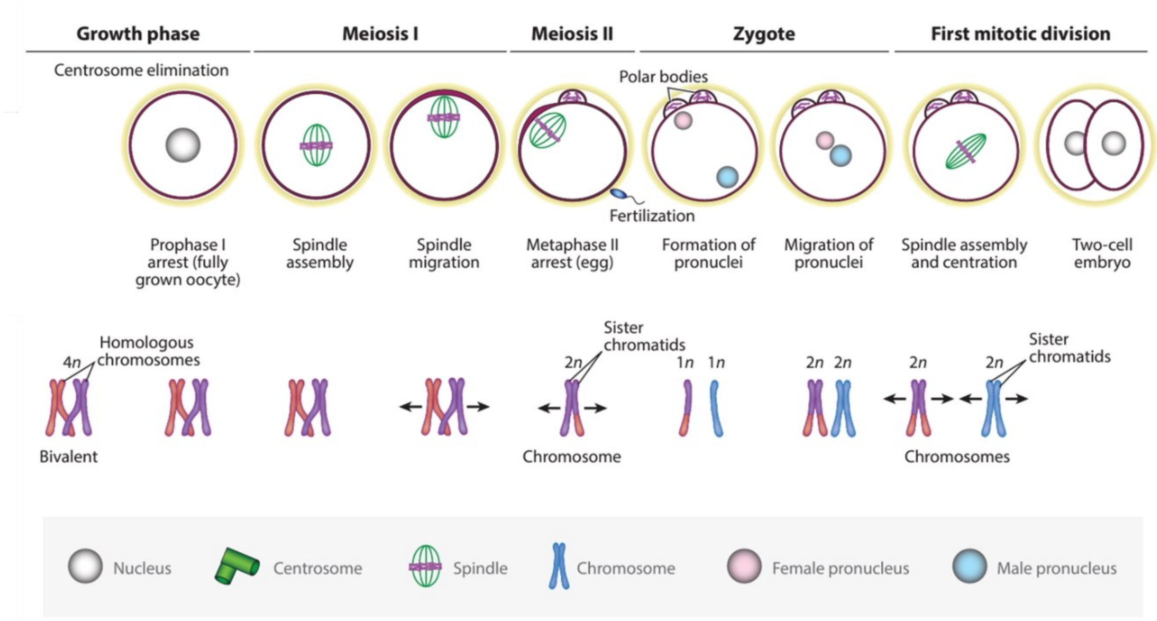

**Figure 20. Meiotic phases in mouse oocytes.** Every menstrual cycle, oocytes arrested at prophase I are released and undergo two asymmetric meiotic divisions. In the first division, spindle assembles and migrates towards the oocyte surface where segregation of haploid chromosomes and the extrusion of the first polar body happens. In the second division, oocytes are arrested in metaphase until the fertilization that triggers segregation of chromosomes and extrusion of the second polar body. The two haploid pronuclei migrate and unite at the center of zygote. From that point onwards, embryonic mitotic divisions start. Taken and adapted from (Mogessie et al., 2018).

The main difference between the meiotic and mitotic spindle is the lack of centrosomes and associated astral microtubules required for normal mitotic cell division. Because of that, actin cytoskeleton is involved in several functions to ensure proper mammalian meiosis. Firstly, F-actin is involved in the spindle migration from the mouse oocyte center towards the cell cortex after spindle assembly during meiosis I. Different approaches to perturb actin cytoskeleton demonstrated that spindle migration was perturbed during this phase (Azoury et al., 2008; Dumont et al., 2007; Schuh and Ellenberg, 2008). This process is regulated by different actin – dependent pathways, where myosin-2 and formin-2 play a significant role (Azoury et al., 2008; Schuh and Ellenberg, 2008). In mitotic divisions, astral microtubules are involved in spindle positioning, however microtubule depolymerization did not have any impact on spindle positioning in oocytes (Azoury et al., 2008). Second, actin is involved in the spindle anchorage during arrest in metaphase II by forming the actin cap (Liu et al., 2000; Maro et al., 1984).

Furthermore, Arp2/3 complex is required for generating actin flow that pushes the spindle towards the cell cortex and counteracting the myosin-2 activity from pushing it towards the oocyte center (Yi et al., 2011). Third, the actin cytoskeleton is involved in polar body extrusion during mouse meiosis I and II. Enrichment of actin and myosin-2 in the actin cap and contraction ring formation around the cap by myosin-2 are required for polar body extrusion (Simerly et al., 1998; Wang et al., 2011). The actomyosin ring is also required for membrane protrusion and ingression during cytokinesis, the similar role seen in mitotic spindles (Deng and Li, 2009; Dumont et al., 2007; Elbaz et al., 2010; Pfender et al., 2011). And finally, actin was found to be important for preventing chromosome segregation errors during mouse meiosis (Mogessie and Schuh, 2017). This study demonstrated that inhibition of actin cytoskeleton causes increase in misaligned and lagging chromosomes during meiosis II metaphase and meiosis I and II anaphase, respectively. Interestingly, this process happened through the formation of k-fibers, where actin was demonstrated to be important for k-fiber bundling. Here, I focused only on the actin functions during mammalian meiosis I and II, but it is also involved in the vesicle transport towards the plasma membrane and in the nucleus positioning to the oocyte center prior to NEBD (Uraji et al., 2018).

The actin cytoskeleton has a variety of roles during mammalian meiotic divisions. The role of actin in spindle positioning is well known also during mitosis (Lancaster et al., 2013), however the functions of actin within the spindle are still unclear. In mouse meiosis actin showed a substantial role in k-fiber formation required for normal chromosome congression (Mogessie and Schuh, 2017), but this role during mitosis is still unexplored. Only recently the importance of spindle actin was demonstrated in normal chromosome congression and segregation (Plessner et al., 2019), but the clear mechanism still remains unknown. The work in this thesis will try to understand these mechanisms.

# 3. MATERIALS AND METHODS

## 3.1. Cell culture

The following cell lines were used: unlabelled human hTERT-RPE1 (hTERT-immortalized retinal pigment epithelium) cell line (ATCC); human hTERT-RPE1 cell line stably expressing CENP-A-GFP and hTERT-RPE1 cell line stably expressing CENP-A-GFP and Centrin1-GFP (Magidson et al., 2011), a gift from Alexey Khodjakov, Wadsworth Center, New York State Department of Health, NY, USA; human RPE1 CRISPR-Cas9 cells stably expressing PRC1-GFP (Asthana et al., 2021), a gift from Thomas Surrey, Centre for Genomic Regulation, Barcelona, Spain; human hTERT-RPE1 cells stably expressing Centrin-GFP H2B-eGFP mCherry-tubulin and carrying tetracycline-inducible system for Plk4 (Vitre et al., 2020), a gift from Benjamin Vitré, Centre national de la recherche scientifique, Montpellier, France; human U2OS cells stably expressing CENP-A-GFP, mCherry-α-tubulin and PA-GFP-α-tubulin (Barisic et al., 2014), a gift from Marin Barišić, Danish Cancer Society Research Center, Copenhagen, Denmark; human HeLa-TDS cells stably expressing GFP-α-tubulin (Kajtez et al., 2016) and human HeLa-Kyoto BAC cells stably expressing PRC1-GFP (Poser et al., 2008), a gift from Ina Poser and Tony Hyman, MPI-CBG, Dresden, Germany. All cell lines were cultured in Dulbecco's Modified Eagle's Medium (DMEM) containing 1 g/L D-glucose, pyruvate and L-glutamine (Gibco), and supplemented with 10% (vol/vol) heat-inactivated Fetal Bovine Serum (FBS, Sigma Aldrich, MO, USA) and penicillin (100 IU/mL)/streptomycin (100 mg/mL) solution (Lonza, Basel, Switzerland). All cell lines were kept at 37°C and 5% $CO_2$ in a Galaxy 170 R humidified incubator (Eppendorf, Hamburg, Germany) and regularly tested for mycoplasma contamination. All cell lines used for experiments have been confirmed to be mycoplasma free if no extracellular DNA was present after DAPI staining (1 µg/mL, D9542, Sigma-Aldrich, MO, USA).

## 3.2. siRNA transfection

One day before siRNA transfection, 80 000 - 150 000 cells were seeded on 35 mm uncoated dishes with 160-190 µm (1.5 coverglass) glass thickness (MatTek Corporation, Ashland, MA, USA or Ibidi GmbH, Gräfeling, Germany) in 2 ml of DMEM medium. Cells were transfected with either targeting or non-targeting siRNA constructs which were diluted in OPTI-MEM medium (Life Technologies, Waltham, MA, US). Transfection was performed using

Lipofectamine RNAiMAX Reagent (Life Technologies, Waltham, MA, US) according to the manufacturer's instructions. After four hours of treatment, the transfection mixture was replaced with the DMEM medium. The following constructs and their final concentrations were: control siRNA (20 nM, D-001810-10-05, Dharmacon, Lafayette, CO, USA), human HAUS6 siRNA (20 nM, L-018372-01-0005, Dharmacon, Lafayette, CO, USA), human HAUS8 siRNA (20 nM, L-031247-01-0005, Dharmacon, Lafayette, CO, USA), human Mad2 siRNA (100 nM, L-003271-00-0010, Dharmacon, Lafayette, CO, USA) and human Myosin-X siRNA (100 nM, L-023017-00-0005, Dharmacon, Lafayette, CO, USA). Experiments were performed 24 hours after Mad2 and Myosin-X siRNA treatment and 48 hours after HAUS6 and HAUS8 siRNA treatment.

### 3.3. Live-cell dyes

To visualize microtubules or DNA during live cell-imaging in experiments where HAUS6 or HAUS8 were depleted, far-red silicon rhodamine (SiR)-tubulin-670 dye (final concentration of 100 nM, Spirochrome, Stein am Rhein, Switzerland) or either SiR-DNA or SPY-555-DNA (final concentration of 100 nM, Spirochrome, Stein am Rhein, Switzerland) were used 45 min to 2 hr prior to imaging, respectively. In order to avoid dye efflux, a broad-spectrum efflux pump inhibitor verapamil (final concentration of 0.5 μM, Spirochrome, Stein am Rhein, Switzerland) was added to RPE1 cells along with tubulin and/or DNA dyes.

### 3.4. Treatments with inhibitors

To arrest the cells in metaphase after HAUS6 depletion, MG-132 (final concentration of 20 μM, M7449-1ML, Sigma Aldrich, MO, USA) was added to the cell media for 30 min prior to imaging. To inhibit actin polymerization and branching (Arp2/3 complex), latrunculin A (final concentration of 0.5 μM, 428021, Sigma-Aldrich, MO, USA) and CK-666 (final concentration of 200 μM, SML006, Sigma-Aldrich, MO, USA) inhibitors were used, respectively. Jasplakinolide (final concentration of 2 μM, J4580, Sigma-Aldrich, MO, USA) was used to stabilize actin filaments. All actin inhibitors were added one to six hours prior to live-cell imaging or fixation. Plk4 inhibitor centrinone (Wong et al., 2015) (final concentration of 300 nM, HY-18682, MedChemExpress, NJ, USA) was added 52 hours before the live-cell imaging. Cell media containing fresh centrinone was changed twice a day to prevent Plk4 reactivation.

All inhibitors were prepared in DMSO. To test if DMSO has any toxic effects on cells, the highest concentration used in experiments (0.2% v/v) was added to the cells. Since no significant differences in mitotic timing and segregation errors were observed compared to untreated cells, I used untreated cells as a control in all experiments.

### 3.5. Immunofluorescence

For STED imaging, RPE1 cells stably expressing CENP-A-GFP were grown on 35 mm uncoated dishes with 160-190 µm (1.5 coverglass) glass thickness (Ibidi GmbH, Gräfeling, Germany). To remove the components of the cytoplasm, cell medium was removed and 0.5% Triton in PEM buffer (0.1M PIPES, 1mM EGTA, 1mM MgCl2) was added for 15 s. Following extraction, cells were fixed in 3% paraformaldehyde and 0.1% glutaraldehyde solution for 10 min. To reduce the background fluorescence, quenching (100 mM glycine in PBS) and reduction (0.1% sodium borohydride in PBS) solution were added for 7 and 10 min, respectively. To prevent non-specific binding, cells were incubated in blocking/permeabilization buffer (2% NGS and 0.5% Triton-X-100 in PBS) for 2 hr at 4 °C. Microtubules were then stained using a rat anti-tubulin primary antibody (1:500 in blocking/permeabilization buffer, MA1-80017, Invitrogen) with a 4 °C overnight incubation. The next day, cells were washed with PBS three times for 5 min. After washing, a secondary antibody donkey anti-rat Alexa Fluor 594 or Alexa Fluor 568 (1:1000 in blocking/permeabilization buffer, Abcam, ab150156, ab175475) was added and incubated for 1 hr at room temperature. SiR-actin (200 nM in PBS, Spirochrome, Stein am Rhein, Switzerland) was incubated for 20 min at room temperature to visualize actin structures in the cell.

When any type of actin inhibition or Myosin 10 depletion were performed, pre-extraction step could not be used since it caused shrinkage of the cells due to already impaired cell membrane. For STED imaging of those cells, RPE1 cells stably expressing CENP-A-GFP and Centrin1-GFP were grown on 35 mm uncoated dishes with 160-190 µm (1.5 coverglass) glass thickness (Ibidi GmbH, Gräfeling, Germany). Cells were fixed by 1 ml of 3.2% paraformaldehyde and 0.25% glutaraldehyde in PBS for 10 min on room temperature. Following fixation, cells were washed three times for 5 min with 1 ml of PBS and permeabilized with 0.5% Triton-X-100 in PBS for 25 min at a room temperature. To block unspecific binding, cells were incubated in 1 ml of blocking/permeabilization buffer (1% normal goat serum (NGS) and 0.1% Triton-X-100 in PBS) for 1 hr at 4 °C. Cells were then incubated with 250 µl of primary antibody solution overnight at 4 °C. The primary antibodies used were as follows: rat anti-tubulin primary antibody (1:300 in blocking/permeabilization buffer, MA1-80017, Invitrogen), rabbit anti-MYO10 primary antibody (1:100 in blocking/permeabilization buffer, HPA024223, Sigma Aldrich, immunostaining under this condition resulted in unspecific binding, other antibodies were either not available to purchase or were made for different species). The next day, cells were washed with PBS three times for 5 min. After washing, a secondary antibody donkey anti-rat Alexa Fluor 568 (1:500 in blocking/permeabilization buffer, Abcam, ab175475) was added and incubated for 1 hr at room temperature. SiR-actin (200 nM in PBS, Spirochrome, Stein am Rhein, Switzerland) was incubated for 25 min at room temperature.

For confocal imaging of control and augmin-depleted HeLa cells stably expressing PRC1-GFP, cells were grown on 35 mm uncoated dishes with 160-190 µm (1.5 coverglass) glass thickness and fixed by 2 ml of ice-cold methanol for 1 min at –20 °C. Following fixation, cells were washed three times for 5 min with 1 ml of PBS and permeabilized with 0.5% Triton-X-100 in water for 15 min at a room temperature. This step was repeated twice when tubulin staining was performed. To block unspecific binding, cells were incubated in 1 ml of blocking buffer (1% normal goat serum (NGS)) for 1 hr at 4 °C. Cells were then washed three times for 5 min with 1 ml of PBS and incubated with 250 µl of primary antibody solution overnight at 4 °C. The primary antibodies used were as follows: rabbit polyclonal PRC1 (diluted 1:100, sc-8356, Santa Cruz Biotechnology), rabbit polyclonal HAUS6 (diluted 1:250, ab-150806, Abcam), rabbit polyclonal HAUS8 (diluted 1:100, PA5-21331, Invitrogen) and rat monoclonal tubulin (diluted 1:100, MA1-80017, Invitrogen). After the incubation with a primary antibody, cells were washed 3 times for 5 min with 1 ml of PBS and then incubated with 250 µl of secondary antibody for 45 min at a room temperature. Alexa Fluor 488 and 594 (Abcam, ab150073, ab150076, ab150156) were used as secondary antibodies at a 1:1000 dilution for PRC1 staining, 1:500 dilution for HAUS6 and 1:250 for HAUS8 and tubulin staining. DAPI (1 µg/mL) was used for chromosome visualization.

### 3.6. SDS-PAGE and Western blot

RPE1 cells stably expressing CENP-A-GFP and Centrin1-GFP were seeded on six-well plates (Thermo Fisher Scientific, Waltham, MA, USA) and transfected with HAUS6 or HAUS8 siRNA following previously described protocol. Following transfection, cells were lysed in RIPA buffer (R0287, Sigma Aldrich, M7449-1ML, MO, USA) containing 1 x protease inhibitor (5892970001, Roche, Basel, Switzerland), 1 x phosphatase inhibitor (4906837001, Roche, Basel, Switzerland) and 1 mM PMSF by two cycles of freezing and thawing in liquid nitrogen. Protein extracts were mixed with 2 x Laemlli sample buffer (S3401, Sigma Aldrich, M7449-1ML, MO, USA) and heated at 95 °C for 10 min prior to SDS-PAGE. After protein transfer onto the nitrocellulose membrane (IB23002, Invitrogen, Waltham, MA, USA) and blocking with blocking solution (5% bovine serum albumin and 0,1% Tween 20 in PBS) for 1 hr, membranes were incubated overnight at 4 °C with primary antibodies diluted in blocking solution. The primary antibodies used were as follows: rabbit polyclonal HAUS6 (diluted 1:1000, ab-150806, Abcam), rabbit polyclonal GAPDH (diluted 1:1000, ab9485, Abcam). Rabbit polyclonal HAUS8 antibody (diluted 1:1000, PA5-21331, Invitrogen and NBP2-42849, Novus Biologicals) resulted in no detectable bands under these conditions. Membranes were washed with 0.1% Tween 20 in PBS, incubated for 1 hr with anti-rabbit HRP-conjugated secondary antibodies (dilution 1:10,000, ab6721, Abcam) and visualized on the C-DiGit blot scanner (LI-COR, Bad Homburg, Germany) with WesternSure PREMIUM Chemiluminescent Substrate (926–95000, LI-COR, Bad Homburg, Germany).

### 3.7. Microscopy

STED microscopy of fixed RPE1 cells stained for microtubules or both microtubules and actin was performed using an Expert Line easy3D STED microscope system (Abberior Instruments, Göttingen, Germany) with the 100 x/1.4NA UPLSAPO oil objective (Olympus, Tokio, Japan) and an avalanche photodiode (APD) detector. The 488 nm, 561 nm and 647 nm laser lines were used for excitation of GFP, Alexa Fluor 568/594 and SiR-actin, respectively. The 775 nm laser line was used for depletion of red and far red lines during STED superresolution imaging. Images were acquired using the Imspector software. The xy pixel size for fixed cells was set to 20 nm and 6 focal planes were acquired with 300 nm distance between planes when only microtubules were imaged in STED. For two-color STED of microtubules and actin, pixel size was set to 20 nm and 1 focal plane was acquired. In both cases, line accumulation was set to 1, dwell time to 10 μs and pinhole size to 1.0 AU (Airy units). Live-cell imaging of Mad2-depleted and Mad2/HAUS6-codepleted RPE1 cells was performed using confocal mode on Expert Line easy3D STED microscope system. The xy pixel size was 80 nm and 16 focal planes were acquired, with 1 μm distance between the planes and 30 s time intervals between different frames. The line accumulation was set to 2, dwell time to 2.2 μs and pinhole size to 1.0 AU. During live-cell imaging, cells were kept at 37 °C and 5% CO2 in Okolab Cage Incubator (Okolab, Pozzuoli, NA, Italy).

Other confocal images of HAUS6-depleted RPE1 or HeLa cells were acquired using a previously described microscope setup (Buđa et al., 2017), consisting of a Bruker Opterra Multipoint Scanning Confocal Microscope (Bruker Nano Surfaces, Middleton, WI, USA), mounted on a Nikon Ti-E inverted microscope with a Nikon CFI Plan Apo VC 100 x/1.4 numerical aperture oil objective (Nikon, Amstelveen, The Netherlands). During live-cell imaging, cells were kept at 37 °C and 5% CO2 in Okolab Cage Incubator (Okolab, Pozzuoli, NA, Italy). To excite Hoechst, GFP, mCherry or SiR fluorescence, a 405 nm, 488 nm, 561 nm or 647 nm laser lines were used, respectively. Opterra Dichroic and Barrier Filter Set 405/488/561/640 enabled the separation of excitation light from the emitted fluorescence. Images were acquired using Evolve 512 Delta Electron Multiplying Charge Coupled Device (EMCCD) Camera (Photometrics, Tuscon, AZ, USA), with camera readout mode of 20 MHz. The xy pixel size was 83 nm. In all experiments where the whole spindle stack was imaged, z-stacks were acquired with unidirectional xyz scan mode at 37 focal planes and 0.5 μm distance between the planes. Photoactivation of U2OS cells was performed perpendicular to pole-to-pole axis of metaphase spindles using a 405 nm laser diode (Coherent, Santa Clara, CA, USA) and a line pattern of 12 equally distributed points, with each point representing one laser hit. The interval between the points was 0.05 ms and photoactivation area was set to 0.5 μm for each point. The interval between successive frames was set to 10 s and one central z-plane was imaged.

Airyscan imaging of RPE1 cells stained for microtubules and actin was performed on the Airyscan Zeiss LSM800 confocal laser scanning microscope with the 63x/1.4NA Oil DIC M27 Plan-Apochromat objective (Carl Zeiss, Germany) and LSM 800 camera. To excite DAPI, GFP, Alexa Fluor 594 and 647, the 405 nm, 488 nm, 561 nm and 647 nm laser lines were used, respectively with 405/488/561/640 filters. LSM scan speed was set to 5, line step and averaging was set to 1, unidirectional scan direction and airyscan detector was used on all images. Images were acquired in ZEN blue 3.5 software and a single z-plane was acquired.

The Lattice Lightsheet 7 system (Carl Zeiss, Germany) was used for live cell imaging of RPE1 control cells and cells treated with different actin inhibitors. The system was equipped with an illumination objective lens 13.3×/0.4 (at a 30° angle to cover the glass) with a static phase element and a detection objective lens 44.83×/1.0 (at a 60° angle to cover the glass) with an Alvarez manipulator. The 488 nm diode laser was used to excite CENP-A-GFP and Centrin1-GFP or Centrin-GFP and H2b-eGFP with laser power set to 1.5% and exposure time to 12 ms and 15 ms, respectively. The 561 nm diode laser was used to excite tubulin-mCherry with laser power and exposure time set to 2.2% and 15 ms, respectively. LBF 405/488/561/642 emission filter was used. The detection module consisted of a Hamamatsu ORCA-Fusion sCMOS camera. During imaging, cells were kept at 37 °C and at 5% CO2 in a Zeiss stage incubation chamber system (Carl Zeiss, Germany). The automatic immersion of water was applied from the motorized dispenser at an interval of 25 minutes. The width of the imaging area in the x dimension was set to 1300 μm with the x interval of 0.5 μm. Images were acquired every 1 to 2 minutes during maximum 20 hours in ZEN 3.9 software.

### 3.8. Image processing and data analysis

All images were analysed in Fiji/ImageJ (National Institutes of Health, Bethesda, MD, USA). Rstudio (R Foundation for Statistical Computing, Vienna, Austria) was used to transform the spindles into an end-on view. Quantification, plotting and statistical analysis was performed in MATLAB (MathWorks, Natick, MA, USA). First, the data were tested for normal distribution using the Shapiro-Wilk test of normality. Two normally distributed groups of data were tested with two-tailed t-test, while more than two groups were tested with one-way ANOVA followed by the post-hoc Tukey test. Two non-normally distributed groups of data were tested with Mann-Whitney test, while more than two groups were tested with Kruskal-Wallis rank sum test followed by post-hoc Dunn's test. Proportions were statistically compared with two-proportions z-test with Yate’s correction used for data with count smaller than 5. Used statistical tests for each analysis is written in the figure captions. Figures were assembled in Adobe Illustrator CS5 (Adobe Systems, Mountain View, CA, USA).

### 3.8.1. Imaging criteria and signal adjustment for augmin related experiments

Only bipolar spindles in cells where HAUS6 or HAUS8 were depleted were imaged and analysed, although multipolar spindles were also observed, as reported previously (Lawo et al., 2009). Raw images were used for quantification. In representative immunofluorescence images of augmin depletion, all signals were adjusted equally in control and treated cells. However, due to severe reduction of bridging fibers in augmin-depleted spindles, the contrast in images for representation on figures was not always equally adjusted, as this led to important spindle structures being either highly oversaturated or barely visible. It was instead adjusted so that astral microtubules are similarly visible in control and augmin-depleted spindles in STED microscopy, or that all present bridging fibers are visible in confocal microscopy. These adjustments did not result in any structures being omitted or otherwise modified in a way that could lead to misrepresentation.

### 3.8.2. Measuring tubulin intensity in k-fibers, bridging fibers and astral microtubules in control and augmin-depleted cells

The tubulin intensity of bridging and k-fibers was measured by using 25x25 or 5x5 pixel Square tool (ImageJ) on STED and confocal images, respectively. Bridging fibers were measured on microtubule signal extending between two kinetochores, while k-fibers were measured next to the kinetochores (average of two k-fibers was used for further analysis). The background was measured using the same tool at several empty areas within the spindle (10 randomly positioned squares for STED and 2 squares just above and below bridging fiber for confocal images). The average background intensity was subtracted from bridging ($I_\mathrm{b} = I_\mathrm{b+bcg} - I_\mathrm{bcg}$) and k-fiber intensities ($I_\mathrm{k} = I_\mathrm{k+bcg} - I_\mathrm{bcg}$). All measurements were performed on randomly selected bundles in single z-planes, after determining that no other microtubules were crossing the area of measurement. Additionally, intensity of astral microtubules on STED images was measured using the 25x25 pixel Square tool (ImageJ). The background was determined by measuring empty area between the two astral microtubules and it was subtracted from astral microtubule intensity ($I_\mathrm{a} = I_\mathrm{a+bcg} - I_\mathrm{bcg}$).

In parallel analysis, tubulin intensities of the bridging and k-fiber on confocal images were measured in a single z plane using the Segmented Line tool (ImageJ) by drawing a 5-pixel thick line along the contour of k-fibers and the corresponding bridging fiber. The background was measured in the same z plane by drawing the 5-pixel thick line along the length of the metaphase midzone and the minimum value of the intensity profile was subtracted from the intensity values of bundle contours. The center of bridging fiber was determined as the minimum value of the mean tubulin intensities and it was set to distance zero µm. The final intensity of a bridging fiber ($I_b$) was calculated as the mean value of intensities in the area 500 nm around the center of the bridging fiber. The final intensity of a k-fiber region ($I_{bk}$), which also includes the bridging fiber, was calculated as an average of two mean values of intensities in the area 500 nm around the distance of 1.5 µm away from the center of the bridging fiber. The intensity value of k-fibers alone ($I_k$) was then calculated as $I_k = I_{bk} - I_b$.

### 3.8.3. Tracking and classification of segregation errors during anaphase in Mad2-depleted and Mad2/HAUS6-codepleted cells

Segregation errors in Mad2-depleted and Mad2/HAUS6-codepleted anaphase spindles were classified into misaligned kinetochores, lagging kinetochores and other errors. Misaligned kinetochores were kinetochore pairs situated outside the metaphase plate 30 s before anaphase onset. Lagging kinetochores were identified by stretched CENP-A signal and positioning in the central part of the spindle, outside the kinetochore mass that was moving towards the pole during anaphase. Finally, other segregation errors included kinetochores situated outside the moving kinetochore mass without stretched CENP-A signal, kinetochore pairs that remained completely unseparated for the whole duration of anaphase and kinetochore pairs in which both kinetochores remained non-stretched and in the central part of the spindle despite the initial separation.

Segregation errors were further divided based on their distance to the pole-to-pole axis into those in the inner ($< 0.5$ from the spindle axis) and the outer part ($\geq 0.5$ from the spindle axis) of the spindle. The distance of the kinetochore pair from the pole-to-pole axis was determined in 3D using a home written Matlab script and then normalized to spindle half-width determined using maximum intensity projections in ImageJ. All kinetochore pairs were manually tracked in time, from 30 sec before anaphase onset until entering the daughter cell by using the Point tool in ImageJ. Merotelic attachments on STED images were defined as those in which one kinetochore forms attachments with microtubules from the opposite side of the spindle, with no visible microtubule signal just below or above the kinetochore.

### 3.8.4. The interkinetochore distance in control and augmin-depleted cells

The interkinetochore distance was determined as a distance between the two points put on the centers of signal in each kinetochore pair using a Point tool in ImageJ. Kinetochore pairs were defined as those in the inner or the outer part of the spindle if their distance to the pole-to-pole axis was smaller or larger than the average distance of all tracked kinetochore pairs to the pole-to-pole axis, respectively.

### 3.8.5. Anaphase A and B speed and kinetochore tilt at anaphase onset in Mad2-depleted and Mad2/HAUS6-codepleted cells

To measure anaphase A speed, the coordinates of kinetochores and poles were tracked in time using the Point tool in ImageJ. The speed was calculated from the time point when the distance between the kinetochore and its closer pole started gradually decreasing. The slope of a regression line was determined for every kinetochore as the anaphase A speed. Anaphase B speed was calculated in a manner similar to anaphase A, but instead of kinetochores, the positions of poles were tracked in time with the first time frame determined as the frame when the distance between two poles started gradually increasing.

Anaphase onset was determined in a frame just before the interkinetochore distance of the tracked kinetochore pair started gradually increasing. The coordinates of kinetochore pairs that ended up as errors and of error-free kinetochore pairs were tracked along with the coordinates of spindle poles. The angle that the kinetochores form with the long spindle axis (tilt of kinetochores) was calculated using a home written Matlab script at the time point of anaphase onset.

### 3.8.6. Spindle architecture and dynamics in control and augmin-depleted cells

Spindle length, width and metaphase plate diameter were measured on maximum intensity projections of the side view z-stack of spindles. Spindle length was determined as distance between two poles (determined either by the center of Centrin 1 signal or the outermost points of the tubulin or PRC1 signal at the spindle pole). Spindle width was measured as the distance between two lines parallel to the long axis of the spindle and encompassing the outermost PRC1- or tubulin-labelled bundles. Additionally, in RPE1 cells stably expressing CENP-A-

GFP and Centrin1-GFP the metaphase plate diameter was measured as the distance between the outermost kinetochore pairs, whereas in HeLa PRC1-GFP it was measured as the distance between the outermost chromosome ends.

Overlap length was measured on sum intensity projections of 2–4 z-planes covering the entire bundle of interest, using ImageJ Segmented line tool by drawing a pole to pole line along the contour of PRC1-GFP and acquiring an intensity profile. The overlap length was defined as the length of the base of the PRC1-GFP intensity peak (Polak et al., 2017).

PRC1 intensity was measured in sum intensity projections of 10 central z-planes of the spindle. Total PRC1 signal in the cell was marked by using Polygon selection tool (ImageJ) and 5x5 Square tool was used to determine the background in the cytoplasm. The final intensity values were obtained using the following formula: PRC1 intensity = Integrated Density of the spindle – (Area of selected cell x mean fluorescence of background).

The side view z-stacks of spindles were transformed into an end-on view using previously written R script in R programming language in RStudio. The correction factor of 0.81 was used for the z-distance to correct for aberrations caused by the different refractive index mismatch of aqueous samples and immersion oil (Novak et al., 2018). The end-on view of the spindle was used to determine the number of bundles in HeLa and RPE1 PRC1-GFP cells by using sum intensity projections of 10 central z-planes covering 0.83 μm along the long spindle axis. Additionally, intensity profiles of PRC1-GFP were measured on the sum intensity projections of 10 central z-planes in an end-on view of the spindle by drawing a 50-pixel wide Straight line tool across the diameter of the spindle.

The shape of spindles was determined in ImageJ using a Point tool. Ten points were distributed throughout the bundle, with the first and last point positioned at the spindle poles. In control cells, only the outermost bundle was tracked. In HAUS6 siRNA-treated cells, three different groups of outermost bundles were tracked: bundles with visible bridging fibers, bundles with no visible bridging fibers and curved bundles extending far from the metaphase plate. Shape and curvature were calculated using a home-written MatLab script by fitting a circle to the tracked points along the bundle. Contour lengths of the bundles were measured by calculating the cumulative distance between the first and the last point of the tracked bundle.

For measuring the poleward flux rate, 10-pixel wide line was drawn from pole to pole along the bundle with photoactivation signal that lasted at least 5 time frames (40 s), using the Segmented Line tool in ImageJ. The position of photoactivated mark in each time frame was determined as the distance between the peaks of intensity profiles in photoactivation and SiR-tubulin channels for photoactivation mark and closer spindle pole, respectively. The analysis was performed on images processed with Gaussian Blur filter with Sigma set to 2 to improve the definition of the intensity profile peaks.

### 3.8.7. Classification of spindles and signal adjustment on two-color STED images of actin and microtubules

To analyse the spatial distribution of actin filaments and spindle microtubules during early prometaphase in fixed cells imaged by STED microscopy, spindles were categorized into two groups. The first group were spindles that had chromosome ring around the nascent spindle, a phase described in (Magidson et al., 2011). The second group consisted of elongated spindles, visible as two separated spindle poles on fixed images, but still had some kinetochores positioned away from the spindle body. Spindles that had all kinetochores attached to the spindle surface between the two poles were classified as late prometaphase spindles. Metaphase spindles were determined when all kinetochores were aligned to the metaphase plate.

When actin and microtubule signals between different treatments were compared, it was adjusted equally in control and treated cells. However, actin filaments were in some cases very faint, so the contrast in those representative images on figures was not always equally adjusted, as this led to important structures being either highly oversaturated or barely visible. It was instead adjusted so that all actin filaments are visible on STED images. These adjustments did not result in any structures being omitted or otherwise modified in a way that could lead to misrepresentation. Raw images were always used for quantification.

### 3.8.8. Intensity profiles of actin and microtubules measured from early prometaphase to metaphase

Intensity profiles of actin and microtubules were measured in early prometaphase elongated spindles, late prometaphase and metaphase spindles in ImageJ. Intensity profiles were measured on single z-planes of spindles by drawing a 50- or 100-pixel wide Straight line tool throughout the spindle midzone or across the pole to pole axis, respectively. To measure intensity profiles of actin and microtubules in the astral region, single z-planes of the spindles were used to draw a 50-pixel wide line by Segmented line tool across the astral microtubules on early prometaphase spindles with chromosome ring. The raw values of signal intensities are shown on graphs, unless stated otherwise.

### 3.8.9. Quantification of astral microtubules colocalizing with actin filaments

To determine the percentage of astral microtubules colocalizing with actin filaments, up to 15 randomly selected astral microtubules, consisting either of a single microtubule or a few of them, were analysed in early prometaphase spindles with a chromosome ring, late prometaphase and metaphase spindles. Analysis was done on single z-planes of spindles and only astral microtubules originating from the spindle pole were selected. Astral microtubule was defined to colocalize with actin if an actin filament was found adjacent to or on the microtubule along at least 50% of its length.

### 3.8.10. Quantification of spindle microtubules colocalizing with actin filaments and vice versa during late prometaphase and metaphase

To determine the percentage of spindle microtubules colocalizing with actin filaments and vice versa, up to 10 microtubule bundles or actin filaments spanning through metaphase plate area were selected in late prometaphase and metaphase spindles. Analysis was done on single z-planes of spindles. Microtubule bundles consisted either of two k-fibers and a bridging fiber, one k-fiber and the bridging fiber or a sole bridging fiber. Actin signal was classified into the three groups: actin filaments directly colocalizing with microtubules, actin filaments adjacent to microtubules and actin mesh visible as a diffuse actin signal above the background signal. Background for actin signal was determined by drawing the 20-pixel square by using Rectangle tool in ImageJ in the metaphase plate area where no microtubule or actin filaments were detected. Microtubules and actin were determined to colocalize with each other if at least 50% of their length was colocalizing with actin and microtubules, respectively. Additionally, percentage of k-fibers and bridging fibers colocalizing with actin was analysed by selecting up to 4 microtubule bundles in the spindle, each consisting of two k-fibers and the corresponding bridging fiber. K-fibers and bridging fibers were determined to colocalize with actin if actin signal was present along k-fibers or in the area between the two k-fibers, respectively.

### 3.8.11. Quantification of kinetochores with and without actin filaments

To determine the percentage of kinetochores with and without actin filaments, up to 20 randomly selected kinetochores were analysed in single z-planes of spindles. Kinetochores with actin were defined when actin filament or actin mesh was found adjacent to or attached to the kinetochore. On the other hand, kinetochores without actin were defined if no actin filament or mesh was in its close proximity. Additionally, intensity profiles of actin, microtubules and kinetochores were measured for kinetochore pairs found in metaphase. Up to 4 kinetochore pairs with its corresponding k-fibers and bridging fiber were analysed on single z-planes of metaphase spindles and 20-pixel thick line was drawn along the contour of k-fibers and the corresponding bridging fiber by using Segmented line tool in ImageJ. The background was measured in the same z plane by drawing the 20-pixel square by using Rectangle tool in ImageJ. Tubulin background was determined in the cytoplasm near the spindle, while actin background was determined in the metaphase plate area where no other filaments were present. For actin background, 4 randomly positioned squares were drawn and average value was calculated. Background values for tubulin and actin were subtracted from their raw intensity values. All intensity values were then normalized to the maximum value. The midpoint between the two kinetochores was set to zero.

### 3.8.12. Determining the mitotic duration, pole movements and focusing and segregation errors in control and cells treated with actin inhibitors

To determine the time from nuclear envelope breakdown to anaphase onset on lattice light-sheet movies, CENP-A or H2B signals in RPE1 cells were analysed. Nuclear envelope breakdown was determined in one frame before CENP-A signal started moving centripetally towards the future spindle or one frame before H2B signal started condensing. Anaphase onset was determined in one frame before the distance between kinetochores or chromosomes within a pair, marked by CENP-A or H2B signal, started gradually increasing in time, respectively. To determine the spindle length in metaphase, the distance between the two centrin signals was measured in one frame before anaphase onset. Only bipolar spindles were used for measuring the spindle length. Bipolar spindles were defined as those with two visible centrin signals in RPE1 cells stably expressing CENP-A-GFP and Centrin1-GFP. In RPE1 cells stably expressing Centrin-GFP H2B-eGFP mCherry-tubulin, bipolar spindles were defined when two centrin signals colocalized with two focused tubulin signals at each pole. If there were more than two centrin signals and/or focused tubulin signals, spindles were defined as multipolar.

Abnormal pole movement during prometaphase and metaphase was defined when centrin signal started moving rapidly throughout the cytoplasm and away from the spindle. Time of pole focusing was determined in cells treated with centrinone from NEBD until the point when tubulin signal was focused into one point at the poles without centrin signal. Cells were defined as the ones with a splayed poles by inspecting tubulin signal through late prometaphase and metaphase. If cells entered anaphase with more than one focused tubulin signal on one of the poles, spindles were defined to have splayed poles. For focusing time, only cells that did not have splayed poles were considered. Segregation errors were assessed during the anaphase. Spindles with segregation errors were defined as the ones with visible CENP-A or H2B signal in the central part of the spindle and outside of segregating kinetochore/chromosome mass moving towards the pole. Additionally, if the cell entered anaphase with splayed poles, it was also defined to have segregation errors since the DNA signal was divided into at least three masses instead into two.

All analysed parameters were determined on maximum intensity projections of cells. If cells divided diagonally to the imaging plane or signal was not clear at any point, the parameters were not measured. For that reason, numbers of analysed cells are different throughout different panels in the same treatment. When centrinone treatment was performed as previously described, majority of cells had one centrin signal on one pole and zero on another (1:0 cells) (Wong et al., 2015). However, some cells also had a different number of centrin signals (1:1, 2:0 or 2:2 cells). Since centrin signal was sometimes faint and number of centrioles was difficult to determine, all cells were analysed for mitotic duration, abnormal pole movement, pole splaying and segregation errors. However, for pole focusing analysis, only cells in which was clearly visible that one pole has one centrin signal and the second pole has none centrin signals, were taken into account.

### 3.8.13. Spindle architecture after treatments with actin inhibitors

In both control cells and cells treated with different actin inhibitors, the spindle position within the cell was determined based on its distance from the cell membrane defined by the actin signal. If the spindle resided in the middle of the cell, its position was defined as the central position. Spindle position was determined as “one pole at edge” or “spindle along edge” if one pole or one side of the spindle was adjacent to the cell membrane, respectively. To determine the percentage of cells with dislocated spindle poles, the position of the centrin signal along with the corresponding tubulin signal was analysed. Poles were defined as dislocated when the centrin signal or centrin signal along with its corresponding astral microtubules was displaced away from the spindle body.

The metaphase plate was positioned symmetrically within the spindle if it was located at the midpoint ± 1 µm between the two centrosomes. If it was located more than 1 µm outside of the midpoint, it was defined as asymmetrically positioned. Additionally, metaphase plate position was determined with the respect to the long spindle axis, which was determined as a line passing through two spindle poles. To measure if metaphase plate is symmetrically positioned with respect to that, two points were put on each end of the metaphase plate end and the closest distance to the long spindle axis was determined. If the distance of each metaphase plate ends to the long spindle axis was equal ± 1 µm, it was defined as symmetrical. Otherwise, it was defined as asymmetrical.

# 4. RESULTS

Firstly, I will show results about the role of augmin in chromosome congression, spindle architecture and mitotic fidelity that are already published in my paper (Štimac et al., 2022), thus figures and text are taken and/or modified from that paper (eLife article is distributed under the terms of a Creative Commons Attribution License that permits unrestricted use and redistribution provided that the original author and source are credited).

## 4.1. Augmin is vital for the formation of uniformly arranged units consisting of two sister k-fibers connected by a bridging fiber

To overcome the limitations of confocal microscopy and explore the relationship between different classes of microtubules within the crowded metaphase plate area, I performed stimulated emission depletion (STED) superresolution imaging (Hell and Wichmann, 1994; Klar and Hell, 1999) of microtubules within the bipolar metaphase spindles of human cells (Figure 21A-C). This enabled me to easily distinguish between k-fibers that start at kinetochores and midplane-crossing microtubules that pass through the central part of the spindle. HAUS6 or HAUS8 components of the augmin complex were depleted by siRNA in hTERT-RPE1 (hereafter referred to as RPE1) cells stably expressing CENP-A-GFP and immunostained for tubulin (Figure 21A). Augmin depletion was confirmed using immunocytochemistry and western blot analysis (Figure 22A-C).

In cells treated with control siRNA (hereafter referred to as control cells), the vast majority of midplane-crossing microtubule bundles laterally attached to a pair of sister k-fibers and formed a bridging fiber between them, consistent with previous findings (Kajtez et al., 2016; Vukušić et al., 2017). These bridging fibers were nearly-parallel with respect to one another and the spindle axis. Additionally, a small portion of midplane-crossing microtubules formed a secondary connection between a k-fiber on one side and a non-sister k-fiber on the other side (O'Toole et al., 2020). In comparison with untreated cells, midplane-crossing microtubules after HAUS6 or HAUS8 depletion extended at a variety of angles, and were wavy and disordered, particularly in the inner part of the spindle close to the pole-to-pole axis. Strikingly, midplane-crossing microtubules less often formed bridging fibers that connect to sister k-fibers in cells depleted of HAUS6 or HAUS8. Instead, they formed more complex arrangements, primarily consisting of one or more connections between various k-fibers within the metaphase spindle. This was contrary to k-fibers which, even though often missing a bridge between them, appeared relatively similar to those in control cells (Figure 21B-C). Taken together, augmin is vital for the proper organization of midplane-crossing microtubules into uniformly arranged bridging fibers that connect two sister k-fibers and extend nearly-parallel to the spindle axis.

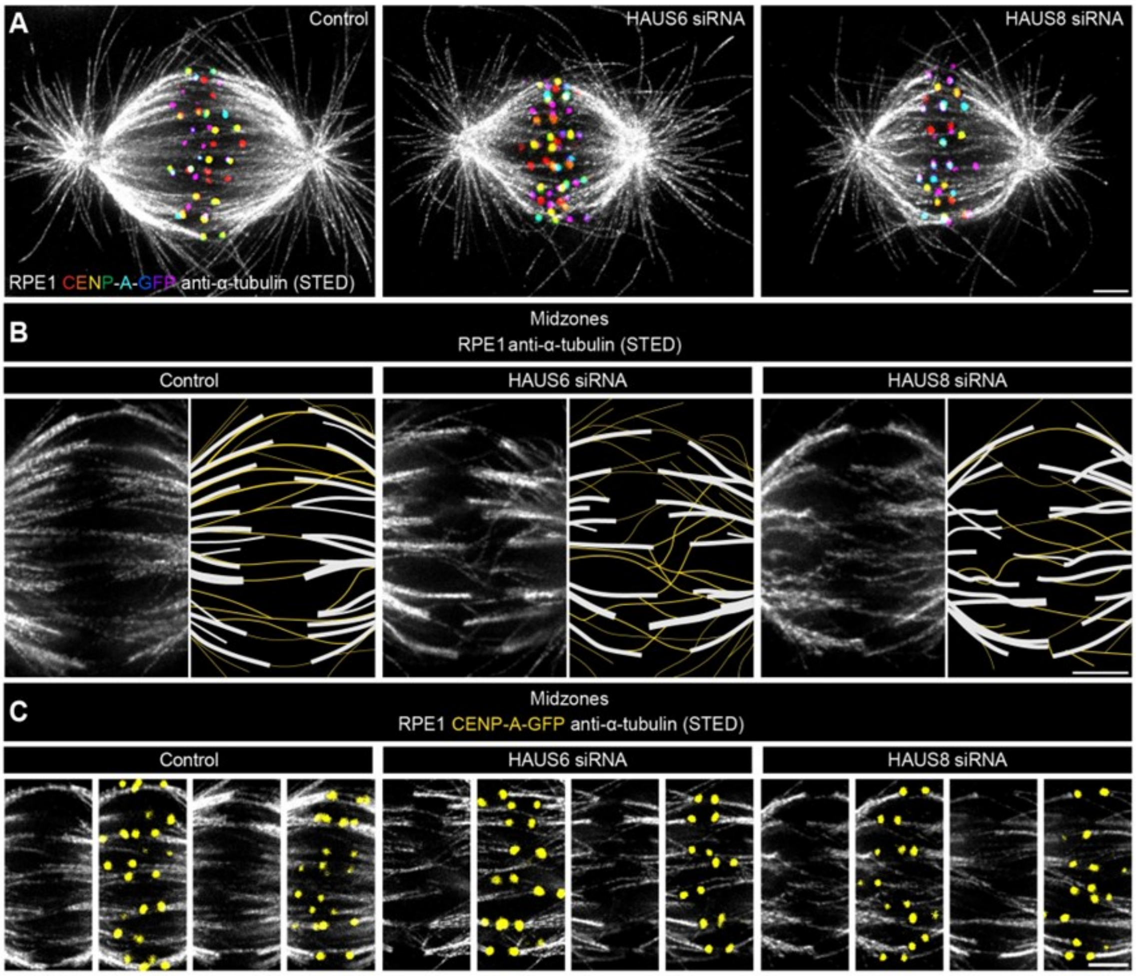

**Figure 21. Augmin ensures the proper formation of entities consisting of bridging fibers that connect two sister k-fibers.** (A) STED superresolution images of microtubules immunostained for α-tubulin (gray) in control (left), HAUS6- (middle), and HAUS8-depleted (right) RPE1 cells stably expressing CENP-A-GFP (rainbow, confocal). Images show maximum intensity projections of 6 central z-planes of metaphase spindles. Kinetochores are color-coded for depth from blue to red with the Spectrum LUT in ImageJ. (B) and (C) Insets of STED superresolution images of microtubules (gray) in spindle midzones of control (left), HAUS6- (middle) and HAUS8-depleted (right) RPE1 cells stably expressing CENP-A-GFP (yellow, panel C). Images show a single z-plane and do not correspond to midzones of spindles in panel (A). (B) Next to each image is the schematic representation of the microtubules in the midzone, with white lines representing k-fiber microtubules and yellow lines representing midplane-crossing microtubules. All images are adjusted for clarity based on the intensity of astral microtubules in each image (see Materials and methods). Scale bars, 2 µm.

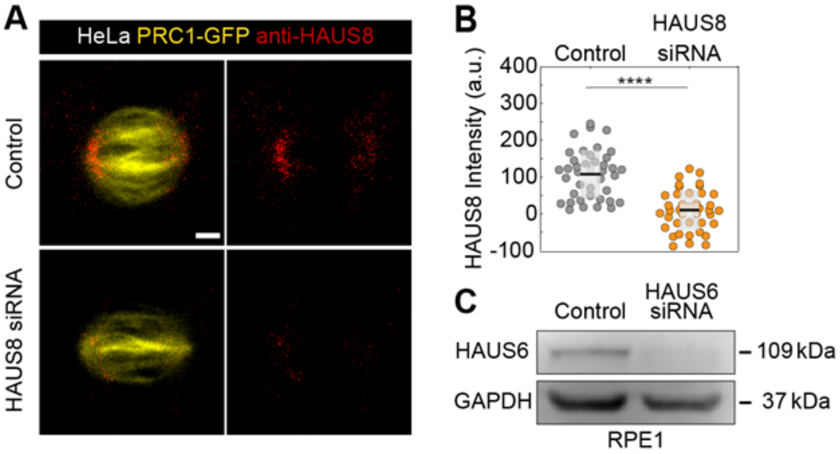

**Figure 22. Immunocytochemistry and western blot analysis confirming depletion of augmin**. (A) Fixed control and HAUS8 siRNA-treated HeLa cells stably expressing PRC1-GFP (yellow) and immunostained for or HAUS8 (red). Chromosomes were stained with DAPI (not shown) to identify cells in metaphase. Images are sum intensity projections of nine central z-planes. (B) Univariate scatter plot of HAUS8 intensities in control cells (gray) and cells depleted of or HAUS8 (orange). The intensity of HAUS8 in siRNA-treated cells is reduced by 82 ± 16% compared to control cells. Boxes represent standard deviation (dark gray), 95% confidence interval of the mean (light gray) and mean value (black). (C) Immunoblot analysis of HAUS6 siRNA treatment efficiency in RPE1 cells stably expressing CENP-A-GFP and Centrin1-GFP. HAUS6 antibody was used to validate the efficiency of knockdown, with GAPDH as the loading control. The representative image of three independent experiments is shown. All results were obtained from three independent experiments. Statistical analysis in (B) t-test; p-value legend: <0.0001 (****), 0.0001–0.001 (***), 0.001–0.01 (**), 0.01–0.05 (*), ≥0.05 (ns). Scale bars, 2 µm.

## 4.2. Augmin helps both prevent and resolve segregation errors through joint action of bridging and k-fibers

The appearance of disordered midplane-crossing microtubules in the metaphase plate area of spindles without augmin prompted me to investigate whether these microtubules affect mitotic fidelity. Augmin depletion has previously been linked to higher incidence of segregation errors (Almeida et al., 2022; Viais et al., 2021; Wu et al., 2008), but their origin remained largely unexplored due to extensive mitotic delays in augmin-depleted cells (Wu et al., 2008). To avoid mitotic delays, I performed live-cell confocal imaging for which I codepleted the checkpoint protein Mad2 together with HAUS6 to induce anaphase onset, and used Mad2-depleted cells (Mayr et al., 2007), which have only a few segregation errors, as a control (Figure 23A). To explore the mechanistic origin of segregation errors, I divided them into three distinct groups: misaligned chromosomes in which both kinetochores were found outside the metaphase plate just before anaphase onset, lagging chromosomes in which the kinetochore is visibly stretched and positioned in the central part of the spindle while other kinetochores are already separating, and other less common and diverse errors (Figure 23A–B, See Materials and methods).

The treatment with Mad2 siRNA resulted in a total of 1.5±0.2 segregation errors per cell (all data are given as mean ± SEM). However, the effect was significantly more severe when Mad2 was codepleted with HAUS6, resulting in a total of 5.7±0.8 segregation errors per cell (Figure 23B). Tracking of sister kinetochores in live-cell videos revealed that the number of misaligned kinetochore pairs per cell was similar in both Mad2 depletion and Mad2/HAUS6 codepletion (Figure 23B), which is why I presume they appeared due to Mad2 depletion independently of HAUS6 depletion. Nevertheless, they were much more likely to missegregate in cells without HAUS6, where 80 ± 9% of kinetochore pairs jointly segregated into the same cell, compared to only 20 ± 13% in control cells (Figure 23B). Interestingly, lagging kinetochores were both more frequent and more likely to missegregate in cells with Mad2/HAUS6 codepletion, in which there were 2.6±0.4 lagging kinetochores per cell, and 45 ± 6% of all lagging kinetochores ultimately missegregated. In contrast, there were only 0.8±0.2 lagging kinetochore pairs per cell in Mad2 depletion, and 77 ± 8% of them segregated correctly (Figure 23B). Finally, errors classified as others were more frequent in cells with Mad2/HAUS6 codepletion when compared to those with Mad2 depletion, but not more prone to missegregation (Figure 23B).

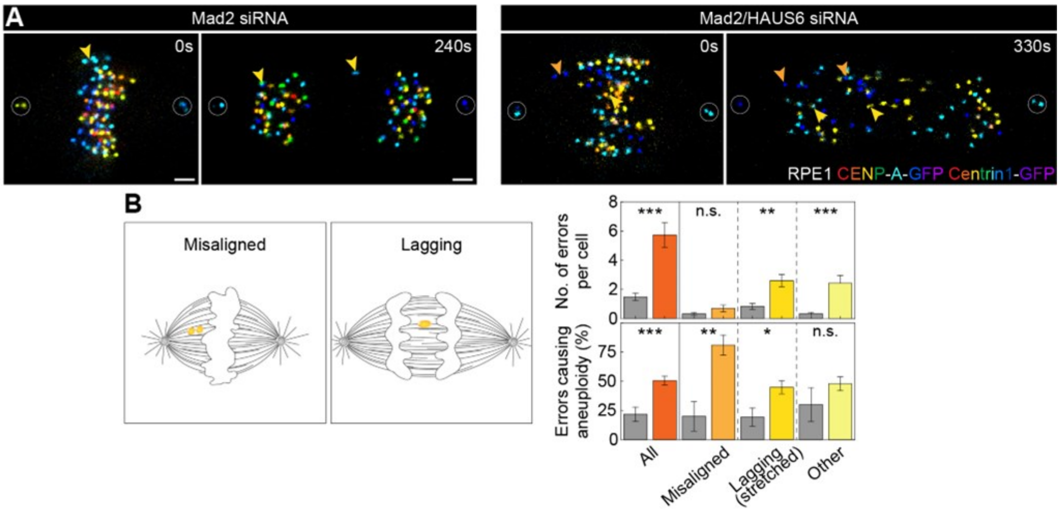

**Figure 23. Augmin-nucleated microtubules ensure proper chromosome segregation during anaphase and prevent aneuploidy.** (A) Time-lapse images of RPE1 cells stably expressing CENP-A-GFP and Centrin1-GFP (rainbow, confocal) in Mad2-depleted cells (left) and Mad2/HAUS6-codepleted cells (right). Yellow arrows represent lagging kinetochores and orange arrows misaligned kinetochores. Kinetochores are color-coded for depth from blue to red with the 16 Colors LUT in ImageJ. (B) The number of segregation errors per cell (top) and the percentage of errors causing aneuploidy (bottom) in Mad2-depleted cells (gray) and Mad2/HAUS6-codepleted cells (dark orange, light orange, dark yellow, light yellow). All segregation errors (dark orange) are divided into three groups: misaligned (light orange), lagging (dark yellow) and other (light yellow). Schematic representations next to the graph represent misaligned kinetochores (left) and lagging kinetochore (right). The number of errors in Mad2-depleted cells - in total 46 errors in 22 out of 31 cells; 10 misaligned kinetochore pairs in 9 out of 31 cells; 26 lagging kinetochores in 16 out of 31 cells; 10 other errors in 9 out of 31 cells. Number of errors in Mad2/HAUS6-codepleted cells - in total 172 errors in 25 out of 30 cells; 21 misaligned kinetochore pairs in 11 out of 30 cells; 78 lagging kinetochores in 23 out of 30 cells; 73 other errors in 20 out of 30 cells. Aneuploidy in Mad2-depleted cells - in total 11/46 errors in 22 out of 31 cells; 2/10 misaligned kinetochore pairs in 9 out of 31 cells; 6/26 lagging kinetochores in 16 out of 31 cells; 3/10 other errors in 9 out of 31 cells. Aneuploidy in Mad2/HAUS6-codepleted cells - in total 47/172 errors in 25 out of 30 cells; 17/21 misaligned kinetochore pairs in 11 out of 30 cells; 35/78 lagging kinetochores in 23 out of 30 cells; 35/73 other errors in 20 out of 30 cells. All results were obtained from three independent experiments. Statistical analysis in (B) Mann–Whitney U test (number of errors per cell) and Fisher's exact test (% of errors causing aneuploidy); p-value legend: <0.0001 (****), 0.0001–0.001 (***), 0.001–0.01 (**), 0.01–0.05 (*), ≥0.05 (ns). Scale bars, 2 µm.

As misaligned chromosomes appeared equally frequently in Mad2 depletion and Mad2/HAUS6 codepletion, but differed in their ability to correctly segregate, I used them as a tool to isolate the role of augmin in resolving segregation errors during anaphase. Consistent with previous findings (Uehara et al., 2009), both poleward movement of kinetochores during anaphase A and spindle elongation during anaphase B were reduced following Mad2/HAUS6 codepletion (Figure 24A-C). To analyse in detail the movement of misaligned kinetochore pairs, I tracked both kinetochores with respect to the proximal and distal pole, that is the pole which is closer to the misaligned kinetochore pair or the pole which is further away from it, respectively. The kinetochore closer to the proximal pole approached the proximal pole during anaphase A both after Mad2 depletion and Mad2/HAUS6 codepletion, thereby moving towards the pole to which it should segregate in both cases (Figure 24D). However, the kinetochore further away from the proximal pole usually remained stagnant for a short period of time, and afterwards typically moved towards the distal pole and accurately segregated as a ‘lazy’ kinetochore (Sen et al., 2021) in Mad2-depleted cells. In contrast, the kinetochore further away from the proximal pole experienced a short stagnation period and then typically moved away from the pole to which it should segregate, thereby missegregating in Mad2/HAUS6-codepleted cells (Figure 24E-H). As the interkinetochore distance of both correctly and incorrectly segregating misaligned kinetochore pairs in Mad2/HAUS6-codepleted cells was similar (Figure 24F), the absence of biorientation is unlikely to be the cause of missegregation for these kinetochores. Instead, missegregation likely occurs due to k-fibers with fewer microtubules (Almeida et al., 2022; Uehara et al., 2009; Zhu et al., 2008) creating insufficient force to move the kinetochore towards the distal pole (Dudka et al., 2018), against the movement of neighboring kinetochores and the corresponding chromosome mass which travel towards the proximal pole (Figure 23A).

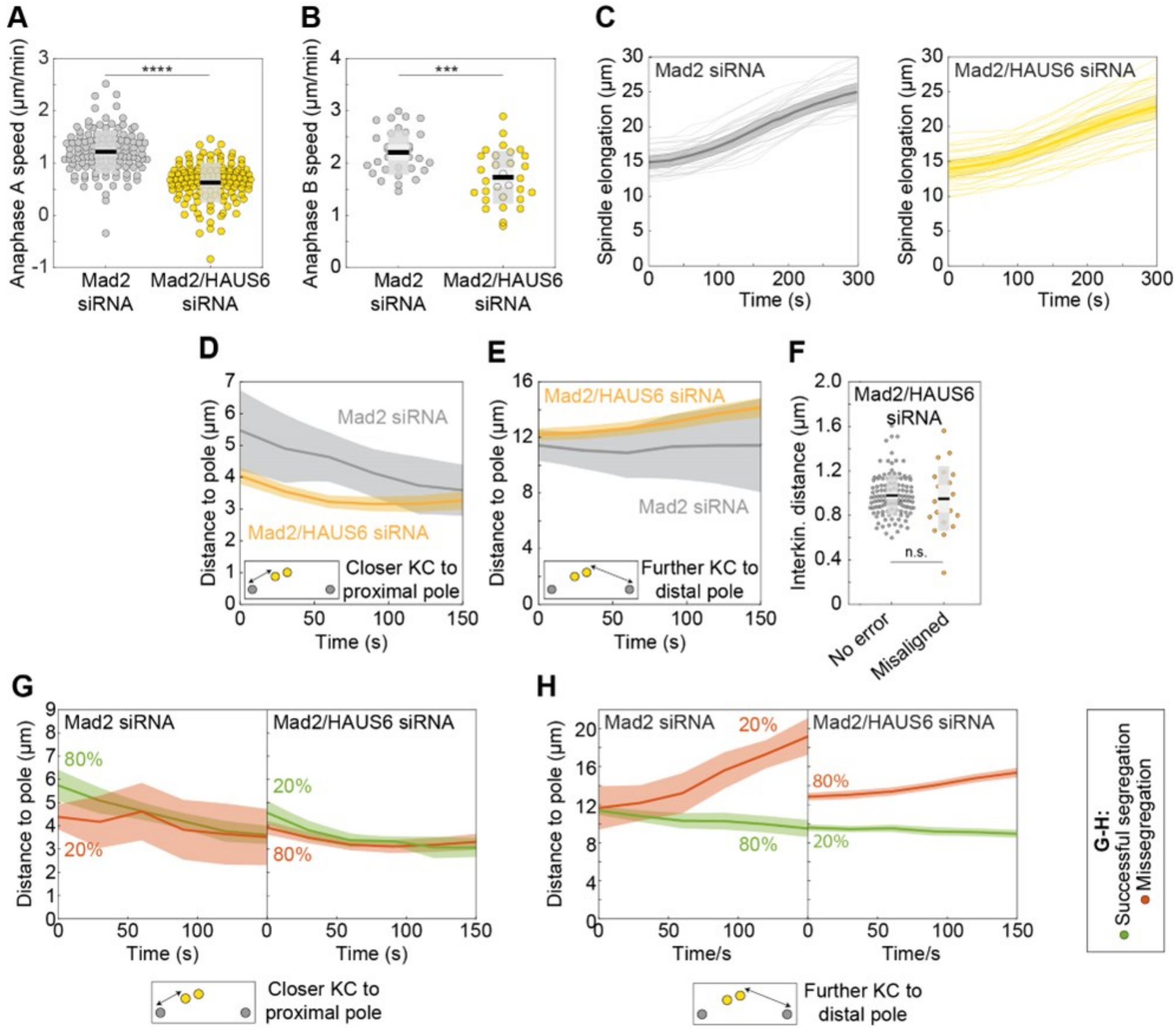

**Figure 24. Fewer microtubules in k-fibers upon augmin depletion cause missegregated kinetochores.** (A) Univariate scatter plot of anaphase A speed, defined as the distance of kinetochore and the closer pole in time, for Mad2-depleted (gray) and Mad2/HAUS6-codepleted (yellow) RPE1 cells stably expressing CENP-A-GFP and Centrin1-GFP. The anaphase A speed in Mad2-depleted cells is 1.2±0.04 µm/min, and in Mad2/HAUS6 codepleted cells 0.6±0.03 µm/min. N=120 kinetochores from 30 cells in both treatments. (B) Univariate scatter plot of anaphase B speed, defined as the distance between two poles in time, for Mad2-depleted (gray) and Mad2/HAUS6-codepleted cells (yellow). The anaphase B speed in Mad2-depleted cells is 2.2±0.08 µm/min, and in Mad2/HAUS6-codepleted cells 1.7±0.09 µm/min. N=31 Mad2-depleted cells and N=30 Mad2/HAUS6-codepleted cells. (C) A plot of spindle elongation in time following Mad2 depletion (gray) and Mad2/HAUS6 (yellow) codepletion. (D) The distance of closer kinetochore to the proximal pole and (E) further kinetochore to the distal pole of misaligned kinetochore pairs in time for Mad2-depleted (gray) and Mad2/HAUS6-codepleted cells (orange). The insets show the positions of kinetochores

**Figure 24. [continued from the previous page]** (yellow) with respect to spindle poles (gray). (F) Univariate scatter plot of the interkinetochore distance of error-free kinetochore pairs (gray) and misaligned kinetochore pairs (orange) in Mad2/HAUS6-codepleted cells. N=30 cells and 120 error-free kinetochore pairs in Mad2-depleted cells and N=30 cells and 21 misaligned kinetochore pairs in Mad2/HAUS6-codepleted cells. (G) A plot of distance of the misaligned kinetochore that is closer to the proximal pole in time following Mad2 depletion (left) and Mad2/HAUS6 (right) codepletion. (H) A plot of distance of the misaligned kinetochore that is further away from the proximal pole in time following Mad2 depletion (left) and Mad2/HAUS6 (right) codepletion. Kinetochore pairs in (G) and (H) are divided based on their outcome in anaphase into those that successfully segregated (green) and those that missegregated (red). Insets show schematic representations of the distance of closer and further kinetochore (yellow) to their corresponding spindle pole (gray). (A, B and F) Boxes represent standard deviation (dark gray), 95% confidence interval of the mean (light gray) and mean value (black). (C, D, E, G and H) Values are shown as mean (dark line) and SEM (shaded areas). All results were obtained from three independent experiments. Statistical analysis (A and F) Mann–Whitney U test; (B) t-test; p-value legend: <0.0001 (****), 0.0001–0.001 (***), 0.001–0.01 (**), 0.01–0.05 (*), ≥0.05 (ns).

Whereas lagging chromosomes have been previously observed following augmin depletion (Almeida et al., 2022; Viais et al., 2021; Wu et al., 2008), their origin remains unknown. Because I observed that disorganized midplane-crossing microtubules were often concentrated in the inner part of the mitotic spindle near the main spindle axis upon augmin depletion (Figure 11B-C), I decided to investigate the spatial distribution of lagging kinetochores in Mad2-depleted and Mad2/HAUS6-codepleted cells (Figure 25A) to see if their increased number might be connected to this phenotype. In Mad2-depleted cells, all lagging kinetochore pairs were situated in the outer half of the spindle just before anaphase onset. Remarkably, in Mad2/HAUS6-codepleted cells, 19 ± 5% of all lagging kinetochore pairs were situated in the inner part of the spindle just before anaphase onset (Figure 25A), where disordered midplane-crossing microtubules most frequently appeared. Thus, organization of midplane-crossing microtubules into bridging fibers might play an important role in mitotic fidelity.

To further explore how this compromised spindle geometry affects lagging kinetochores, I measured their interkinetochore distance just before anaphase onset. The lagging kinetochore pairs in Mad2/HAUS6-codepleted cells had an interkinetochore distance of 0.89±0.03 μm, which was significantly smaller than the interkinetochore distance of 0.98±0.02 μm measured in error-free kinetochore pairs (Figure 25B). This was not the case for lagging kinetochore pairs in Mad2-depleted cells which had an interkinetochore distance of 1.10±0.05 μm, similar to the interkinetochore distance of 1.05±0.02 μm measured in error-free kinetochore pairs (Figure 25B). Distinctly reduced interkinetochore distance of lagging kinetochore pairs following Mad2/HAUS6 codepletion suggests that they appear due to compromised spindle architecture being unable to maintain adequate kinetochore tension.

As sister k-fibers in the disorganized spindle region were sometimes diagonally positioned with respect to the pole-to-pole axis, I decided to test if this tilt is also connected to the appearance of segregation errors by measuring the angle that either lagging or error-free kinetochores form with the spindle axis just before anaphase onset. As for the interkinetochore distance following Mad2/HAUS6 codepletion, lagging kinetochore pairs were different from error-free kinetochore pairs, the tilt of which was 19.7±1.6° and 10.9±0.8°, respectively (Figure 25C). In contrast, in Mad2-depleted cells with preserved spindle geometry there was no difference between lagging kinetochore pairs with the tilt of 8.2±1.5° and error-free kinetochore pairs with the tilt of 8.9±0.6°, which was also similar to the tilt of 10.9±0.8° measured for error-free kinetochore pairs following Mad2/HAUS6 codepletion (Figure 25C). The tilt of kinetochores inversely correlated with the interkinetochore distance in augmin depletion, but not in control cells (Figure 25D). These data indicate the importance of nearly parallel configuration of kinetochore pairs during metaphase for mitotic fidelity, and points to the augmin-specific cause of lagging kinetochores that likely arise due to compromised and tilted bundle architecture facilitating the formation of merotelic attachments. Indeed, I found merotelic attachments in HAUS6-depleted cells imaged using STED microscopy, with most kinetochores forming an attachment with the microtubule from the opposite side of the mitotic spindle, while missing a proper bridging fiber (Figure 25E). To further test the nature of the observed attachments, I combined STED microscopy with cold treatment to remove midplane-crossing microtubules and preserve only kinetochore microtubules (DeLuca et al., 2006; Sacristan et al., 2018; Silkworth et al., 2011), which allowed me to confirm their true merotelic nature (Figure 25F). Interestingly, my live-cell imaging experiments reveal that augmin is required not only to prevent the formation of merotelic attachments in metaphase, but also to resolve them in anaphase, as a larger percentage of lagging kinetochore pairs ends up missegregating in Mad2/HAUS6 codepletion than in Mad2 depletion (Figure 23B). This suggests that the insufficient force provided by k-fibers with fewer microtubules (Dudka et al., 2018), which is responsible for missegregation of misaligned kinetochore pairs following augmin depletion, also leads to inability to resolve merotelic attachments during anaphase.

Altogether, I propose that augmin ensures mitotic fidelity through the joint action of bridging and k-fibers. While augmin-nucleated bridging fibers prevent merotelic attachments by creating a nearly parallel and highly bundled spindle geometry unfavorable for creating additional attachments, augmin-nucleated k-fibers produce robust force required to resolve any potentially appearing errors during anaphase (Figure 25G).

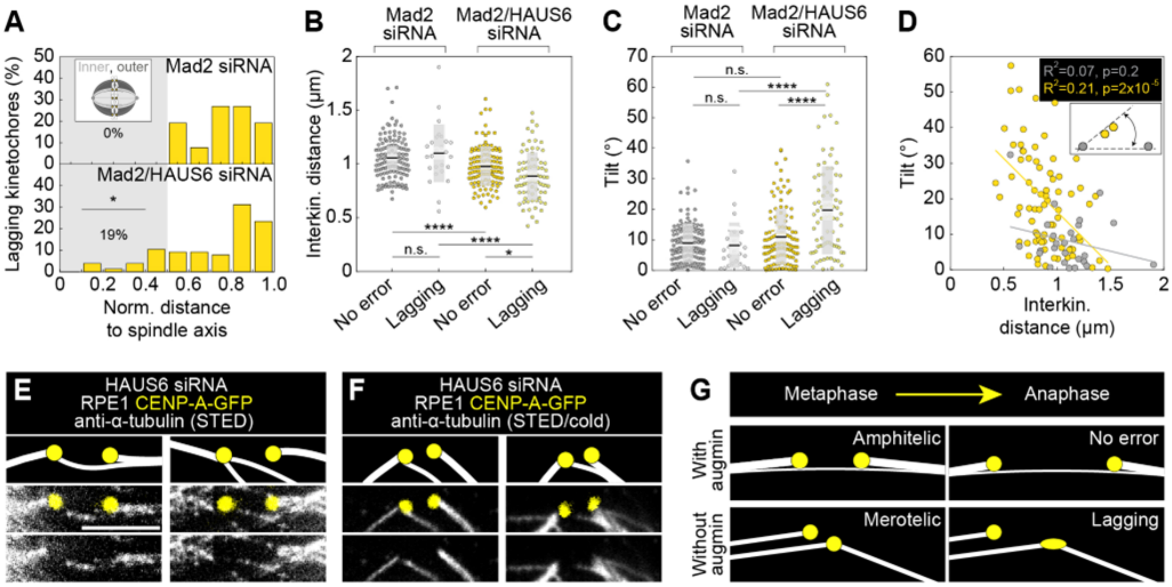

**Figure 25. Augmin-nucleated midplane-crossing microtubules prevent kinetochore tilt and thus merotelic attachments.** (A) The percentage of lagging kinetochores in Mad2-depleted (top) and Mad2/HAUS6-codepleted RPE1 cells stably expressing CENP-A-GFP and Centrin1-GFP (bottom) divided by their location with respect to the pole-to-pole axis into inner and outer (schematic representation shown as inset, see Materials and methods). (B) Univariate scatter plot of the interkinetochore distance of error-free and lagging kinetochore pairs in Mad2-depleted (gray) and Mad2/HAUS6-codepleted cells (yellow). (C) Univariate scatter plot of the angle that the error-free and lagging kinetochore pairs form with the pole-to-pole axis (tilt) in Mad2-depleted (gray) and Mad2/HAUS6-codepleted cells (yellow). N=31 cells and 124 error-free and 26 lagging kinetochore pairs from Mad2-depleted cells. N=30 cells and 120 error-free and 78 lagging kinetochore pairs from Mad2/HAUS6-codepleted cells. (D) The correlation of the tilt and the interkinetochore distance for Mad2-depleted (gray) and

**Figure 25. [continued from the previous page]** Mad2/HAUS6-codepleted cells (yellow). Inset shows schematic representation of the tilt (kinetochores are shown in yellow and spindle poles in gray). (E) The insets of kinetochore pairs with merotelic attachments in RPE1 cells stably expressing CENP-A-GFP (yellow, confocal) and immunostained for α-tubulin (gray, STED). (F) The insets of kinetochore pairs from cells as in (E) but exposed to cold treatment. Images in (E) and (F) are smoothed with 0.5-mm-sigma Gaussian blur and adjusted for clarity (see Materials and methods). Schematic representations in (E) and (F) are shown above the insets for better visualization of merotelic microtubule attachments. (G) The schematic representations of a kinetochore pair with amphitelic attachment in metaphase that does not cause any segregation errors during anaphase when augmin is present (top) and a kinetochore pair with merotelic attachment in metaphase that ends up as the lagging kinetochore during anaphase when augmin is not present (bottom). (B and C) Boxes represent standard deviation (dark gray), 95% confidence interval of the mean (light gray) and mean value (black). Statistical analysis (A) Fisher's exact test; (B and C) ANOVA with the post-hoc Tukey test; (D) linear regression; p-value legend: <0.0001 (****), 0.0001–0.001 (***), 0.001–0.01 (**), 0.01–0.05 (*), ≥0.05 (ns). Scale bars, 2 µm.

### 4.3. Bridging fibers are predominantly generated by augmin-dependent nucleation

As my visual assessment revealed that spindles without augmin have disorganized arrangements of midplane-crossing microtubules and often lack proper bridging fibers (Figure 21B-C), which were also missing at kinetochore pairs that formed merotelic attachments (Figure 25E), I set out to analyse how augmin-dependent microtubule nucleation contributes to the formation of bridging fibers in immunostained RPE1 cells imaged using STED microscopy (Figure 26A-B). Bridging fibers were strictly defined as midplane-crossing microtubules that connect two sister k-fibers, whereas k-fibers were defined as microtubules that start at kinetochores (Figure 26C). I measured tubulin signal intensity of randomly selected bridging ($I_b$) and k-fibers ($I_k$) which had no other microtubules in their immediate neighborhood, in a small square region between two kinetochores or at the pole-side of kinetochore, respectively (Figure 26C, see Materials and methods). By using the resulting tubulin signal intensities, I first estimated the number of microtubules in the bridging fiber in untreated RPE1 cells. Electron tomography of spindles in RPE1 cells showed that k-fibers consist of $n_k = 12.6 \pm 1.7$ microtubules (O'Toole et al., 2020). Thus, the bridging fiber consists of $n_b = I_b \times n_k / I_k = 3.8 \pm 0.4$ microtubules (for the explanation of $I_b$ and $I_k$ calculations, see Materials and methods). The accuracy of this calculation was additionally tested by measuring the intensity of astral microtubules, which presumably consist of single microtubules (McDonald et al., 1992). Indeed, using the number of microtubules in the k-fiber, my measurement of astral microtubule intensities showed that the astral microtubules consist of $n_a = 1.0 \pm 0.1$ microtubules (Figure 26D).

Quantification of STED images further revealed that HAUS6 depletion resulted in 68 ± 8% reduction of the bridging fiber signal intensity and 24 ± 6% reduction of the k-fiber signal intensity, with similar results obtained by HAUS8 depletion (Figure 26D–E). These data indicate that augmin depletion affects not only k-fibers, but even more so bridging fibers. The contribution of augmin to the nucleation of k-fibers was independently tested by measuring their intensity in spindles exposed to cold treatment in which bridging fibers are removed (Figure 27A). HAUS6 depletion resulted in a 37 ± 5% reduction of the k-fibers (Figure 27B), which is consistent with a previous study (Zhu et al., 2008) and comparable to values under non-cold conditions. Based on the measurements under non-cold conditions, I estimate that after HAUS6 depletion bridging fibers consist of 1.2±0.7 microtubules and k-fibers of 9.6±1.5 microtubules, which I interpret as microtubules nucleated in an augmin-independent manner. Thus, 2.6±0.7 microtubules in the bridging fiber and 3.0±0.9 microtubules in the k-fiber are nucleated in an augmin-dependent manner. To further validate my results, I performed live-cell confocal imaging with SiR-tubulin (Lukinavičius et al., 2014) and analysed the spindles by two independent methods (Figure 26F-J, See Materials and methods). Altogether, these results reveal that the augmin complex is a major nucleator of bridging fibers, whereas its contribution to the formation of k-fibers is significant but less prominent.

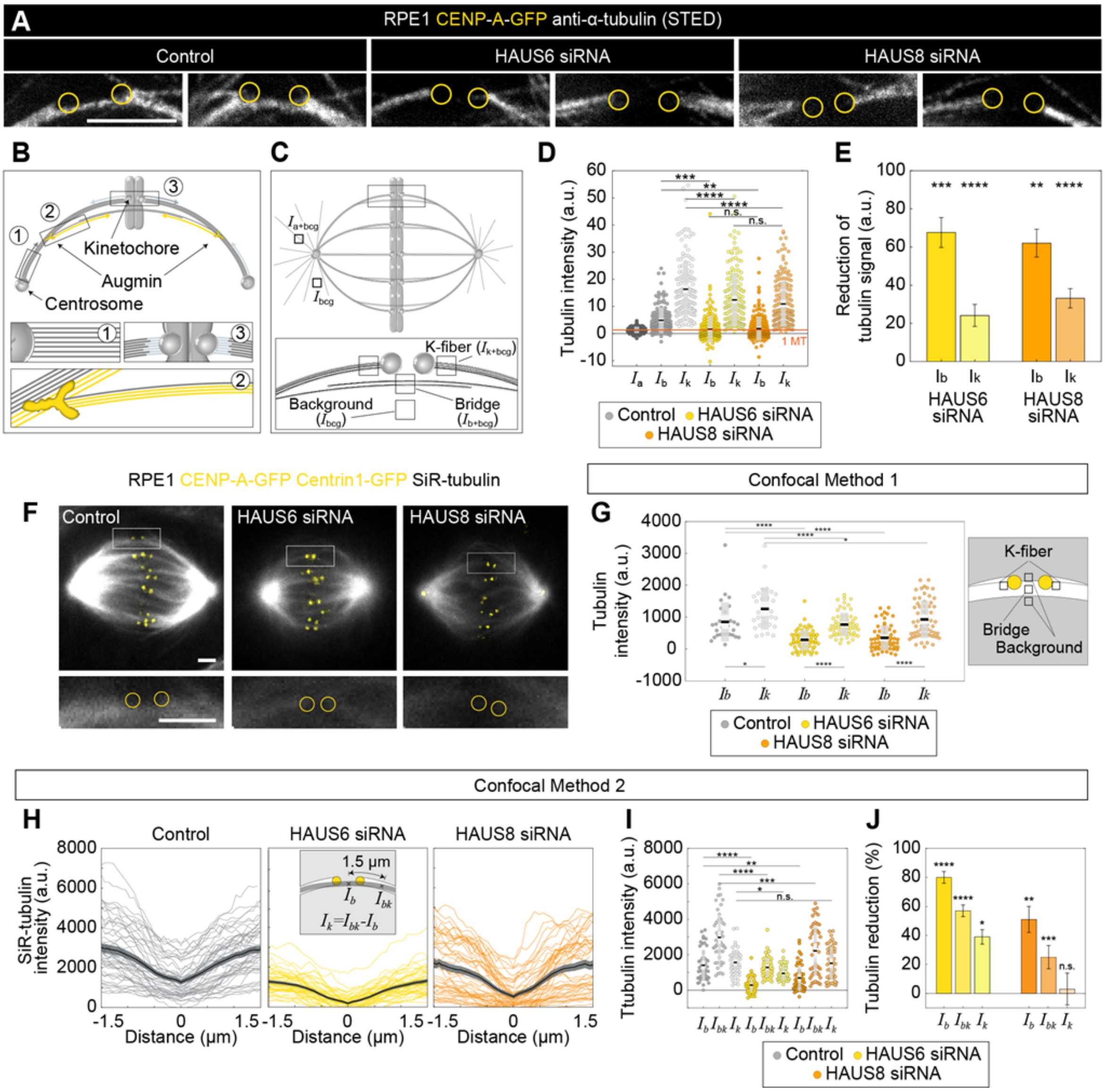

**Figure 26. Augmin is crucial for the nucleation of bridging microtubules.** (A) The insets of kinetochore pairs in RPE1 cells stably expressing CENP-A-GFP (not shown) immunostained for α-tubulin (gray, STED) in control cells (left) and after HAUS6 (middle) or HAUS8 (right) depletion. The insets demonstrate kinetochore pairs with bridging fibers affected by HAUS6 or HAUS8 depletion compared to bridging fibers in control cells. The positions of kinetochores are marked with yellow circles. (B) The schematic representation of three possible pathways of microtubule nucleation: (1) centrosome-dependent (2) augmin-dependent and (3) chromatin- and kinetochore-dependent nucleation. The augmin complex is shown in yellow. (C) Top: the schematic representation of the mitotic spindle in metaphase and the method used to measure the tubulin intensity of the astral microtubules. Small square regions were measured on microtubules extending from the spindle pole, corresponding to astral microtubules. Their background was measured in the empty area between the two astral microtubules, and it was

**Figure 26. [continued from the previous page]** subtracted from astral microtubule intensity. Bottom: Schematic representation of the method used to measure the tubulin intensity of the bridging and k-fiber. Small square regions were measured between two kinetochores or right next to the kinetochore, corresponding to bridging and k-fibers, respectively. The intensity of k-fibers was measured as an average of two sister k-fibers, and the average value of the background within the spindle was subtracted from all measurements. $I_{a+bcg}$ = intensity of astral microtubules with background, $I_{k+bcg}$ = intensity of k-fibers with background, $I_{b+bcg}$ = intensity of bridging microtubules with background, $I_{bcg}$ = intensity of background. (D) Univariate scatter plot of tubulin signal intensities of astral microtubules in control cells (reference value, dark gray, $I_a$), and bridging fibers ($I_b$) and k-fibers ($I_k$) in control cells (gray), HAUS6- (yellow) and HAUS8-depleted cells (orange). (E) The reduction of tubulin signal in the bridging fiber ($I_b$) and the k-fiber ($I_k$) following HAUS6 (yellow) or HAUS8 (orange) depletion, values are shown as mean ± SEM. p-Values were calculated using the absolute values of tubulin signal intensity of bridging or k-fibers following HAUS6 or HAUS8 depletion, compared to the absolute values of tubulin signal intensity of corresponding fibers in control cells. (D) and (E) N=30 cells and 90 astral microtubules in control cells, 158 bridging and sister k-fibers in control and 180 bridging and sister k-fibers in HAUS6- and HAUS8 siRNA-treated cells. (F) Live images (single z-plane) of SiR-tubulin (gray) stained metaphase spindles in control (left), HAUS6- (middle) and HAUS8-depleted (right) RPE1 cells stably expressing CENP-A-GFP and Centrin1-GFP (both in yellow). The enlarged boxes show bridging fibers affected by HAUS6 or HAUS8 depletion compared to the bridging fiber in control cell. The positions of kinetochores are marked with yellow circles. Images in are adjusted for clarity (see Materials and methods). (G) Univariate scatter plot of the tubulin signal intensities of bridging and k-fibers in control (gray), HAUS6- (yellow) and HAUS8-depleted (orange) RPE1 cells stably expressing CENP-A-GFP and Centrin1-GFP. Schematic representation of the method for measuring tubulin intensity of a bridging fiber and corresponding k-fibers (kinetochores are shown in yellow and tubulin signal in white). For the analysis, the average of two k-fibers is calculated and the average of background is subtracted from the tubulin intensity values of the bridging and k-fiber. N=30 bridging and sister k-fibers in 10 control cells and N=60 bridging and sister k-fibers in both 10 HAUS6- and 10 HAUS8-depleted cells. (H) Intensity profiles of SiR-tubulin signal along the bundles in control cells (gray) and after HAUS6 (yellow) or HAUS8 (orange) depletion. The center of the bridging fiber is set at a distance zero and the minimum intensity of the central part of the spindle was subtracted from the values of intensity profiles. N=10 cells and 50 bundles for control and HAUS6 siRNA-treated cells, N=10 cells

**Figure 26. [continued from the previous page]** and 48 bundles for HAUS8 siRNA-treated cells. Mean ± SEM (thick black line and shaded area, respectively). The method for measuring the tubulin intensity of the bridging fiber and the corresponding k-fibers is depicted in the inset; the average of two k-fibers was calculated whenever both k-fibers resided in the same-z plane. (I) Univariate scatter plot of the tubulin signal intensities of the bridging fiber ($I_b$), the bundle consisting of the k-fiber and bridging fiber ($I_{bk}$), and k-fiber ($I_k$) in control (gray), HAUS6- (yellow) and HAUS8-depleted (orange) cells. (J) Reduction of the tubulin signal in the bridging fiber ($I_b$), the bundle consisting of the k-fiber and bridging fiber ($I_{bk}$), and the k-fiber ($I_k$) following HAUS6 (yellow) or HAUS8 (orange) depletion. Values are shown as mean ± SEM. p-values were calculated using the absolute values of tubulin signal intensity of bridging or k-fibers following HAUS6 or HAUS8 depletion, compared to the absolute values of tubulin signal intensity of corresponding fibers in control cells. (D, G and I) Boxes represent standard deviation (dark gray), 95% confidence interval of the mean (light gray) and mean value (black). All results were obtained from three independent experiments. Statistical analysis ANOVA with post-hoc Tukey test, p-value legend:<0.0001 (****), 0.0001–0.001 (***), 0.001–0.01 (**), 0.01–0.05 (*), ≥0.05 (ns). Scale bars, 2 µm.

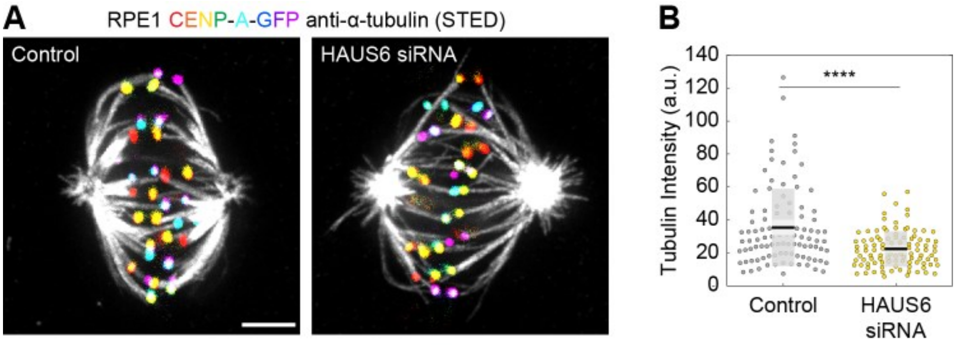

**Figure 27. Cold treatment as an independent method to determine augmin's role in microtubule nucleation within k-fibers.** (A) Maximum intensity projections of STED superresolution images of microtubules stained for α-tubulin (gray) in RPE1 cells stably expressing CENP-A-GFP (rainbow, confocal) in control cells (left) and HAUS6 siRNA-treated cells (right) exposed to cold treatment. (B) Univariate scatter plot of the tubulin signal intensities of k-fibers in control cells (gray) and upon HAUS6 depletion (yellow) in cells exposed to cold treatment. N=30 cells and 101 bundles in control cells and 102 bundles in HAUS6-depleted cells from 3 independent experiments. Boxes represent standard deviation (dark gray), 95% confidence interval of the mean (light gray) and mean value (black). Images are adjusted for clarity (see Materials and methods). Statistical analysis Mann–Whitney U test, p-value legend: <0.0001 (****). Scale bars, 2 µm.

Remarkably, 41 ± 4% of all kinetochore pairs in HAUS6-depleted cells had no detectable bridging fibers, defined as those with the tubulin signal below the background signal (see Materials and methods), and consistent with results obtained using visual inspection (Figure 28A). The majority of kinetochore pairs without bridging fibers were located in the inner part of the mitotic spindle, where as much as 50 ± 5% of all kinetochore pairs had undetectable bridging fibers after augmin depletion, compared to only 27 ± 5% in the outer part (Figure 28B), thus pointing to an irregular and more complex spatial distribution of bridging fibers in the inner part of the spindles following augmin depletion. Similar results were obtained from superresolution imaging after HAUS8 depletion (Figure 28B).

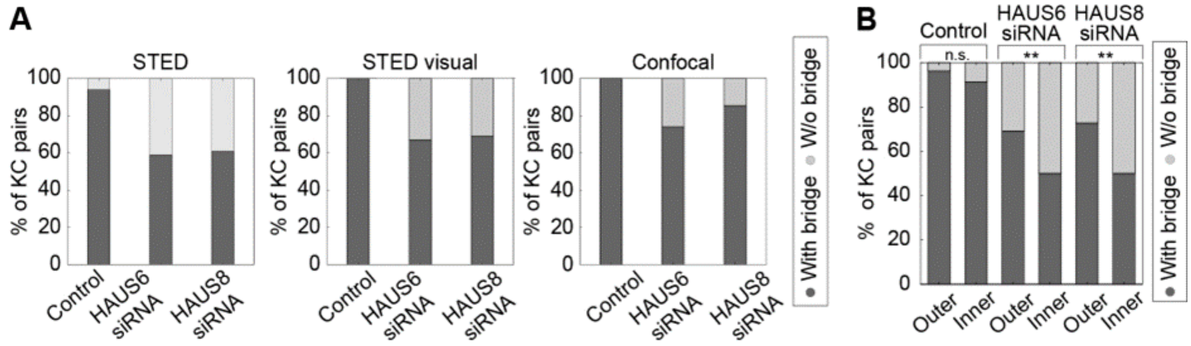

**Figure 28. Bridging fibers located in the inner part of the spindle are more affected upon augmin depletion.** (A) The fractions of kinetochore pairs with bridging fibers (dark gray) and with undetectable bridging fibers (light gray). The fractions are obtained from the tubulin intensity measured in STED images (left), by visual inspection of STED images (middle) and from SiR-tubulin intensity measured in confocal images (right) of control, HAUS6- and HAUS8-depleted RPE1 cells stably expressing CENP-A-GFP cells. (B) The fractions of kinetochore pairs with bridging fibers (dark gray) and with undetectable bridging fibers (light gray) in control, HAUS6- and HAUS8-depleted cells. Kinetochore pairs are divided based on their location in the spindle into outer and inner (See Materials and methods and Results). All results were obtained from three independent experiments. Statistical analysis (B) chi-square test; p-value legend:<0.0001 (****), 0.0001–0.001 (***), 0.001–0.01 (**), 0.01–0.05 (*), ≥0.05 (ns).

The compromised microtubule nucleation following augmin depletion led to the impairment of overall spindle geometry, creating a unique system where three main types of interactions between k-fibers and bridging fibers can be found within the same spindle: (1) sister k-fibers attached to bridging fibers, (2) sister k-fibers without a bridging fiber, and (3) solitary, long, interpolar bundles without associated kinetochores. This is in contrast with control cells, where the first group dominates and the other two groups are rarely found (Polak et al., 2017). To gain insight into the contribution of each of these functionally distinct microtubule bundles to the maintenance of spindle geometry, I traced the outermost bundles in HAUS6 siRNA-treated RPE1 cells imaged using STED microscopy and fitted a circle to the bundle outline (Figure 29A, see Materials and methods). Whereas the bundles without kinetochores in HAUS6 siRNA-treated cells had a significantly longer contour when compared to all other bundle types (Figure 29B), k-fibers without bridging fibers in augmin-depleted cells had a significantly larger radius of curvature than any of the other bundle types in augmin-depleted or control cells

(Figure 29C). Taken together, the outer interpolar bundles without associated kinetochores are excessively long and make the spindle wider, whereas k-fibers lacking a bridging fiber are overly straight, ultimately resulting in a diamond-like shape of the spindle. This change in spindle shape in the absence of proper bridging fibers is consistent with the prediction of Tolić lab's theoretical model (Kajtez et al., 2016) and previous experiments (Jagrić et al., 2021).

In addition to spindle architecture, compromised microtubule nucleation following augmin depletion also affected spindle dynamics, as poleward flux in U2OS cells stably expressing CENP-A-GFP, mCherry-tubulin and photoactivatable-GFP-α-tubulin was significantly reduced (Figure 29D-E), in agreement with findings in Indian Muntjac cells (Almeida et al., 2022). Recent speckle microscopy experiments in RPE1 cells, which were able to separate the effect of augmin on poleward flux of bridging and k-fibers, revealed that both k-fibers and the remaining bridging fibers were significantly slowed down (Risteski et al., 2022). Bridging fibers fluxed faster than k-fibers in control and augmin-depleted cells (Risteski et al., 2022), supporting the model in which poleward flux is largely driven by sliding apart of antiparallel microtubules (Brust-Mascher et al., 2009; Mitchison, 2005; Miyamoto et al., 2004). I propose that augmin depletion results in slower flux of bridging fibers because the remaining bridging microtubules are likely nucleated at the poles, where microtubule depolymerization mechanisms might curb poleward flux speed (Ganem et al., 2005). In contrast, protein regulator of cytokinesis 1 (PRC1) depletion does not affect the flux (Risteski et al., 2022; Steblyanko et al., 2020) even though it reduces bridging fibers (Kajtez et al., 2016; Polak et al., 2017), possibly because the remaining bridging microtubules are generated away from the poles via augmin and can thus flux freely. In sum, augmin ensures proper architecture and dynamics of the metaphase spindle largely through the nucleation of bridging fibers, which link sister k-fibers and ensure their proper shape and function.

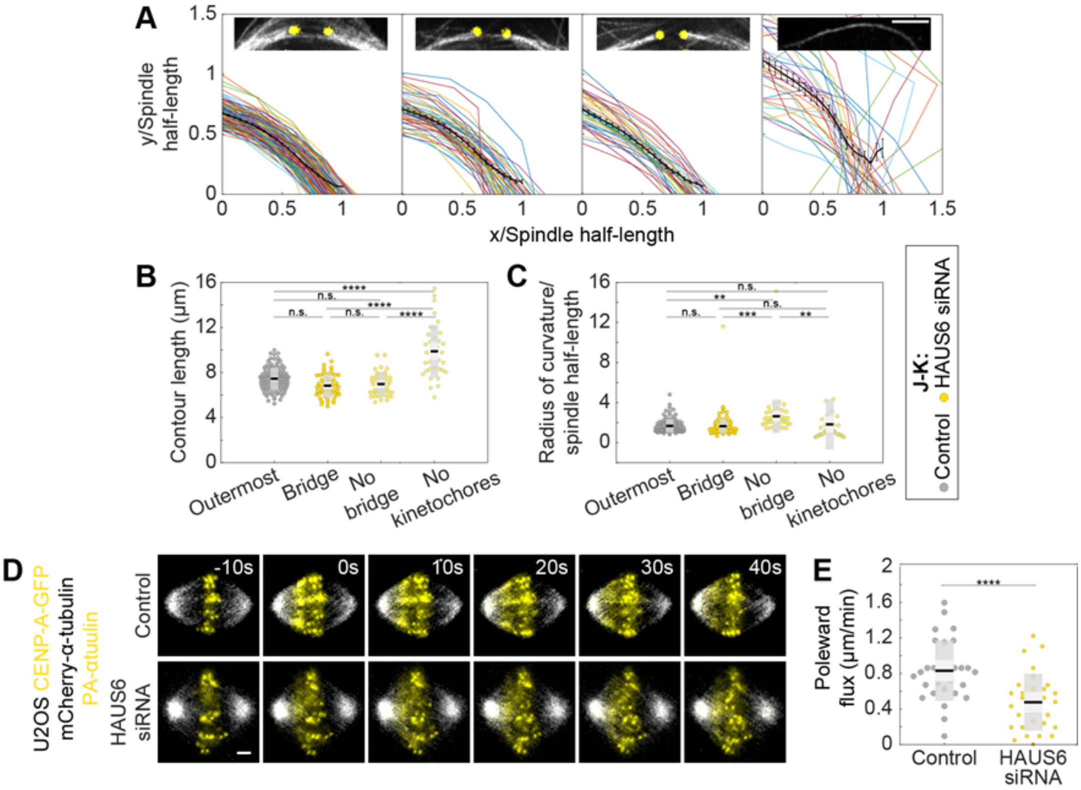

**Figure 29. Augmin depletion affects spindle architecture and dynamics.** (A) Bundle contours from RPE1 cells stably expressing CENP-A-GFP (yellow). Examples of each bundle type are shown in insets. From left to right: the outermost bundle in control cells, the outermost bundle with a bridging fiber, the outermost bundle without a bridging fiber and the outermost bundle without kinetochores in HAUS6-depleted cells; mean ± SEM is shown in black. (B) Univariate scatter plot of contour lengths and (C) radii of curvature in control (gray), HAUS6- (yellow) and HAUS8-depleted (orange) cells. N=120 outermost bundles from 30 control cells, 54 bundles with a bridging fiber, 40 bundles without a bridging fiber, and 36 bundles without kinetochores from 30 HAUS6-depleted cells. (D) Time-lapse images of control (top) and HAUS6-depleted (bottom) U2OS cells stably expressing CENP-A-GFP (yellow), mCherry-α-tubulin (gray) and PA-GFP-α-tubulin, before (–10 s), at the time when photoactivation (yellow) was performed (0 s), and after photoactivation. Images are adjusted for clarity (see Materials and methods). (E) Univariate scatter plot of the poleward flux speed in control cells (gray) and after HAUS6 depletion (yellow). N=30 measured photoactivation spots in 30 cells for both conditions. (B, C and E) Boxes represent standard deviation (dark gray), 95% confidence interval of the mean (light gray) and mean value (black). All results were obtained from three independent experiments. Statistical analysis (B and C) ANOVA with post-hoc Tukey test; (E) t-test, p-value legend:<0.0001 (****), 0.0001–0.001 (***), 0.001–0.01 (**), 0.01–0.05 (*), ≥0.05 (ns). Scale bars, 2 µm.

## 4.4. Augmin-depleted spindles contain fewer overlap bundles, which have longer overlap regions and are located at the spindle periphery

My finding that bridging fibers were more severely perturbed in the inner part of the spindle after augmin depletion prompted me to examine the spatial distribution of these midplane-crossing microtubules and their overlap regions throughout the spindle. I used PRC1 as a marker because it preferentially crosslinks overlap microtubules (Li et al., 2018; Mollinari et al., 2002), thus providing a specific label for bridging fibers (Polak et al., 2017). By taking a standard 'side view' of the spindle and rotating the 3D image stack of the spindle into an 'end-on' view, I was able to gain insight into the redistribution of bridging microtubules throughout the spindle cross-section in HeLa (Kajtez et al., 2016) and RPE1 (Asthana et al., 2021) cells stably expressing PRC1-GFP with and without MG-132 treatment (Figure 30A-B and Figure 31A). To compare their distribution to that of tubulin, I also rotated the 3D image stacks of the spindles in RPE1 cells stained with SiR-tubulin (Figure 30A-B) (Novak et al., 2018).

The signal intensity of PRC1-GFP bundles in RPE1 cells was reduced by 55 ± 4% following augmin depletion (Figure 30C). Consistently, the number of PRC1-labeled overlap bundles measured in an end-on view of spindles was almost halved; from 28±1 to 16±1 distinct bundles in control and HAUS6-depleted RPE1 cells, respectively (Figure 30D). Comparable trends were also observed in HeLa cells after depletion of HAUS6 or HAUS8 (Figure 31B-D).

The augmin-depleted cells showed a specific barrel-like distribution of the PRC1-GFP labeled bundles, with more overlap bundles being present around the perimeter of the spindle and fewer in the central part (Figure 30A 'end-on view' and 30E, Figure 31E). However, DNA was uniformly distributed throughout the spindle cross-section, both in augmin-depleted and control cells (Figure 30A 'end-on view'). In agreement with this result, kinetochores and tubulin signal were also found uniformly distributed over the spindle cross-section (Figure 30A 'end-on view' of RPE1 cells). This observation indicates that k-fibers are present and roughly uniformly distributed throughout the spindle cross-section and is in agreement with my finding that augmin primarily affects bridging fibers, while k-fibers are less perturbed (Figure 26).

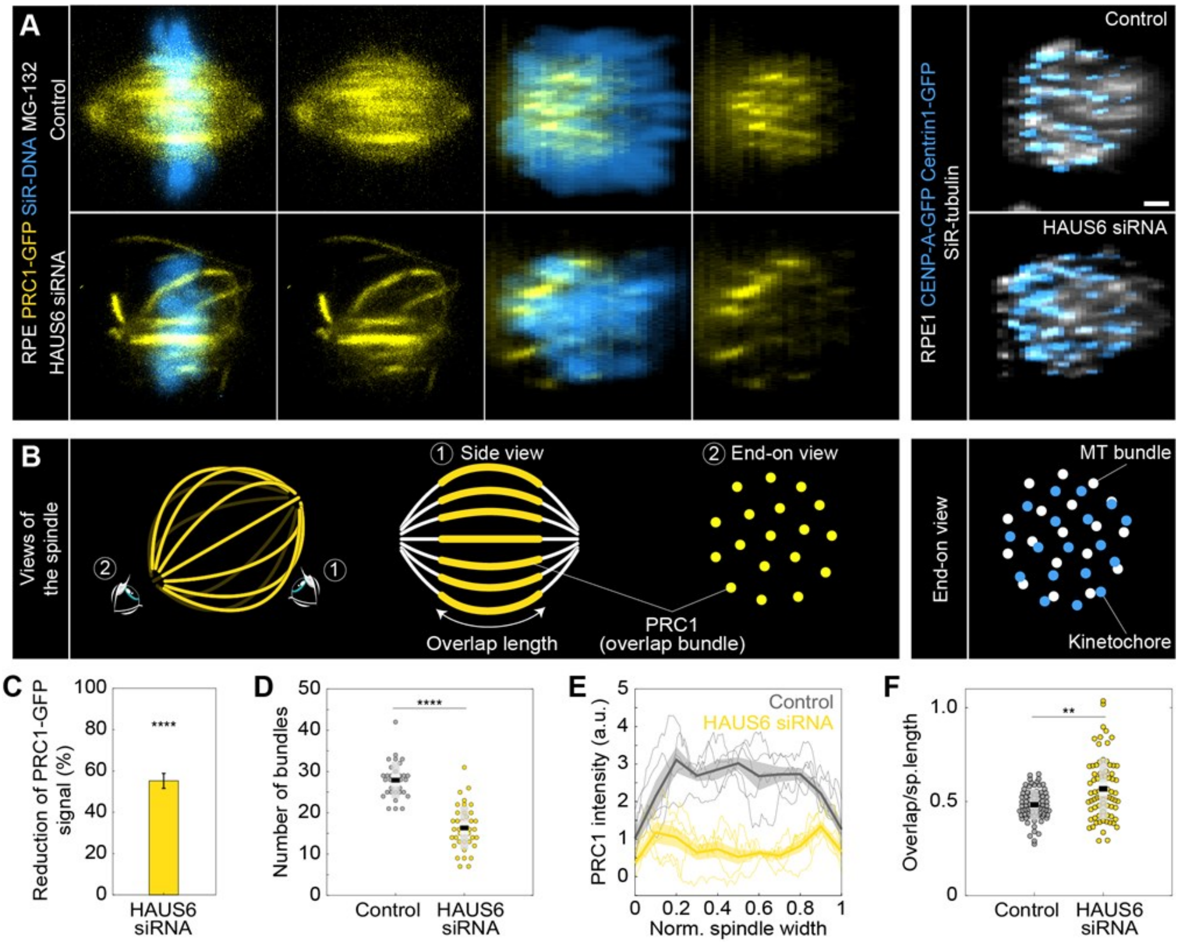

**Figure 30. Augmin-depleted spindles have fewer bridging fibers, which have larger overlap length and are located at the spindle periphery in RPE1 cells.** (A) The four columns on the left represent live images of metaphase spindles in MG-132-treated RPE1 cells stably expressing PRC1-GFP (yellow) and stained with SiR-DNA (blue) in control cells (top row) and after HAUS6 depletion (bottom row). 1st and 2nd column: side view of the spindle; 3rd and 4th column: end-on view of the same spindle, showing a barrel-like arrangement of PRC1-labeled bundles after augmin depletion. Images on the right show the end-on view of RPE1 cells stably expressing CENP-A-GFP and Centrin1-GFP (both in blue) and stained with SiR-tubulin (gray) in control cells (top) and after HAUS6 depletion (bottom). Side views are sum intensity projections of 10 central z-slices for RPE1 cells. End-on views are sum projections of 20 central z-slices ($\Delta z$=0.083 µm) for RPE1 cells. (B) Left: schematic representations of different views of the spindle. Eye signs mark the angle for the side view (1) and the end-on view (2). Side view was used to measure the length of overlap regions (yellow) and end-on view to determine the number of bundles (yellow dots). Right: schematic representation of the end-on view of RPE1 cells stably expressing CENP-A-GFP and Centrin1-GFP (blue dots) and stained with SiR-tubulin (gray dots). (C) The reduction of the PRC1 signal in RPE1 cells treated

**Figure 30. [continued from the previous page]** with MG-132 measured in sum intensity projection of 10 central z-slices following HAUS6 depletion. Values are shown as mean ± SEM. P-values were calculated using the absolute values of PRC1 signal intensity following HAUS6 depletion (N=39 cells), compared to the absolute values of PRC1 signal intensity in control cells (N=32 cells). (D) Univariate scatter plot of the number of bundles in RPE1 cells treated with MG-132 counted in the end-on view of the spindle in control cells (gray) and HAUS6-depleted cells (yellow). N=32 control cells and N=39 HAUS6-depleted cells. (E) The PRC1-GFP intensity profiles in RPE1 cells treated with MG-132 measured in the end-on view of the spindle in control cells (gray) and after HAUS6 depletion (yellow). The blue line in the inset marks the measured region (width: 2.5 µm). Mean (thick lines) and SEM (shaded areas). (F) Univariate scatter plot of overlap length divided by spindle length in RPE1 cells treated with MG-132 measured in the side view of the spindle in control cells (gray) and HAUS6-depleted cells (yellow). N=75 bundles in 32 control cells and N=74 bundles from 39 HAUS6-depleted cells. (D and F) Boxes represent standard deviation (dark gray), 95% confidence interval of the mean (light gray) and mean value (black). All results were obtained from three independent experiments. Statistical analysis (C, D and F) Mann–Whitney U test; p-value legend:<0.0001 (****), 0.0001–0.001 (***), 0.001–0.01 (**), 0.01–0.05 (*), ≥0.05 (ns). All images are adjusted for clarity so that all PRC1 bundles are visible in each cell (see Materials and methods). Scale bars, 2 µm.

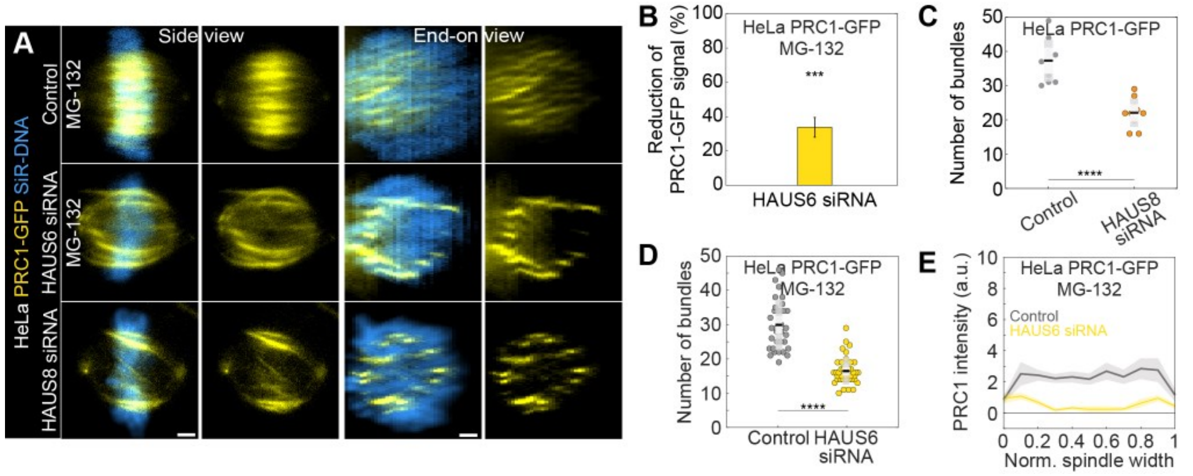

**Figure 31. Augmin-depleted spindles have fewer bridging fibers, which have larger overlap length and are located at the spindle periphery in HeLa cells.** (A) Four columns represent live images of metaphase spindles in HeLa cells stably expressing PRC1-GFP (yellow) and stained with SiR-DNA (blue) in control (top) and after HAUS6 (middle) or HAUS8 (bottom) depletion. Control and HAUS6-depleted cells are treated with MG-132. 1st and 2nd column: side view of the spindle; 3rd and 4th column: end-on view of the same spindle, showing a barrel-like arrangement of PRC1-labeled bundles after augmin depletion. Side views are sum projections of 5 central z-slices (Δz=0.5 µm) and end-on views are sum projections of 10 central z-slices (Δz=0.083 µm). (B) Reduction of the PRC1 signal in HeLa cells stably expressing PRC1-GFP and treated with MG-132, measured in sum intensity projection of 10 central z-slices following HAUS6 depletion. Values are shown as mean ± SEM. P-values were calculated using the absolute values of the PRC1 signal intensity following HAUS6 depletion (N=39 cells), compared to the absolute values of the PRC1 signal intensity in control cells (N=33 cells). (C) Univariate scatter plot of the number of PRC1-labeled bundles in HeLa cells stably expressing PRC1-GFP, counted in the end-on view of the spindle in control (gray), and HAUS8-depleted (orange) cells without MG-132 treatment. N=10 cells for all conditions. (D) Univariate scatter plot of the number of PRC1-labeled bundles in HeLa cells stably expressing PRC1-GFP treated with MG-132, counted in the end-on view of the spindle in control (gray) and HAUS6-depleted cells (yellow). N=32 control and 39 HAUS6-depleted cells. (E) The PRC1-GFP intensity profile in HeLa cells stably expressing PRC1-GFP and treated with MG-132, measured in the end-on view of the spindle in control cells (gray) and after HAUS6 (yellow) depletion. Mean (thick lines) and SEM (shaded areas). (C and D) Boxes represent standard deviation (dark gray), 95% confidence interval of the mean (light gray) and mean value (black). All results were obtained from three independent experiments. All images are

**Figure 31. [continued from the previous page]** adjusted for clarity (see Materials and methods). Statistical analysis (B and C) Mann-Whitney U test; (D) t-test; p-value legend:<0.0001 (****), 0.0001–0.001 (***), 0.001–0.01 (**), 0.01–0.05 (*), ≥0.05 (ns). Scale bars, 2 μm.

To explore the role of the observed overlap repositioning in defining the overall spindle geometry, I measured spindle width, the diameter of the metaphase plate, spindle length, and overlap length in RPE1 and HeLa cells (see Materials and methods). Despite the spindles being wider in both cell lines, the diameter of the metaphase plate was not larger, as the spindles widened due to the long, curved bundles without kinetochores (Figure 32A). While the spindles in RPE1 cells shortened following augmin depletion, those in HeLa cells were longer (Figure 32A), consistent with previous observations on Drosophila S2 cells and Xenopus egg extracts (Goshima et al., 2007; Petry et al., 2011). This difference in spindle length might be due to the overlaps remaining the same length after augmin depletion in RPE1 cells, while being longer and thereby able to push the spindle poles further apart in HeLa cells (Figure 32B). When both spindle length and overlap length were taken into account, the relative length of overlaps with respect to spindle length increased in RPE1 cells from 48±1% to 57 ± 2% following augmin depletion (Figure 30F), comparable to the increase in HeLa cells (Figure 32C-D). Altogether, these results suggest that augmin regulates both the width and length of metaphase spindles, while also restricting the portion of spindle length occupied by overlap microtubules.

Interestingly, the long curved bundles characteristic for augmin depletion (Goshima et al., 2008; Uehara et al., 2016; Wu et al., 2008; Zhu et al., 2008) exhibited PRC1 signal along most of their length, suggesting that they consist of antiparallel microtubules, even though contrary to bridging fibers, they form away from the k-fibers and kinetochores (corresponding to long, curved bundles in (Figure 21A and Figure 29A). These bundles likely arose either due to PRC1 crosslinking excessively long astral microtubules that were now able to reach the spindle midzone or due to PRC1 activity combined with the excess of free tubulin present as a consequence of less tubulin being incorporated in bridging and k-fibers. Altogether, the data suggest that there was an overall redistribution of PRC1 within the spindle from a large number of relatively short overlaps to a small number of relatively long overlaps. Thus, without augmin, the spindles are wider and contain fewer overlaps, which occupy a larger portion of spindle length and tend to accumulate at the spindle periphery.

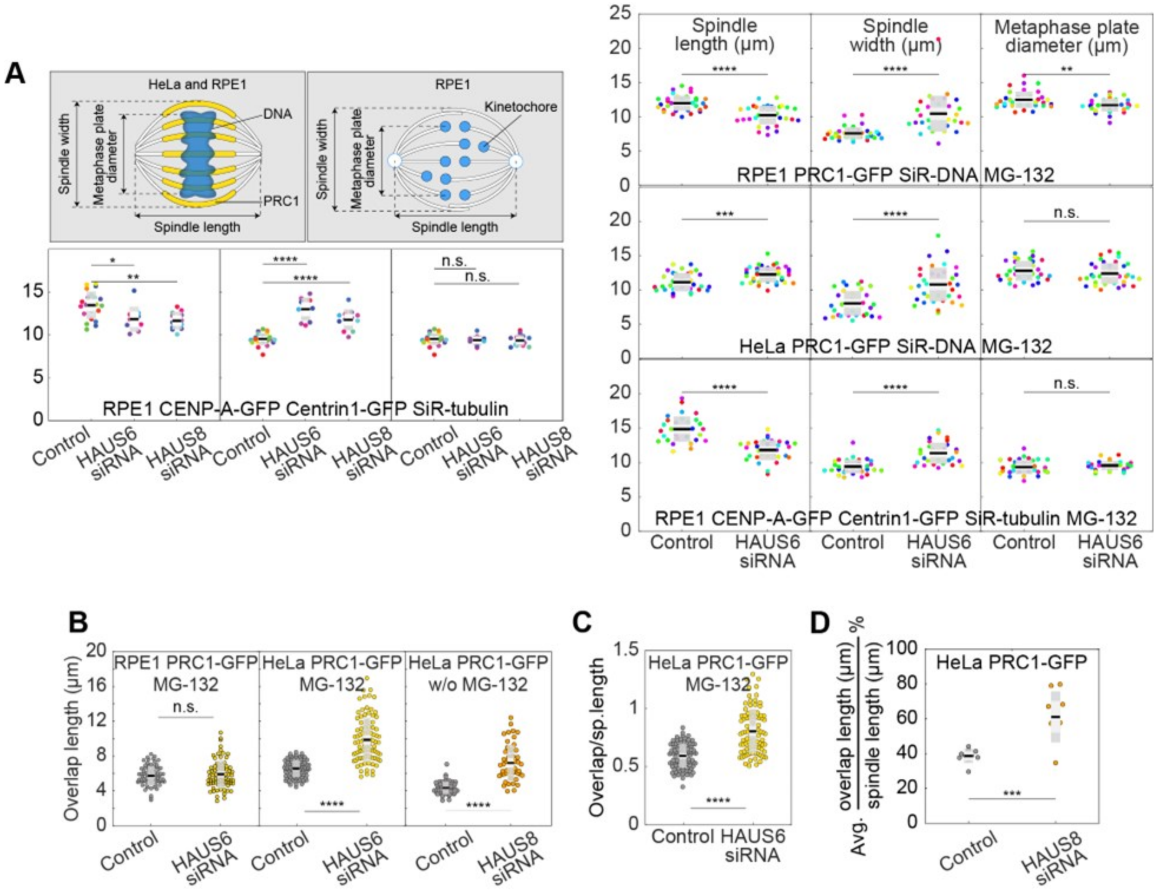

**Figure 32. Spindles without augmin are wider.** (A) Schematic representations of spindle geometry measurements in RPE1 and HeLa cells stably expressing PRC1-GFP (yellow) and stained with SiR-DNA (blue) and RPE1 cells stably expressing CENP-A-GFP and Centrin1-GFP (both in yellow) and stained with SiR-tubulin (white). Univariate scatter plots of the spindle length (left), width (middle) and diameter of the metaphase plate (right) are shown in this order on both left and right panels. The cell type from which the measurement was obtained is indicated in each panel. The measurements were taken in control, HAUS6- or HAUS8-depleted cells. Left panels show untreated cells and right panels represent cells treated with MG-132. Each color in the plot corresponds to data obtained in one cell. N=36 control cells and 33 HAUS6-depleted cells following MG-132 treatment of the RPE1 PRC1-GFP cell line; N=33 control cells and 38 HAUS6-depleted cells following MG-132 treatment of the HeLa PRC1-GFP cell line; N=31 control cells and 31 HAUS6-depleted cells following MG-132 treatment of the RPE1 CENP-A-GFP Centrin1-GFP cell line; N=10 control, HAUS6- and HAUS8-depleted RPE1 CENP-A-GFP Centrin1-GFP cells. (B) Overlap length measured in the side view of the spindle of control (gray) and HAUS6-depleted (yellow) RPE1 cells stably

**Figure 32. [continued from the previous page]** expressing PRC1-GFP and treated with MG-132 (left). N=72 overlaps in 32 control cells and 74 overlaps in 39 HAUS6-depleted cells. Overlap length measured in the side view of the spindle of control (gray) and HAUS6-depleted (yellow) HeLa cells stably expressing PRC1-GFP and treated with MG-132 (middle, left). N=96 overlaps in 33 control cells and 90 overlaps in 39 HAUS6-depleted cells. Overlap length measured in the side view of the spindle of control (gray) and HAUS8-depleted (orange) HeLa cells stably expressing PRC1-GFP without MG-132 treatment (right). N=50 overlaps in 10 cells for each condition. Each color in the plot corresponds to data obtained from one cell. (C) Univariate scatter plot of an overlap length divided by spindle length in control (gray) and HAUS6-depleted (yellow) HeLa cells stably expressing PRC1-GFP and treated with MG-132. N=96 overlaps in 33 control cells and 90 overlaps in 39 HAUS6-depleted cells. (D) Univariate scatter plot of an average overlap length divided by spindle length in control (gray) and HAUS8-depleted (orange) HeLa cells stably expressing PRC1-GFP. N=10 overlaps in 10 cells for each condition. (A-D) Boxes represent standard deviation (dark gray), 95% confidence interval of the mean (light gray) and mean value (black). All results were obtained from three independent experiments. Statistical analysis: t-test for samples that followed normal distribution or Mann–Whitney U test for samples that significantly departured from normality, determined using the Shapiro-Wilk test; p-value legend:<0.0001 (****), 0.0001–0.001 (***), 0.001–0.01 (**), 0.01–0.05 (*), ≥0.05 (ns).

### 4.5. The interkinetochore distance decreases preferentially in the inner part of the spindle and at kinetochores with weaker bridging fibers after augmin depletion

The interkinetochore distance, which is a readout of interkinetochore tension (Waters et al., 1996), decreases after augmin depletion (Uehara et al., 2009; Zhu et al., 2008). My measurements on RPE1 cells also showed a reduced interkinetochore distance in augmin-depleted cells (Figure 33A-D). This reduction of interkinetochore tension may be due to weaker k-fibers (Uehara et al., 2009; Zhu et al., 2008). However, I noticed that the interkinetochore distance was smaller in the inner part of the spindle in augmin-depleted cells (Figure 33A-C and 33E), where bridging fibers were most severely impaired (Figures 28B and 30A). This was not the case in control cells, which showed no difference in interkinetochore distance between the inner and the outer part of the spindle (Figure 33E). These findings motivated me to investigate a potential link between the lack of proper bridging fibers and the interkinetochore tension. I thus divided kinetochore pairs in STED images into two groups: (1) those with a bridging fiber (i.e. signal intensity of the bridging fiber above the background signal), and (2) those with undetectable signal intensities at the expected locations of bridging fibers, which I for simplicity refer to as kinetochore pairs without bridging fibers (Figure 33B–C). Remarkably, kinetochore pairs without bridging fibers had a significantly smaller interkinetochore distance than kinetochore pairs with bridging fibers (Figure 33F).

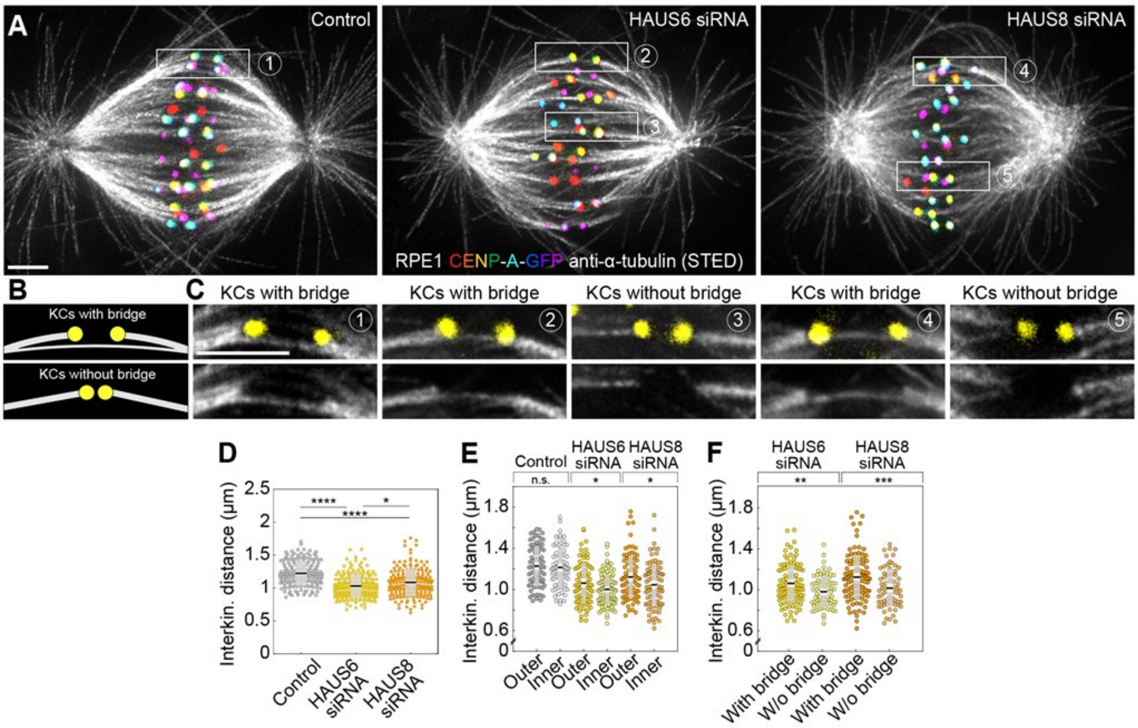

**Figure 33. The reduction of the interkinetochore distance after augmin depletion is related to the impairment of bridging fibers.** (A) STED superresolution images of microtubules immunostained for α-tubulin (gray) in control (left), HAUS6- (middle) and HAUS-8 depleted (right) RPE1 cells stably expressing CENP-A-GFP (rainbow, confocal). Images are maximum intensity projections and kinetochores are color-coded for depth from blue to red with the Spectrum LUT in ImageJ. (B) The schematic representation of a kinetochore pair (KCs) with (top) and without (bottom) bridging fiber (See Results). (C) Enlarged boxes show KCs with or without a bridging fiber in control (left), HAUS6- (middle), and HAUS8- (right) depleted RPE1 cells. Images represent single z-plane taken from spindles in (A) and smoothed with 0.75-mm-sigma Gaussian blur. Kinetochores are shown in yellow. (D) Univariate scatter plot of the interkinetochore distance in control (gray), HAUS6- (yellow) and HAUS8-depleted (orange) RPE1 cells stably expressing CENP-A-GFP and

**Figure 33. [continued from the previous page]** immunostained for α-tubulin. N=158 kinetochore pairs in 30 control cells and 180 kinetochore pairs in 30 HAUS6- and HAUS8-depleted cells. (E) Univariate scatter plot of the interkinetochore distance in control (gray), HAUS6- (yellow), and HAUS8- (orange) depleted cells with kinetochore pairs divided based on their distance from the long (pole-to-pole) spindle axis (outer kinetochore pairs shown in darker colors and inner in lighter colors). N=30 cells in all three conditions; 78 and 80 outer and inner kinetochore pairs for control, respectively; 84 and 96 outer and inner kinetochore pairs for HAUS6 depletion, respectively; 88 and 92 outer and inner kinetochore pairs for HAUS8 depletion, respectively. (F) Univariate scatter plot of the interkinetochore distance in HAUS6- (yellow) and HAUS8- (orange) depleted cells. Kinetochore pairs are divided into two groups: with bridging fiber (darker colors) and without bridging fiber (lighter colors). N=30 cells in HAUS6/8-depleted cells; 106 pairs with and 74 kinetochore pairs without bridging fibers in cells following HAUS6 depletion, respectively; 110 and 70 kinetochore pairs with and without bridging fibers in cells following HAUS8 depletion, respectively. (D-F) Boxes represent standard deviation (dark gray), 95% confidence interval of the mean (light gray) and mean value (black). All results were obtained from three independent experiments. Statistical analysis (D) ANOVA with post-hoc Tukey test; (E, F) t-test for samples that followed normal distribution or Mann–Whitney U test for samples that significantly departured from normality, determined using the Shapiro-Wilk test; p-value legend:<0.0001 (****), 0.0001–0.001 (***), 0.001–0.01 (**), 0.01–0.05 (*), ≥0.05 (ns). All images are adjusted for clarity based on the intensity of astral microtubules in each image (see Materials and methods). Scale bars, 2 μm.

Although this result suggests a role of bridging fibers in regulating interkinetochore distance, this effect may be indirect and arise due to k-fibers, as kinetochore pairs that lacked a bridging fiber typically had thinner k-fibers than those with a bridging fiber in augmin-depleted cells (Figure 34A). Hence, I used several approaches to separate the contribution of bridging and k-fibers to the interkinetochore tension. First, I found that although the interkinetochore distance correlated both with bridging and k-fiber intensity after augmin depletion, the correlation with bridging fiber intensity was stronger (Figure 34B-C). Such correlations were absent in control cells (Figure 34B-C). To explore a specific contribution of k-fibers to the interkinetochore tension, I divided the kinetochore pairs in augmin-depleted cells into two subsets, those with and without bridging fibers, and found that the interkinetochore distance did not correlate with k-fiber intensity within each group (Figure 34D), which argues against the k-fiber intensity as a sole determinant of interkinetochore tension. In agreement with this, when I selected two subsets of kinetochore pairs with either very strong or very weak k-fiber intensity but with comparable bridging fiber intensities (Figure 34E-F), I found no difference in the interkinetochore distance between these subsets (Figure 34G). Finally, to examine a specific contribution of bridging fibers, I identified two subsets of kinetochore pairs with similar k-fiber intensity values, one of which had bridging fibers and the other which did not (Figure 34H). I found that the interkinetochore distance was larger in the subset with bridging fibers than without (Figure 34I), indicating a specific effect of bridging fibers on interkinetochore tension. Analysis of live-cell confocal images of RPE1 cells yielded similar results (Figure 35A-D). Based on these data, I conclude that augmin has a significant role in regulating interkinetochore tension through the nucleation of bridging microtubules.

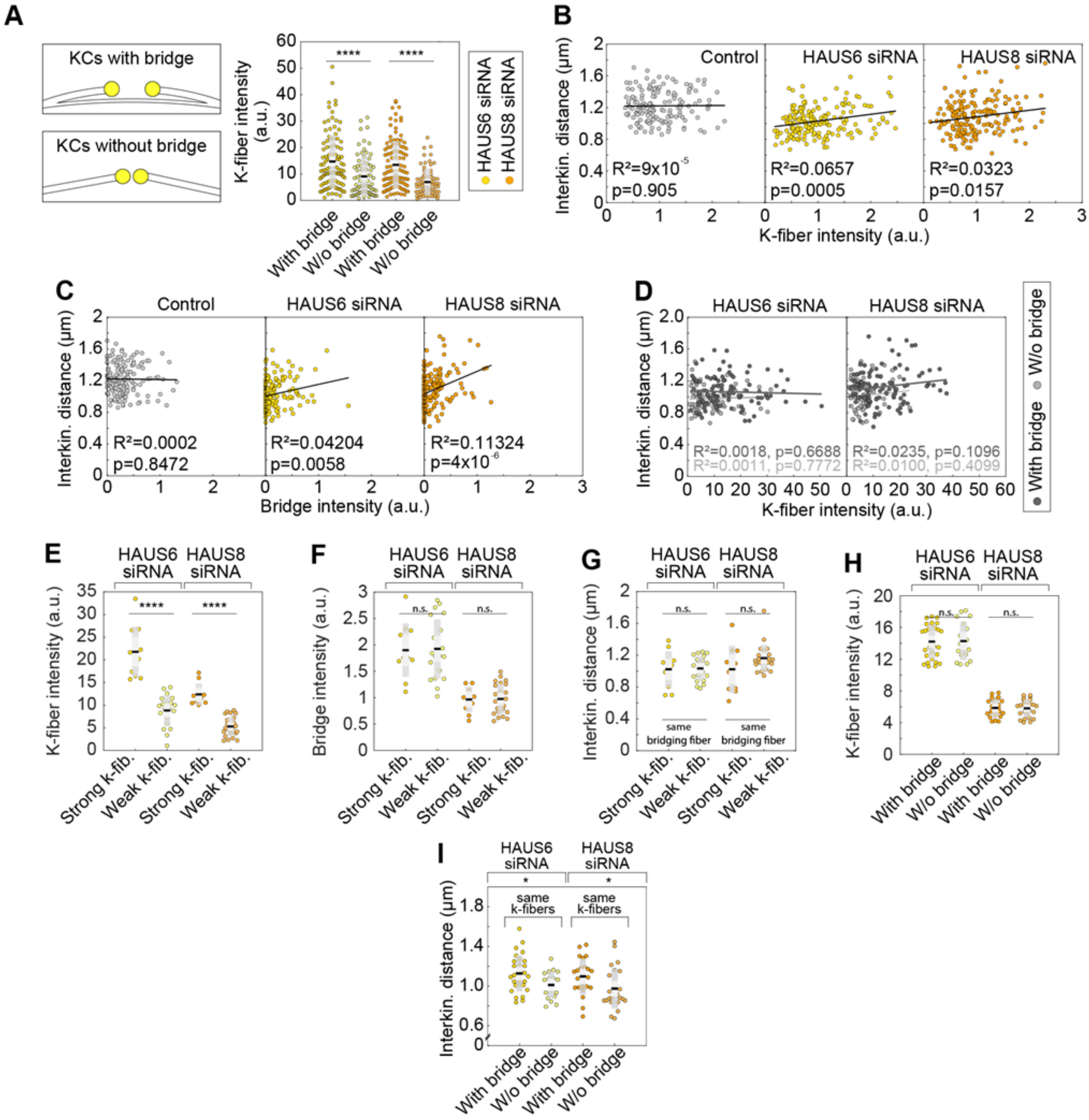

**Figure 34. The reduction of the interkinetochore distance after augmin depletion is related to the impairment of bridging fibers.** (A) Univariate scatter plots of the k-fiber intensity for kinetochore pairs with bridging fiber (dark colors) and without bridging fiber (light colors) in HAUS6- (yellow) and HAUS8-depleted (orange) RPE1 cells stably expressing CENP-A-GFP and immunostained for α-tubulin. Schematic representation of a kinetochore pair (KCs) with and without bridging fiber (See Results). N=30 HAUS6-depleted cells with 106 kinetochore pairs with bridging fibers and 74 kinetochore pairs without bridging fibers. N=30 HAUS8-depleted cells with 110 kinetochore pairs with bridging fibers and 70 kinetochore pairs without bridging fibers. (B) Correlation of the interkinetochore distance and k-fiber intensity for kinetochore pairs in control (gray), HAUS6- (yellow) and HAUS8- (orange) depleted RPE1 cells stably expressing CENP-A-GFP and immunostained for α-

**Figure 34. [continued from the previous page]** tubulin. (C) Correlation of the interkinetochore distance and bridging fiber intensity for kinetochore pairs in control (gray), HAUS6- (yellow) and HAUS8- (orange) depleted RPE1 cells stably expressing CENP-A-GFP and immunostained for α-tubulin. (B and C) N=158, 180 and 180 kinetochore pairs in 30 control, HAUS6- and HAUS8-depleted cells, respectively. For D and E, bridging and k-fiber intensities were normalized to the average intensity of two outermost k-fibers in each cell and negative intensities were set to a value zero. (D) The correlation of the interkinetochore distance and the k-fiber intensity for kinetochore pairs with (dark gray) and without (light gray) bridging fiber in HAUS6- (left) and HAUS8-depleted (right) cells. (E) Univariate scatter plots of the k-fiber intensity for kinetochore pairs with stronger k-fiber (dark colors) and with weaker k-fiber (light colors) within subgroups of kinetochore pairs with or without bridging fiber after HAUS6 (yellow) or HAUS8 (orange) depletion in RPE1 cells stably expressing CENP-A-GFP and immunostained for α-tubulin. (F) Univariate scatter plots of the bridging fiber intensity of kinetochore pairs in (E). (G) Univariate scatter plots of the interkinetochore distance for kinetochore pairs in (E). (E-G) N=11 kinetochore pairs with stronger k-fiber and 20 kinetochore pairs with weaker k-fiber in 30 HAUS6-depleted cells. N=10 kinetochore pairs with stronger k-fiber and 23 kinetochore pairs with weaker k-fiber in 30 HAUS8-depleted cells. (H) Univariate scatter plot of the k-fiber intensity for kinetochore pairs with bridging fibers (dark colors) and without bridging fibers (light colors), after HAUS6 (yellow) or HAUS8 (orange) depletion in RPE1 cells stably expressing CENP-A-GFP and immunostained for α-tubulin. K-fiber intensities are chosen to be similar within the subgroups with or without a bridging fiber to exclude the contribution of k-fibers. N=27 kinetochore pairs with a bridging fiber and 18 kinetochore pairs without a bridging fiber in HAUS6-depleted cells. N=23 kinetochore pairs with a bridging fiber and 25 kinetochore pairs without a bridging fiber in HAUS8-depleted cells. (I) Univariate scatter plot of the interkinetochore distance for HAUS6- (yellow) and HAUS8-depleted (orange) cells. Kinetochore pairs are divided into two groups: with bridging fiber (darker colors) and without bridging fiber (lighter colors), but in this case both groups have the same k-fiber intensity. N=27 kinetochore pairs with a bridging fiber and 18 kinetochore pairs without a bridging fiber in HAUS6-depleted cells, respectively; N=23 kinetochore pairs with and N=25 kinetochore pairs without a bridging fiber in HAUS8-depleted cells. (A, E-I) Boxes represent standard deviation (dark gray), 95% confidence interval of the mean (light gray) and mean value (black). All results were obtained from three independent experiments. Statistical analysis (A, E-I) t-test for samples that followed normal distribution or Mann–Whitney U test for samples that significantly departured from normality, determined

**Figure 34. [continued from the previous page]** using the Shapiro-Wilk test; (B-D) linear regression; p-value legend:<0.0001 (****), 0.0001–0.001 (***), 0.001–0.01 (**), 0.01–0.05 (*), ≥0.05 (ns).

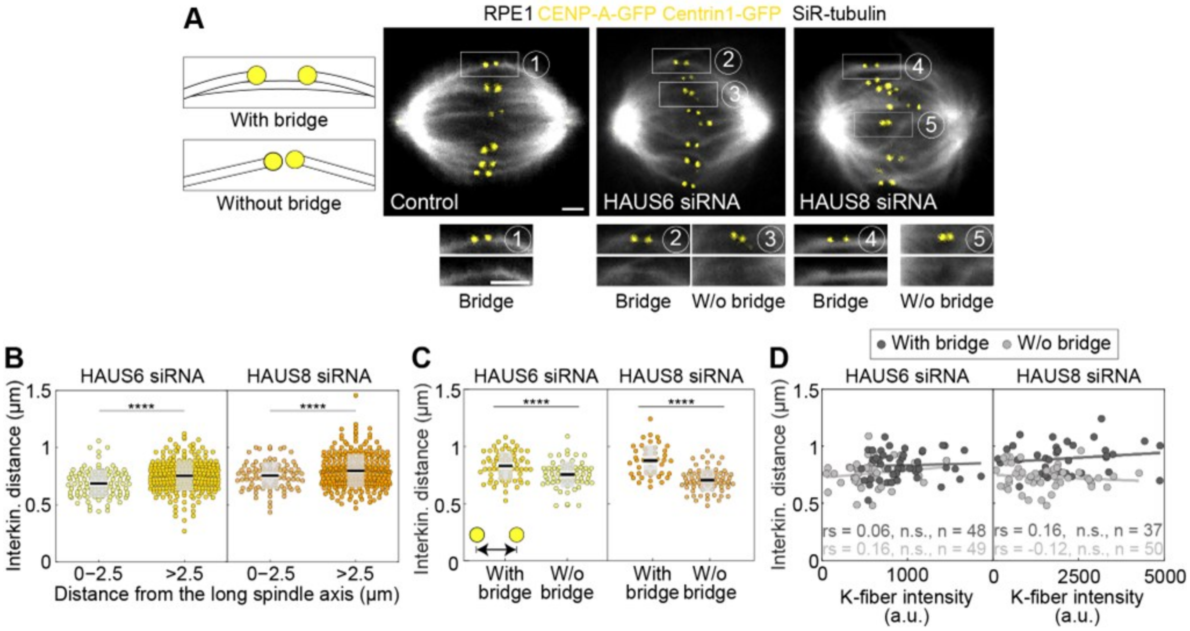

**Figure 35. The reduction of the interkinetochore distance after augmin depletion is related to the impairment of bridging fibers.** (A) Live images (single z-plane) of metaphase spindles in RPE1 cells stably expressing CENP-A-GFP and Centrin1-GFP (both in yellow) and stained with SiR-tubulin (gray). Enlarged boxes show kinetochore (KC) pairs with or without a bridging fiber. All images are adjusted for clarity (see Materials and methods). Scale bars, 2 μm. (B) Univariate scatter plot of the interkinetochore distance in HAUS6- (yellow) or HAUS8- (orange) depleted cells depending on the 3D-distance from the long spindle axis. N=10 HAUS6-depleted cells with 97 and 259 kinetochore pairs in the intervals of 0–2.5 and >2.5, respectively. N=10 HAUS8-depleted cells with 95 and 265 kinetochore pairs in the intervals of 0–2.5 and >2.5, respectively. (C) Univariate scatter plot of the interkinetochore distance in HAUS6- (yellow) and HAUS8- (orange) depleted cells. N=10 cells with >50 kinetochore pairs. Kinetochore pairs are divided into two groups: with bridging fiber (dark gray) and without bridging fiber (light gray). N=65 kinetochore pairs with and without a bridging fiber in 10 HAUS6-depleted cells; N=42 kinetochore pairs with a bridging fiber and 74 kinetochore pairs without a bridging fiber in HAUS8-depleted cells. (D) Correlation of the interkinetochore distance and k-fiber intensity for kinetochore pairs with (dark gray) and without (light gray) a bridging fiber in HAUS6 siRNA (left) and HAUS8 siRNA (right)-treated

**Figure 35. [continued from the previous page]** cells. The data represent a subset from L, in which only kinetochore pairs with k-fibers well isolated from neighboring microtubules were taken into account. The interkinetochore distance values for kinetochore pairs with and without bridging fibers were 0.83±0.02 and 0.76±0.02 μm for HAUS6 siRNA- and 0.89±0.02 and 0.73±0.01 μm for HAUS8 siRNA-treated cells, respectively, in agreement with results from panel L. rs, Spearman correlation coefficient. (K, L) Boxes represent standard deviation (dark gray), 95% confidence interval of the mean (light gray) and mean value (black). All results were obtained from three independent experiments. Statistical analysis (B and C) t-test for samples that followed normal distribution or Mann–Whitney U test for samples that significantly departured from normality, determined using the Shapiro-Wilk test; (D) linear regression; p-value legend:<0.0001 (****), 0.0001–0.001 (***), 0.001–0.01 (**), 0.01–0.05 (*), ≥0.05 (ns). Scale bars, 2 μm.

### 4.6. Actin filaments are present within the mitotic spindle during all mitotic phases

Several studies reported presence of actin within the mitotic spindle (Kita et al., 2019; Plessner et al., 2019), where only confocal microscopy was used, which was not sufficient enough to distinguish between each fine actin filament structures within the spindle. Moreover, the interplay between actin and microtubules was studied only at the beginning or at the very early stages of mitosis (Booth et al., 2019; Farina et al., 2016; Plessner et al., 2019) when microtubules only start to assemble and the space between two spindle poles is still not too crowded. However, the relationship between actin and microtubules within the assembling spindle during prometaphase and within the crowded metaphase area has not been demonstrated. To determine the precise spatial distribution of actin filaments and microtubules within the spindle throughout mitosis, I performed two-color STED imaging, which allowed me to visualise both actin and microtubules in superresolution.

I used RPE1 cells stably expressing CENP-A-GFP stained with anti-α-tubulin antibody for microtubules and SiR-actin for actin filaments and imaged them during different phases of mitosis (Figure 36A). During prophase, actin was visible as a continuous signal surrounding the nuclear area, corresponding to actin's localization to nuclear envelope demonstrated previously (Booth et al., 2019). During nuclear envelope breakdown (NEBD), the signal around the nucleus was still present, in agreement with (Booth et al., 2019), however there was an increase in actin signal inside of the nucleus visible as an actin mesh that occupied the area around the chromosomes. Although chromosomes are not imaged in this experiment, the area they occupy is visible as a black region inside the cell when actin channel is imaged. Soon after NEBD, in early prometaphase, actin mesh around chromosomes was reorganized into the filaments colocalizing with astral microtubules. Microtubules of the nascent mitotic spindle also colocalized with actin. In late prometaphase and metaphase, the colocalization shifted completely to the spindle microtubules and actin accumulated more around the spindle poles. Finally, in anaphase, actin was reorganized and became evident as a future contraction ring between the two separating masses of chromosomes, as it was demonstrated previously (Bringmann and Hyman, 2005).

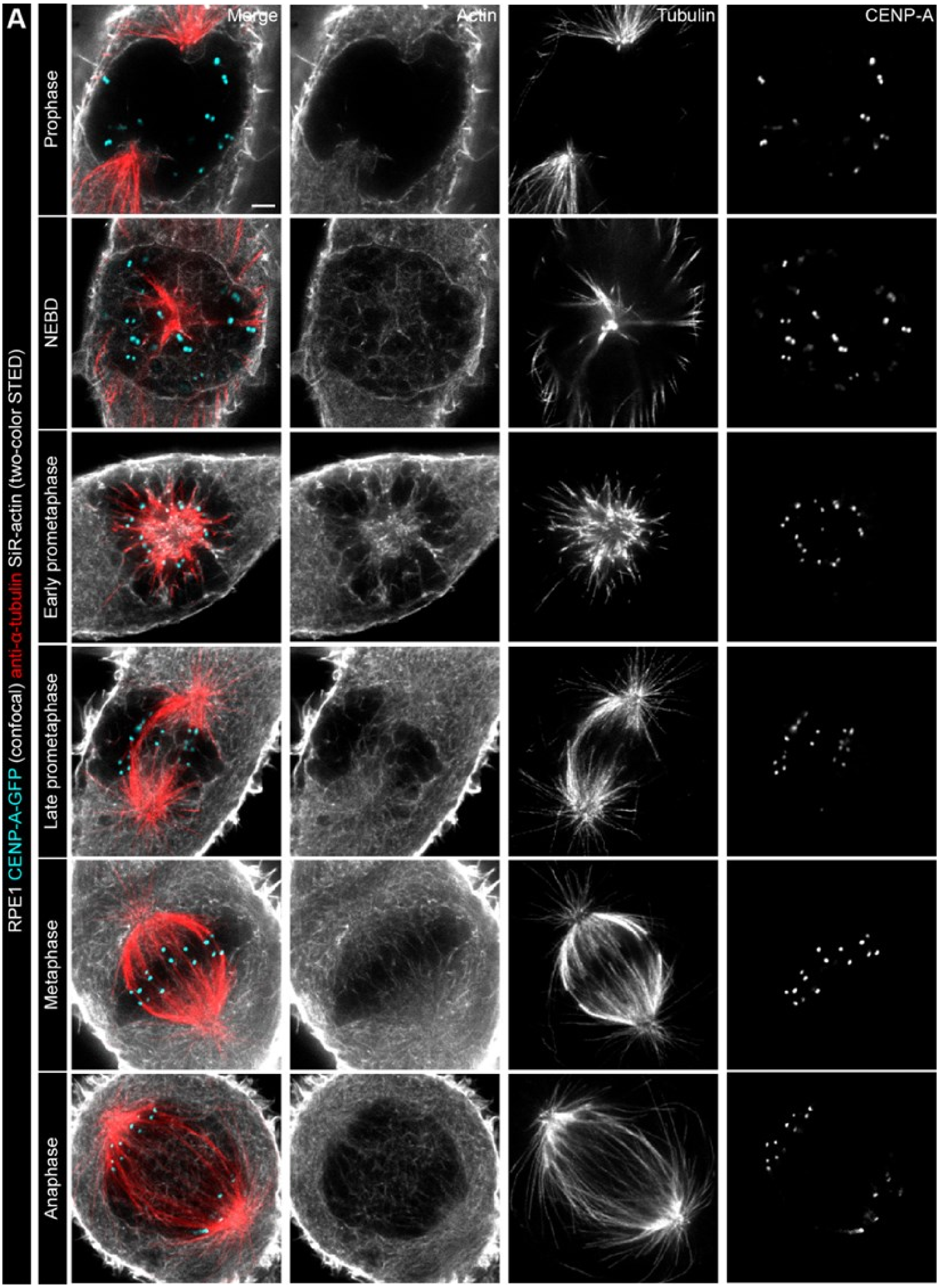

**Figure 36. Distribution of spindle actin during mitosis.** (A) Two-color STED superresolution images of actin stained with SiR-actin (gray) and microtubules immunostained for α-tubulin (red) in RPE1 cells stably expressing CENP-A-GFP (cyan, confocal). Single

**Figure 36. [continued from the previous page]** channels of actin, microtubules and kinetochores (all in gray) are shown next to the merged images. Images show single z-planes of cells undergoing mitosis, from prometaphase until anaphase. All images are adjusted for clarity based on the intensity of actin filaments in each image (see Materials and methods). Scale bar, 2 µm.

To make sure that staining and imaging protocols did not produce any actin artefacts, I performed a series of experiments to exclude that. To check for fluorophore bleed-through, I performed single channel staining of either tubulin or actin and imaged both channels with the same settings as I would use in two-color STED in Figure 36A. The selected fluorophores did not cause any leakage in neighbouring channels (Figure 37A). Next, to exclude possible dye artefacts, I applied phalloidin 488, another commonly used F-actin binding dye. I stained unlabelled RPE1 cells with anti-α-tubulin antibody for microtubules and phalloidin 488 for spindle actin (Figure 37B). Actin within the spindle colocalized with astral and spindle microtubules during early prometaphase and metaphase, respectively, consistent with the SiR-actin staining shown in Figure 36. Finally, to directly compare structures labelled with phalloidin and SiR-actin, I stained RPE1 cells with phalloidin 488 and SiR-actin and imaged them on confocal microscope with the Airyscan detector (Huff, 2015) to achieve better resolution in both actin channels (Figure 37C). Phalloidin 488 and SiR-actin channel overlapped completely suggesting that both dyes label the same structures. The imaging with Airyscan detector, as an independent microscopy method, also demonstrated that the spindle actin signals correspond to those acquired by STED microscopy in Figure 36, finally showing that the chosen fluorophores, staining and imaging protocols do not produce any artefacts and can be used for further experiments.

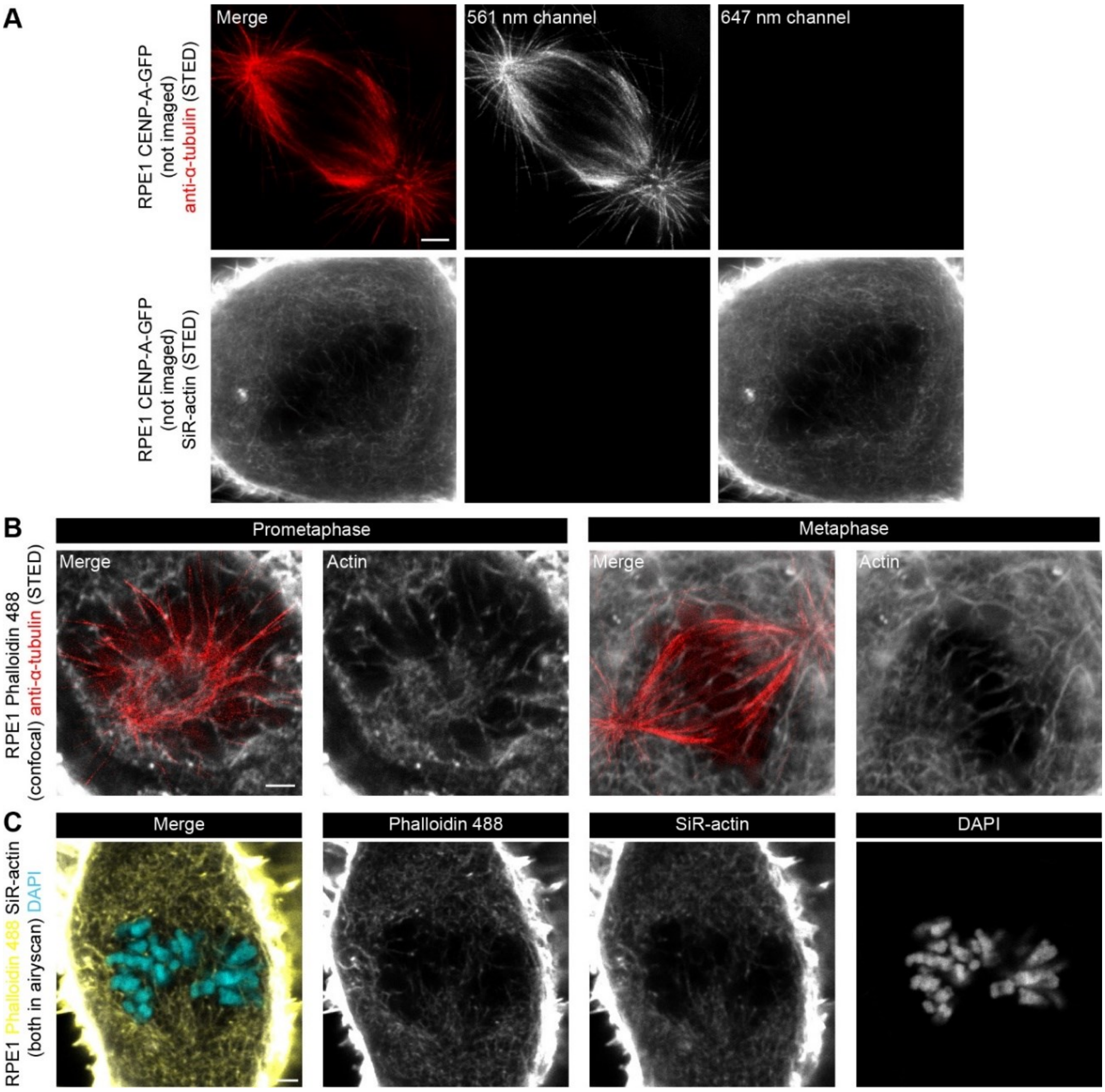

**Figure 37. Different approaches to exclude immunostaining and imaging artefacts**. (A) STED superresolution images of single channel staining (either microtubules immunostained for α-tubulin (red) or actin stained with SiR-actin (gray)) in RPE1 cells stably expressing CENP-A-GFP (not shown), to check for fluorophore bleed-through. Single channels of actin and microtubules (all in gray) are shown next to the merged images. Images show single z-planes of metaphase cells. (B) STED superresolution images of microtubules immunostained for α-tubulin (red) and actin stained with phalloidin 488 (gray, confocal) in unlabelled RPE1 cell. Images show single z-planes of prometaphase and metaphase cells. (C) Unlabelled RPE1 cells stained with phalloidin 488 (yellow, airyscan) and SiR-actin (gray, airyscan) for actin and DAPI (blue) for chromosomes. Single channels of actin and chromosomes (all in gray) are shown next to the merged image. Images show single z-planes. All images are adjusted for clarity based on the intensity of actin filaments in each image (see Materials and methods). Scale bar, 2 μm.

## 4.7. Actin follows the similar distribution pattern as microtubules during mitosis

Since I demonstrated that actin is present within the mitotic spindle throughout mitosis but changes its organization from mesh to filaments, I wanted to get a better insight if actin distribution overlaps with microtubule distribution within the mitotic spindle from early prometaphase until metaphase. I analysed the intensity profiles of actin and microtubules throughout the spindle midzone and across the pole-to-pole axis in RPE1 cells (Figure 38A-B). I divided early prometaphase spindles into two groups: shorter spindles with chromosome ring (Magidson et al., 2011) (Figure 36A – early prometaphase) and longer spindles (distinguished by two discernible spindle poles, Figure 38A – early prometaphase, see Materials and methods). To get the actin distribution throughout the spindle midplane and across the pole-to-pole axis, the intensity profiles were drawn only on the latter group of the early prometaphase spindles.

To analyse how distribution of actin and microtubule signal changes within the spindle midplane, I measured and analysed their intensity profiles in the central part of the spindle, between the two spindle poles (Figure 38A). In early prometaphase, spindle actin filaments and microtubule bundles were still not fully formed throughout the spindle midzone (microtubule signals in agreement with (Matković et al., 2022)). This was visible as two wide signal intensity peaks that overlapped at the edges of spindle midzone profiles. During late prometaphase and metaphase, actin filaments and microtubule bundles were more prominent, occupying the whole metaphase plate area and their signal intensity peaks overlapped across the entire profile. These results suggest an interplay between actin filaments and microtubule bundles in the central part of the spindle, from the early prometaphase as they start to form until the metaphase where they contribute to proper spindle architecture.

Next, I analysed the distribution of actin and microtubules across the pole-to-pole axis (Figure 38B). In early prometaphase, actin signal was continuously present between the two spindle poles, while microtubule signal had a decrease in the equatorial region. In late prometaphase and metaphase, actin and microtubule signal were overlapping between the two spindle poles, with both having the decrease in signal at te equatorial region where actin filaments and microtubule bundles are less dense and attach to or occupy the area around chromosomes. Both actin and microtubules colocalized in the polar region. These results show that actin follows the similar pattern as microtubules suggesting that its distribution is similar to microtubule distribution during mitosis.

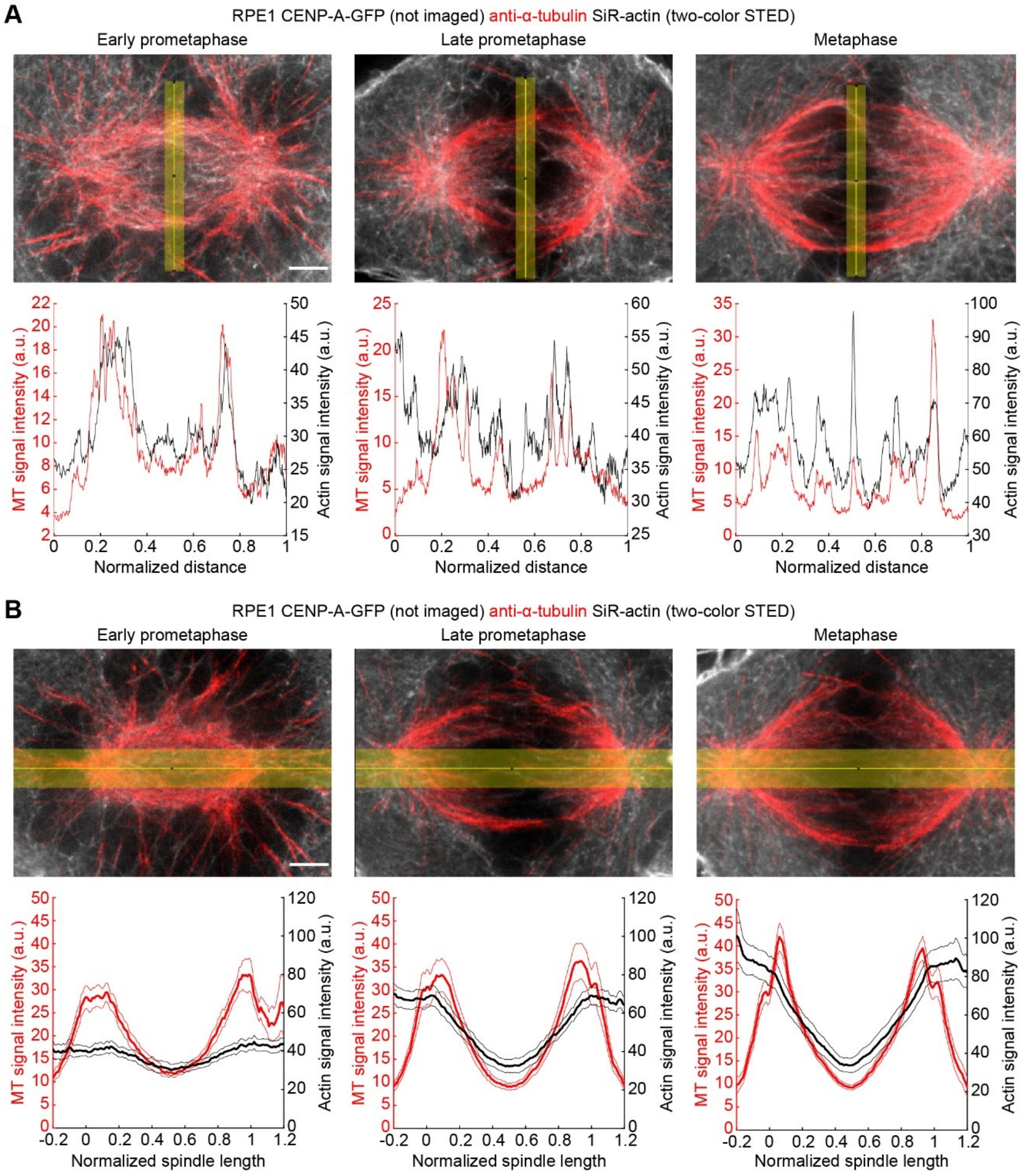

**Figure 38. Actin follows similar distribution pattern as microtubules during mitosis.** (A) and (B) Two-color STED superresolution images of actin stained with SiR-actin (gray) and microtubules immunostained for α-tubulin (red) in RPE1 cells stably expressing CENP-A-GFP (not shown). Images show single z-planes of early prometaphase, late prometaphase and metaphase spindles. Yellow line represents area where intensity profiles of actin and microtubules was measured. Corresponding intensity profile graphs are shown below each image. Intensity profile graphs measured throughout the metaphase plate area show one representative example of each phase. Intensity profile graphs between the two spindle poles

**Figure 38. [continued from the previous page]** are average of 10 cells in early prometaphase, 17 cells in late prometaphase and 21 cells in metaphase. Spindle poles are normalized. Values are show and mean (dark line) and SEM (shaded areas). All results were obtained from three independent experiments. Scale bars, 2 μm.

## 4.8. Actin colocalization shifts from astral microtubules in early prometaphase to spindle microtubules in late prometaphase and metaphase

Since two-color STED microscopy enabled me to distinguish between the actin filaments and microtubule bundles within the spindle, I decided to make a detailed analysis of their spatial distribution throughout mitosis. STED images in Figure 36 and signal intensity analysis in Figure 38 suggest that actin colocalization shifts from astral microtubules towards the spindle microtubules during mitosis. To analyse that, I first measured the signal intensity profiles of actin and microtubules in RPE1 early prometaphase spindles with chromosome ring (Figure 39A). The majority of actin signal peaks overlapped with microtubule signal peaks, suggesting an interplay between astral microtubules and actin during early prometaphase. To determine the percentage of astral microtubules that colocalize with actin, I quantified the number of astral microtubules that had actin filaments present on them (see Materials and methods). During early prometaphase, actin filaments overlapped with astral microtubules in 84.6 ± 3.3% of cases (Figure 39B). In comparison, during late prometaphase and metaphase, that was the case only for 7.3 ± 2.1% and 5.2 ± 2.1% of astral microtubules, respectively (Figure 39B). These results suggest that after NEBD, actin filaments that occupied the space around the chromosomes (Figure 36) reorganize into filaments that colocalize with astral microtubules of nascent spindle.

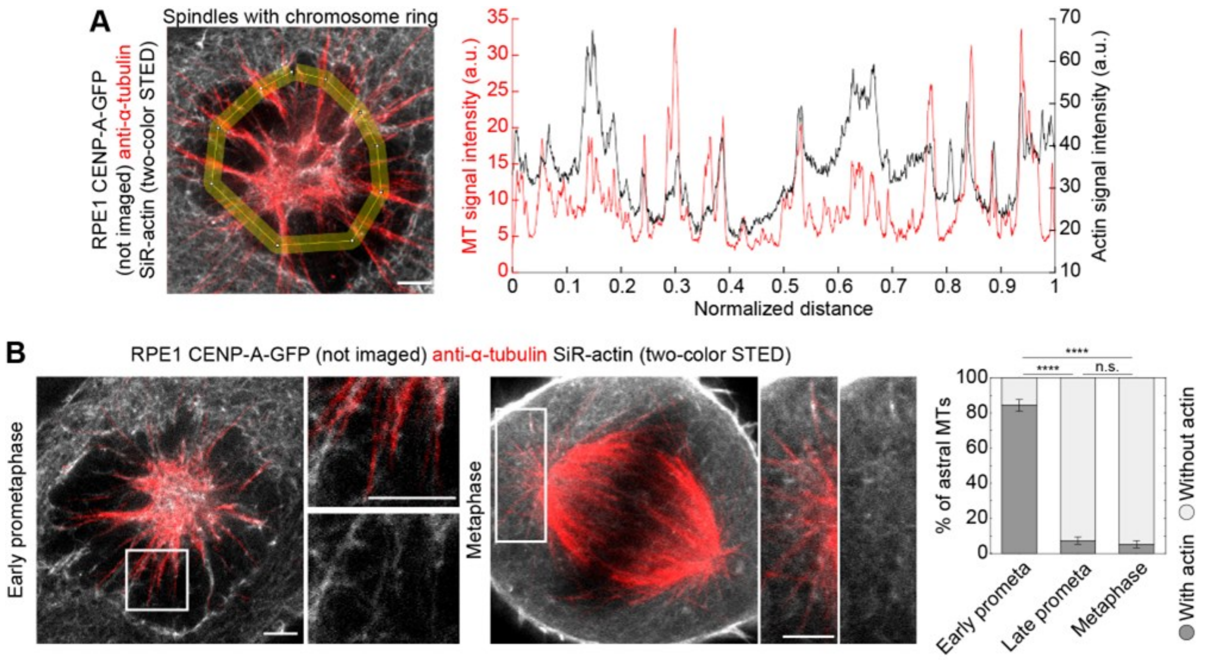

**Figure 39. Actin colocalizes with astral microtubules only during early prometaphase.** (A) Two-color STED superresolution image of actin stained with SiR-actin (gray) and microtubules immunostained for α-tubulin (red) in RPE1 cells stably expressing CENP-A-GFP (not shown). Image shows single z-planes of early prometaphase spindle. Yellow line represents area where intensity profile of actin and microtubules was measured. Corresponding intensity profile graph is shown next to the image. (B) Two-color STED superresolution image of actin and microtubules as described in (A). Enlarged areas, depicted with white square, of astral microtubules are shown next to the images. Percentage of astral microtubules colocalizing with actin (dark gray) and not colocalizing with actin (light gray) in early prometaphase (123 astral microtubules, 104 colocalizing and 19 not colocalizing with actin), late prometaphase (150 astral microtubules, 11 colocalizing and 139 not colocalizing with actin) and metaphase (115 astral microtubules, 6 colocalizing and 109 not colocalizing with actin). Statistical analysis: proportion Z test; p-value legend:<0.0001 (****), 0.0001–0.001 (***), 0.001–0.01 (**), 0.01–0.05 (*), ≥0.05 (ns). Scale bars, 2 µm.

Since actin colocalization with astral microtubules was lost during late prometaphase and metaphase, I set to determine the spatial distribution of actin with spindle microtubules in those phases (Figure 40A). Firstly, I determined the percentage of spindle microtubules that colocalized with actin filaments and vice versa. The 83.2 ± 3.5% and 78.9 ± 3.9% of actin filaments colocalized with microtubule bundles in late prometaphase and metaphase, respectively (Figure 40B). The result was consistent in opposite situation, where 80.0 ± 3.4% and 86.13 ± 2.9% of microtubule bundles colocalized with actin filaments in late prometaphase and metaphase, respectively (Figure 40C). These results suggest that actin filaments constitute a substantial part of the spindle architecture.

Next, I divided microtubule bundles that colocalized with actin onto three groups based on the actin appearance: microtubule bundles that directly colocalized with actin filaments, microtubule bundles with actin filament adjacent to them and microtubule bundles with actin mesh around or on them (Figure 40A). Actin directly colocalized in 24% and 46% of microtubule bundles and was adjacent to 40% and 26% of microtubules in late prometaphase and metaphase, respectively (Figure 40D). In both late prometaphase and metaphase, actin mesh was present in approximately 40% of microtubule bundles (Figure 40D). I further quantified the presence of actin in kinetochore and bridging fibers (Figure 40E). Actin was present in 70.9 ± 3.9% and 62.7 ± 5.9% kinetochore and bridging fibers, respectively. In conclusion, during early prometaphase, actin colocalizes with astral microtubules that are most likely soon going to be part of the spindle microtubules, while in later phases this colocalization is shifted towards the spindle microtubules between the two poles.

Lastly, I determined the percentage of kinetochores that are attached to or in close proximity to actin filaments during early prometaphase and metaphase (Figure 40F, see Materials and methods). The result was similar for both phases, with 87.7 ± 1.9% and 93.0 ± 2.0% kinetochores being attached to actin in early prometaphase and metaphase, respectively (Figure 40G). I measured intensity profiles of actin, microtubules and kinetochores to determine the distribution of actin with respect to kinetochore pairs and kinetochore and bridging fiber in metaphase (Figure 40H). Microtubules showed the decrease at the position of bridging microtubules, between the two kinetochores, and actin signal followed the same distribution. Taken together, kinetochores are adjacent to actin filaments since early prometaphase and remain colocalized to them until metaphase.

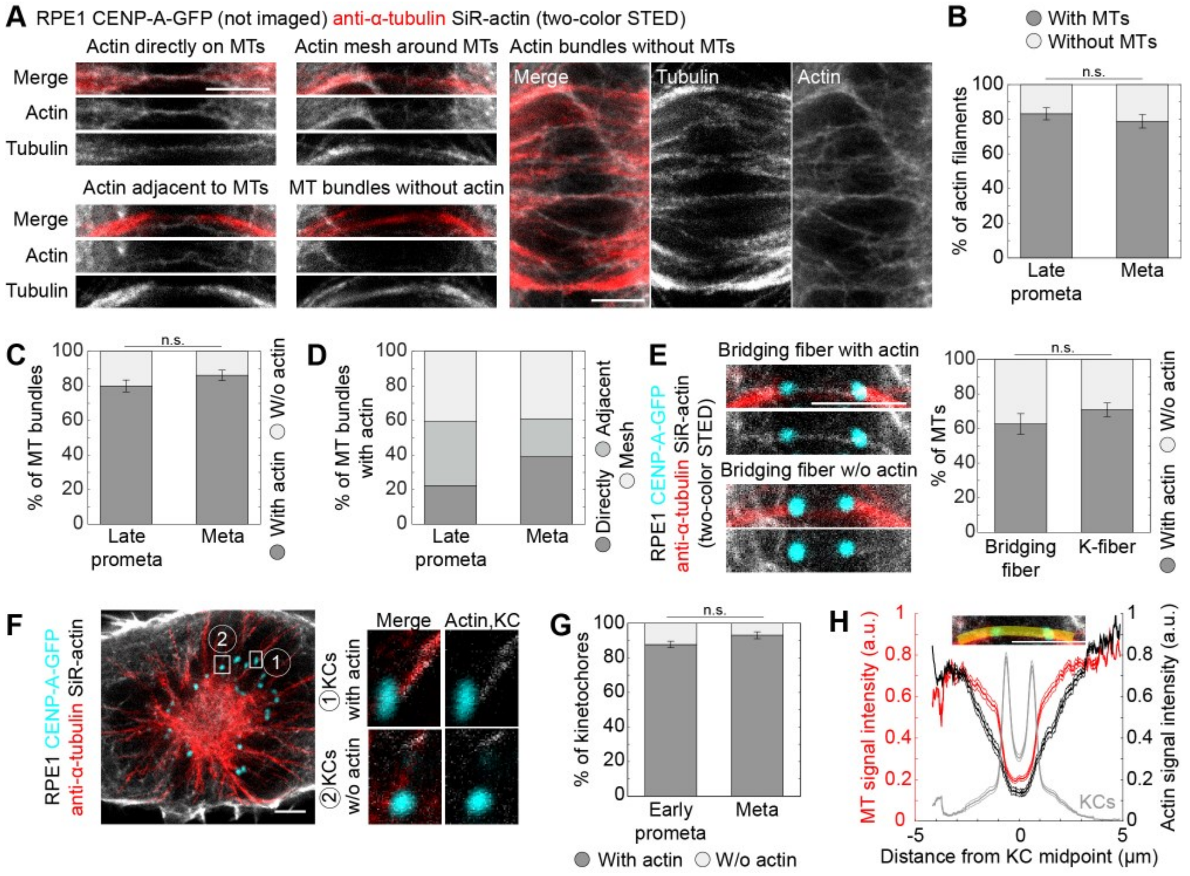

**Figure 40. Actin colocalizes with spindle microtubules during late prometaphase and metaphase.** (A) Two-color STED insets of different types of actin and microtubule colocalization denoted above every image in RPE1 cells stably expressing CENP-A-GFP (not imaged) stained with SiR-actin for actin (gray) and immunostained for α-tubulin for microtubules (red). Image shows single z-planes. (B) Percentage of actin filaments that do (dark gray) or do not (light gray) colocalize with microtubules in late prometaphase (113 actin filaments, 94 colocalizing and 19 not colocalizing with microtubules) and metaphase (109 actin filaments, 86 colocalizing and 23 not colocalizing with microtubules). (C) Percentage of microtubule bundles that do (dark gray) or do not (light gray) colocalize with actin filaments in late prometaphase (135 microtubule bundles, 108 colocalizing and 27 not colocalizing with actin) and metaphase (137 microtubule bundles, 118 colocalizing and 19 not colocalizing with actin). (D) Percentage of microtubule bundles that colocalize with actin filaments in late prometaphase and metaphase divided based on colocalization type (directly (dark gray), adjacent (gray) or actin mesh (light gray)). (E) Two-color STED insets of bridging fibers that colocalize or do not colocalize with actin filaments in RPE1 cells stably expressing CENP-A-GFP (cyan, confocal) stained with SiR-actin for actin (gray) and immunostained for α-tubulin for microtubules (red). Image shows single z-planes. The graphs show percentage of bridging

**Figure 40. [continued from the previous page]** or kinetochore fibers that do (dark gray) or do not (light gray) colocalize with actin filaments. N = 67 bridging fibers (42 colocalizing and 25 not colocalizing with actin); N = 134 (95 colocalizing and 39 not colocalizing with actin). (F) Two-color STED image of early prometaphase RPE1 cell stably expressing CENP-A-GFP (cyan, confocal) stained with SiR-actin for actin (gray) and immunostained for α-tubulin for microtubules (red). Image shows single z-planes. Insets of kinetochores with and without actin filaments are shown on the right and correspond to the squared region on the whole image of the spindle. (G) Percentage of kinetochores with (dark gray) or without (light gray) actin filaments in early prometaphase (300 kinetochores, 236 with and 37 without actin) and metaphase (158 kinetochores, 147 with and 11 without actin). (H) Average intensity profile graph of kinetochores, actin and microtubules for kinetochore pairs found in metaphase (N = 62 pairs). Inset represents method for measuring intensity profiles. All results are obtained from three independent experiments. Statistical analysis (B, C, E, G) proportion Z test; p-value legend:<0.0001 (****), 0.0001–0.001 (***), 0.001–0.01 (**), 0.01–0.05 (*), ≥0.05 (ns). Scale bars, 2 µm.

## 4.9. Inhibition of actin branching and polymerization has mild to no effect on spindle assembly and chromosome segregation

It was previously reported that inhibition of actin polymerization and branching has a role in spindle positioning and orientation (Kunda and Baum, 2009), as well in mitotic progression and fidelity (Plessner et al., 2019). Since my results demonstrate that spindle microtubules and actin colocalize from early prometaphase until anaphase, I hypothesize that actin is involved in proper spindle assembly that ensures normal chromosome congression and segregation. To investigate that, I inhibited actin branching by Arp2/3 inhibitor CK666 and actin polymerization by latrunculin A in RPE1 cells stably expressing CENP-A-GFP and Centrin1-GFP (Figure 41A). I performed live-cell imaging of cells in 1.3 mm wide field of view with high spatiotemporal resolution (~350 nm pixel size and 1 min/image) for up to 18 hours using lattice light-sheet microscopy.

First, to determine if the DMSO used to prepare all actin inhibitors in this thesis has any toxic effects on cells, I treated RPE1 cells with the highest used DMSO concentration (0.2% v/v final concentration in the cell media). I performed live-cell imaging using lattice light-sheet microscopy (Figure 41A) and measured mitotic timing, spindle length in metaphase, the percentage of bipolar cells, and the percentage of cells exhibiting segregation errors (Figure 41B-E, see Materials and Methods), which are all a readout of normal mitotic progression. Since there were no significant differences in these parameters compared to untreated cells, I used untreated cells as a control in further experiments.

To determine the role of spindle actin in mitotic progression, I measured mitotic timing and spindle length just before anaphase onset as a readout of chromosome congression behaviour and spindle architecture, respectively. The timing from NEBD until anaphase onset increased mildly, but significantly, when actin branching was inhibited compared to untreated cells (Figure 41B, untreated cells entered anaphase after 24.7 ± 0.8 min, and cells treated with CK666 after 29.6 ± 0.8 min). Inhibition of actin polymerization by Latrunculin A showed no effect on mitotic timing (26.7 ± 1.0 min, Figure 40B). Spindle architecture was not significantly impaired upon treatments with actin inhibitors compared to untreated cells, evident as no change in spindle length (control 14.1 ± 0.3 µm, CK666 13.7 ± 0.2 µm, Latrunculin A 14.5 ± 0.2 µm, Figure 40C). Since actin was also present at spindle poles during mitosis (Figure 36 and 38B), I next analysed percentage of bipolar spindles in untreated and cells treated with actin inhibitors. There was no significant difference between untreated and treated cells (Figure 40D). Finally, to analyse the role of actin in chromosome segregation, I analysed if cells have lagging kinetochores or other errors during anaphase (see Materials and methods). All cells divided with no errors in untreated, CK666- and Latrunculin A-treated cells (Figure 40E), contrary to previous findings (Plessner et al., 2019). Taken together, inhibition of actin branching and polymerization has mild to none effects on spindle assembly and mitotic timing.

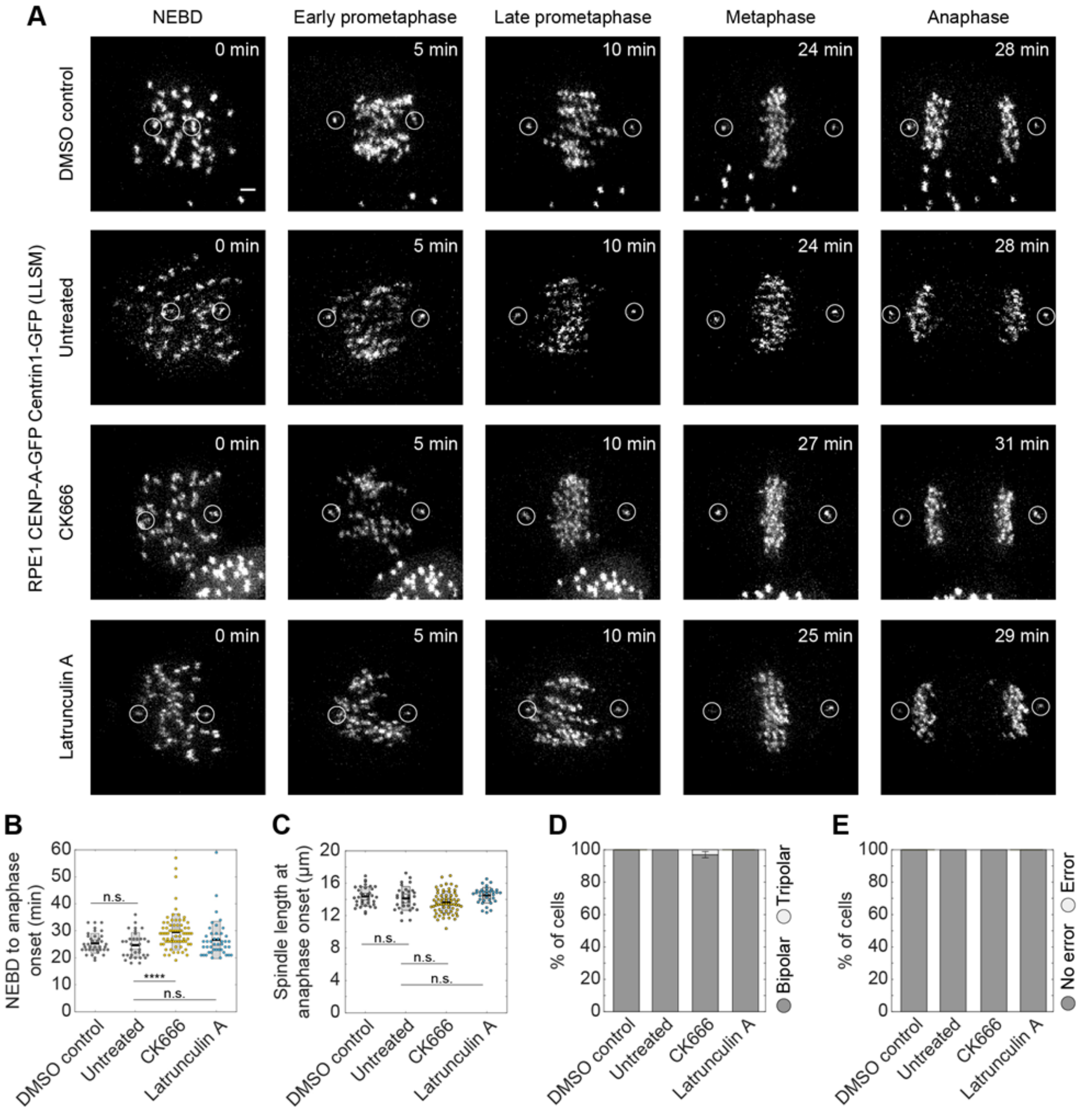

**Figure 41. Inhibition of actin branching and polymerization does not affect spindle assembly and chromosome segregation.** (A) Time-lapse images of RPE1 cells stably expressing CENP-A-GFP and Centrin1-GFP (both in gray, lattice light-sheet) in untreated and cells treated with DMSO, CK666 and latrunculin A throughout mitosis. Images show maximum intensity projections of the whole cell. Centrosomes are denoted with white circles. (B) Univariate scatter plot of the mitotic timing determined as time from NEBD to anaphase onset for DMSO (gray, N = 37), untreated (gray, N = 33), CK666- (yellow, N = 73) and latrunculin A- (blue, N = 44) treated cells. (C) Univariate scatter plot of spindle length at anaphase onset for DMSO (gray, N = 34), untreated (gray, N = 30), CK666- (yellow, N = 68) and latrunculin A- (blue, N = 44) treated cells. (D) Percentage of cells with bipolar (dark gray) and tripolar (light gray) spindles in DSMO (N = 37), untreated (N = 33), CK666- (N = 73) and latrunculin

**Figure 41. [continued from the previous page]** A- (N = 42) treated cells. (E) Percentage of cells that segregated without errors (dark gray) and with errors (light gray) in DMSO (N = 37), untreated (N = 33), CK666- (N = 73) and latrunculin A- (N = 44) treated cells. (B-C) Boxes represent standard deviation (dark gray), 95% confidence interval of the mean (light gray) and mean value (black). All results were obtained from three independent experiments, except for DMSO-treated cells where one independent experiment was performed. Statistical analysis (B and C) Kruskal-Wallis test with post-hoc Dunn's test; p-value legend:<0.0001 (****), 0.0001–0.001 (***), 0.001–0.01 (**), 0.01–0.05 (*), ≥0.05 (ns). Scale bars, 2 µm.

### 4.10. Actin stabilization induces abnormal pole movement during mitosis

The effects of actin stabilization on cell morphology and chromosome movements during anaphase have been previously reported (Bubb et al., 2000; Ou et al., 2002; Xie and Forer, 2008). However, how inhibition of actin depolymerization affects spindle assembly, spindle pole structure and chromosome segregation has not been demonstrated. Actin stabilizing drug jasplakinolide causes polymerization of monomeric actin into aggregates (Bubb et al., 2000), resulting in disordered actin polymers within the cell. To investigate if actin stabilization has also an impact on spindle architecture and mitotic fidelity, I treated RPE1 cells stably expressing Centrin-GFP H2B-eGFP mCherry-tubulin with jasplakinolide and performed live-cell imaging on lattice light-sheet microscope (Figure 42A).

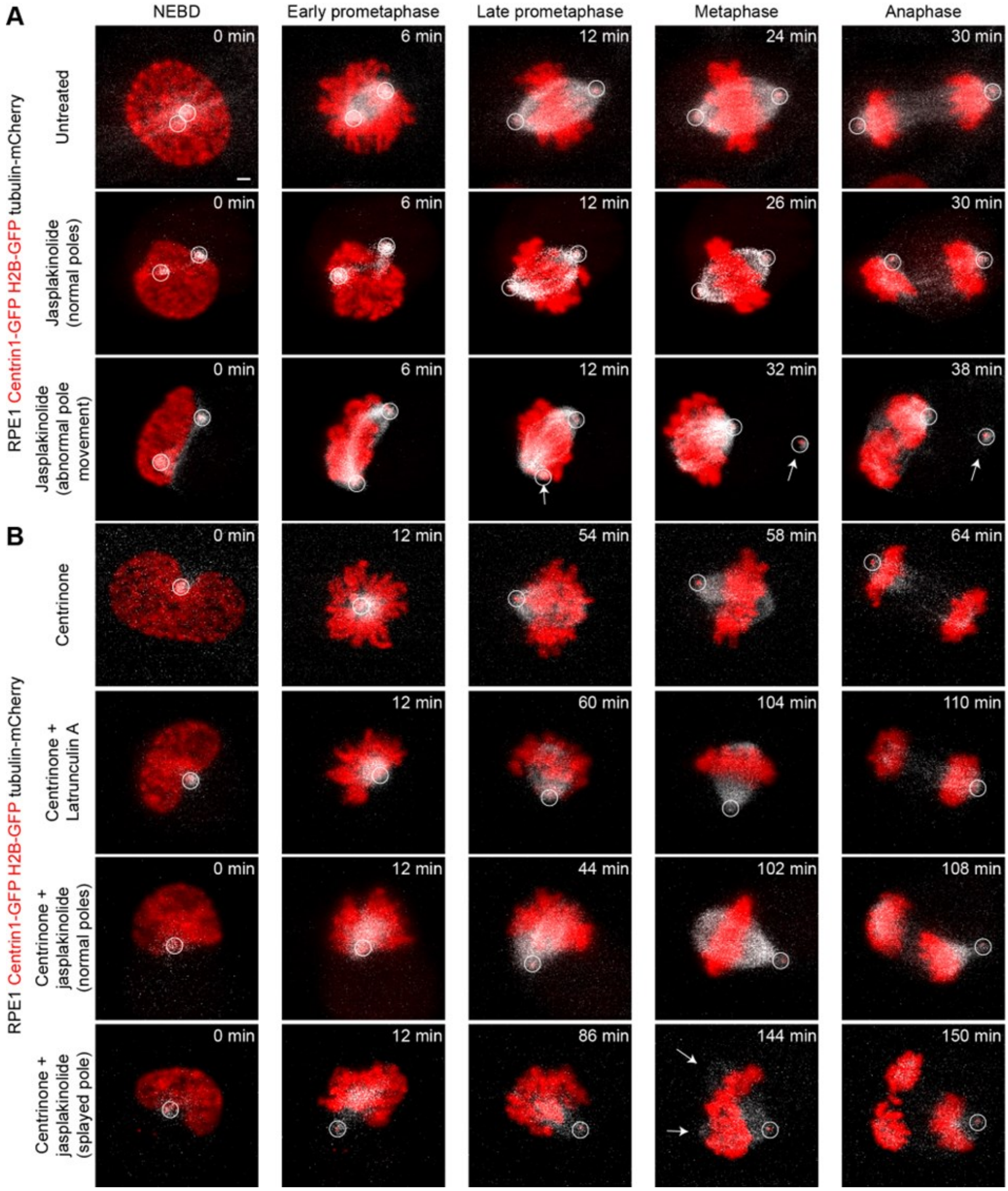

**Figure 42. Actin is involved in normal spindle pole morphology and focusing.** (A) and (B) Time-lapse images of RPE1 cells stably expressing Centrin-GFP H2B-eGFP (both in red) and mCherry-tubulin (gray, lattice light-sheet) throughout mitosis in untreated cells or cells treated with various inhibitors denoted next to each time-lapse. Images show maximum intensity projections of the whole cell. Centrosomes are denoted with white circles. Abnormal pole movements and pole splaying are denoted with white arrows. Scale bars, 2 µm.

The timing from NEBD to anaphase, a readout of spindle assembly and chromosome congression timing, was significantly higher compared to untreated cells (Figure 43A, 24.2 ± 0.6 min for control cells and 38.6 ± 2.7 min for jasplakinolide-treated cells). This suggests that actin stabilization affects prometaphase and metaphase during mitosis. Next, I determined the spindle length in metaphase as a measure of spindle architecture. The actin stabilization did not affect the spindle architecture during metaphase, since untreated and jasplakinolide-treated cells had similar spindle lengths (Figure 43B, 12.4 ± 0.1 µm for controls and 12.4 ± 0.2 µm for jasplakinolide treatment).

Surprisingly, I noticed that 33.3 ± 6.4% of cells exhibit abnormal pole movement seen as a rapid movement of centrin signal away from the spindle pole and moving through the cytoplasm during mitosis (Figure 42A – compare cell treated with jasplakinolide with normal poles and abnormal pole, and Figure 43C). Although treatment with jasplakinolide prolonged mitotic duration (Figure 43A), longer time to anaphase did not correlate with abnormal pole movement (Figure 43D). Interestingly, described rapid movement mostly happened during prometaphase (in 17 out of 18 cases when spindle pole exhibited abnormal movement). Additionally, 11.2 ± 4.5% of cells had splayed pole structure at the anaphase onset (Figure 43E), contributing to significantly higher segregation error rate compared to untreated cells since those were multipolar cell divisions (Figure 43F). Taken together, actin stabilization by jasplakinolide results in abnormal pole movements during mitosis.

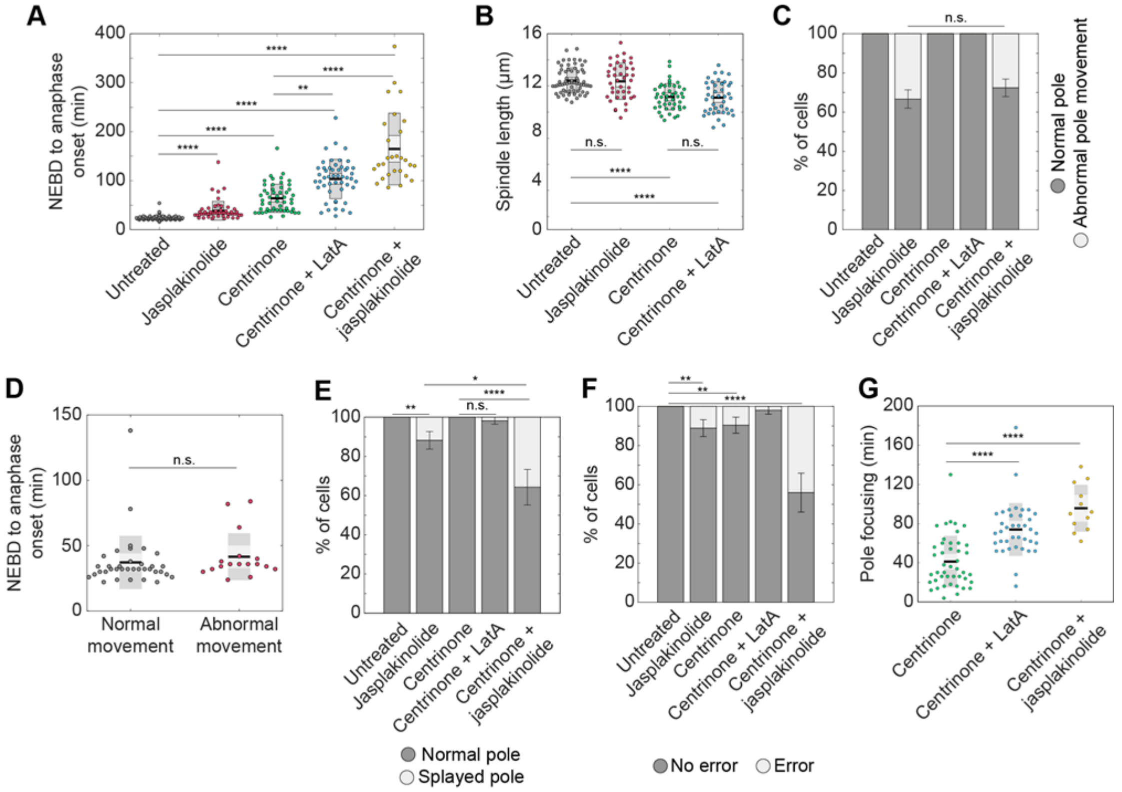

**Figure 43. Spindle actin promotes spindle pole focusing and bipolar mitosis.** (A) Univariate scatter plot of the mitotic timing determined as time from NEBD to anaphase onset for untreated (gray, N = 67), jasplakinolide- (red, N = 53), centrinone- (green, N = 52), centrinone and latrunculin A- (blue, N = 50) and centrinone and jasplakinolide- (yellow, N = 28) treated RPE1 cells stably expressing Centrin-GFP H2B-eGFP and mCherry-tubulin. (B) Univariate scatter plot of the spindle length determined one frame before anaphase onset for untreated (gray, N = 65), jasplakinolide- (red, N = 41), centrinone- (green, N = 45) and centrinone and latrunculin A- (blue, N = 41) treated cells. Cells treated with centrinone and jasplakinolide were diagonally dividing with respect to the imaging plane so measurements in maximum z-projections were not accurate. (C) Percentage of cells with normal pole movements (dark gray) and abnormal pole movements (light gray) during mitosis for the same treatments as in (A). Number of analysed cells: 67 untreated, 54 jasplakinolide-, 54 centrinone, 50 centrinone and latrunculin A- and 29 centrinone and jasplakinolide-treated cells. (D) Univariate scatter plot of mitotic timing for jasplakinolide treated cells divided onto those having normal pole movements (gray, N = 36) and abnormal pole movements (red, N = 17) during mitosis. (E) Percentage of cells where spindles have normal pole structure (dark gray) and when the pole is splayed (light gray) upon entering anaphase for the same treatments as in (A). Number of analysed cells: 67 untreated, 51 jasplakinolide-, 60 centrinone-, 56 centrinone and latrunculin A- and 28 centrinone and jasplakinolide-treated cells. (F) Percentage of cells that divided

**Figure 43. [continued from the previous page]** without errors (dark gray) and with errors (light gray) for the same treatments as in (A). Note that when cells entered the anaphase with splayed poles, they were defined as those segregating with errors (see Materials and methods). Number of analysed cells: 67 untreated, 54 jasplakinolide-, 52 centrinone-, 50 centrinone and latrunculin A- and 25 centrinone and jasplakinolide-treated cells. (G) Univariate scatter plot of time to focus poles without centriole in centrinone- (green, N = 44), centrinone and latrunculin A- (blue, N = 38) and centrinone and jasplakinolide- (yellow, N = 12) treated cells. (A, B, D, G) Boxes represent standard deviation (dark gray), 95% confidence interval of the mean (light gray) and mean value (black). Number of independent experiments: 2 for control, jasplakinolide and centrinone and jasplakinolide treatments, 3 for centrinone treatment and 1 for centrinone and latrunculin A treatment. Statistical analysis (A, B and G) Kruskal-Wallis test with post-hoc Dunn's test, (C, E, F) proportion Z test, (D) Mann–Whitney U test; p-value legend:<0.0001 (****), 0.0001–0.001 (***), 0.001–0.01 (**), 0.01–0.05 (*), ≥0.05 (ns).

### 4.11. Actin promotes spindle pole focusing when centrioles are absent

To further explore if actin has a role in maintaining spindle pole structure, I decided to perturb centrosomes in RPE1 cells stably expressing Centrin-GFP H2B-eGFP tubulin-mCherry and perform live-cell imaging on lattice light-sheet microscope. To achieve that, I inhibited centriole duplication by Plk4 inhibitor centrinone (Wong et al., 2015) and subsequently added latrunculin A or jasplakinolide to inhibit actin polymerization and depolymerization, respectively (Figure 42B). Centrinone treatment results in spindles that have one or zero centrioles at each spindle pole (Wong et al., 2015) (see Materials and methods). Cells treated only with centrinone focus poles normally, although the pole structure is impaired. I hypothesised that if spindle actin is involved in spindle pole maintenance, cells treated with centrinone and actin inhibitors will have impaired pole movements and/or structure on the pole with zero centrioles. To test that, I analysed pole movements as in Figure 43 and additionally measured the timing needed to focus poles without centrioles, as well as mitotic duration and segregation efficiency.

Cells treated only with centrinone took longer to anaphase onset compared to untreated cells, but were error free (Figure 43A and Figure 43F). Combined treatments with centrinone and actin inhibitors prolonged mitotic duration (Figure 43A), so I analysed what part of mitosis took longer compared to centrinone treatment alone. I analysed time from NEBD until the pole that had zero centrioles was focused. This timing was significantly higher compared to centrinone, contributing to longer mitotic duration and suggesting that actin is involved in this step (Figure 43G). Cells treated with jasplakinolide and centrinone in 35.7 ± 9.0% of cases exhibited pole splaying on pole without centrioles compared to centrinone alone (Figure 43E). Pole with centrioles was displaced similarly as in jasplakinolide treatment alone, with 27.6 ± 4.5% of cells exhibiting it (Figure 43C). Note that in analysis where pole focusing was measured, I only analysed cells that did not exhibit pole splaying, so pole focusing timing is underestimated because some cells never focused both poles. These results suggest that spindle actin promotes proper pole architecture and facilitates pole focusing when centrioles are absent. Since approximately a third of cells entered anaphase with splayed poles and made multipolar chromosome segregation, segregation errors were significantly higher compared to centrinone treatment alone and untreated cells (Figure 43F). Taken together, these results suggest that spindle actin, by forming fine filaments in the polar region and along spindle microtubules, promotes spindle pole focusing and integrity.

### 4.12. Spindle position within the cell, symmetry of the metaphase plate and spindle pole architecture are impaired upon jasplakinolide treatment

Next, I wanted to investigate in more detail spindle architecture upon inhibition of actin branching, polymerization and depolymerization using STED microscopy. I treated RPE1 cells stably expressing CENP-A-GFP and Centrin1-GFP with CK666, latrunculin A and jasplakinolide and stained them with anti-α-tubulin antibody and SiR-actin (Figure 44A). The chemicals I use for untreated cells and for STED immunostaining disrupt the cell membranes. Since actin inhibitors disrupt cortical actin, I adapted the immunostaining protocol to preserve the cell membrane and spindle architecture. I excluded the first step in which cytoskeletal components are removes, since this step severely impairs cell membrane, and prolonged the permeabilization step after fixation (see Materials and methods). Even with mild permeabilization steps during immunostaining, I was able to get a successful actin staining within the spindle (Figure 44A, note that actin filaments are clearly visible throughout the metaphase plate area in control cells). The colocalization of actin filaments and spindle microtubules was comparable to colocalization analysed in Figure 36.

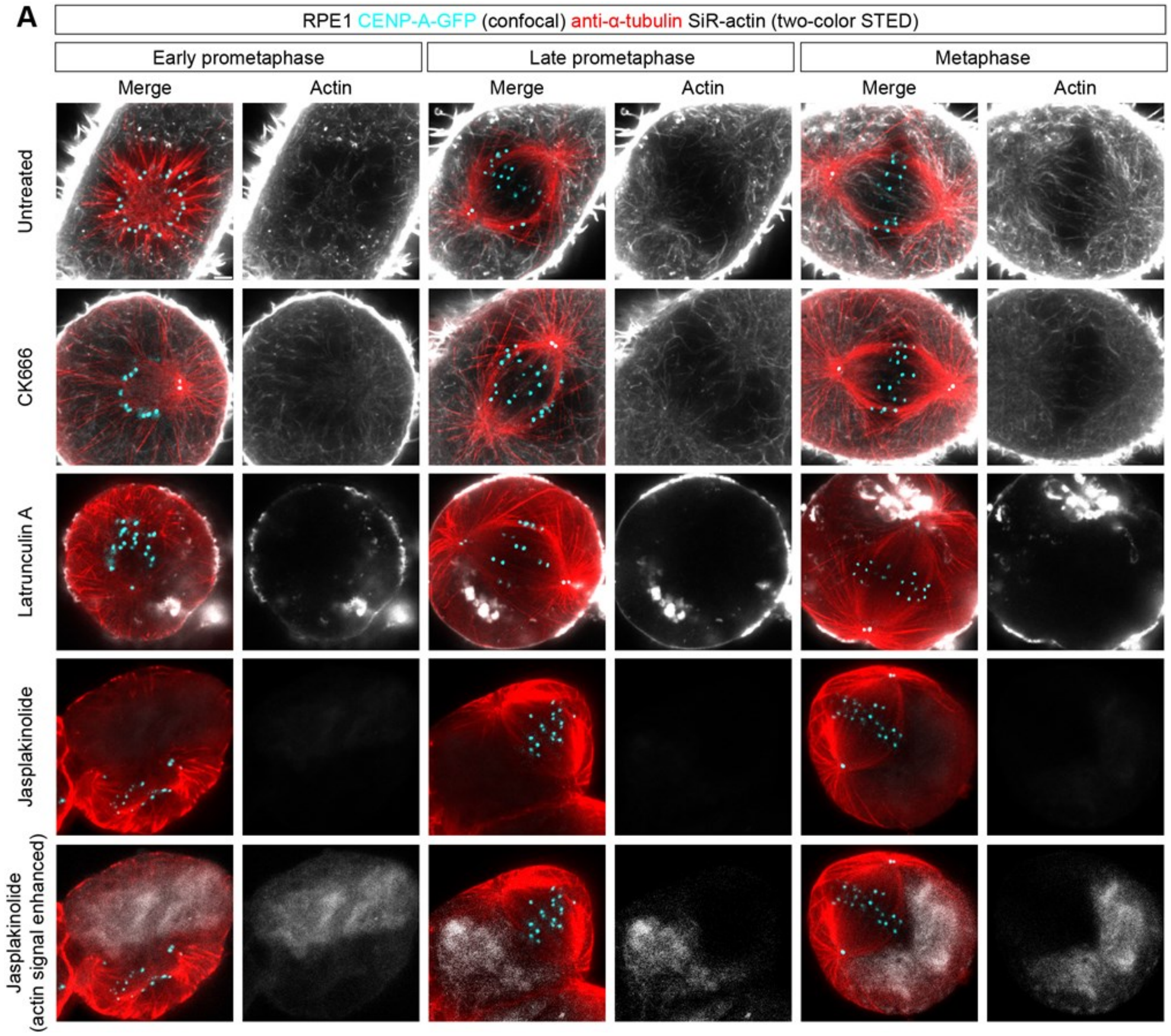

**Figure 44. Inhibition of actin polymerization and depolymerization severely disrupts actin architecture within the spindle, while branching inhibition has no effect.** (A) Two-color STED superresolution images of actin stained with SiR-actin (gray) and microtubules immunostained for α-tubulin (red) in RPE1 cells stably expressing CENP-A-GFP (cyan, confocal) in early prometaphase, late prometaphase and metaphase. Treatment of cells is denoted next to each panel. Single channels of actin are shown next to the merged images. Images show single z-planes of cells. Brightens and contrast are equally adjusted for actin and microtubules throughout the panels. Note that jasplakinolide treatment caused the monomeric actin to aggregate which was not sufficiently stained with SiR-actin so the last panel has enhanced brightness and contrast in order to visualise actin aggregates. Scale bar, 2 μm.

Surprisingly, upon CK666 treatment, actin architecture within the cell did not change significantly compared to untreated cells (Figure 44A – control and CK666). Cortical actin intensity was lower compared to untreated cells, but spindle actin filaments within the spindle were present in all mitotic phases and colocalized with spindle microtubules through prometaphase and metaphase. The results from live-cell imaging demonstrated that inhibition of actin branching does not influence spindle assembly and chromosome segregation significantly (Figure 41A-E). Given that the actin architecture is not severely impaired upon CK666 treatment within the spindle, the results from live-cell imaging are consistent.

On the other hand, latrunculin A and jasplakinolide treatment had severe effect on both cortical actin and actin within the spindle (Figure 44A – latrunculin A and jasplakinolide). Note that actin aggregates in jasplakinolide treatment are not visible when signals are equally adjusted throughout all images (Figure 44A, enhanced actin signal added to the last row for better visualisation of aggregates). Reason for that might be that SiR-actin cannot bind to aggregated monomeric actin and another staining approach needs to be optimized in the future experiments. Upon latrunculin A and jasplakinolide treatments cortical actin was reduced or absent, as previously reported (Bubb et al., 2000; Spector et al., 1989). Additionally, actin within the spindle was also absent. Taken together, inhibition of actin polymerization and depolymerization impairs spindle actin structure.

One of the prominent effects of actin inhibitors is on the spindle position within the cell. I quantified percentage of spindles positioned in the cell center, along the cell edge or when one spindle pole was near the cell edge (Figure 45A). Latrunculin A and jasplakinolide impaired spindle position severely, with 52.2 ± 7.4% and 85.7 ± 5.0% of spindles being positioned away from cell center, respectively (Figure 45A). In CK666-treated and untreated cells spindle was positioned in the center of the cell (Figure 45A). When spindles in latrunculin A or jasplakinolide treatment were positioned near the cell edge, their astral microtubules bent to adjust their shape to the cell membrane and extended along the cell edge (visible on Figure 45A, second and third image). Additionally, I analysed the position of metaphase plate within the spindle. Jasplakinolide treatment had a major effect on metaphase plate position, with 60.5 ± 7.5% of spindles having asymmetrically positioned metaphase plate (Figure 45B, see Materials and methods). Since majority of spindles in jasplakinolide treatment were positioned near the cell edge, causing curved spindle shape, this result is consistent with that. Taken together, disruption of actin polymerization and depolymerization affects spindle positioning within the cell as well as metaphase plate positioning within the spindle.

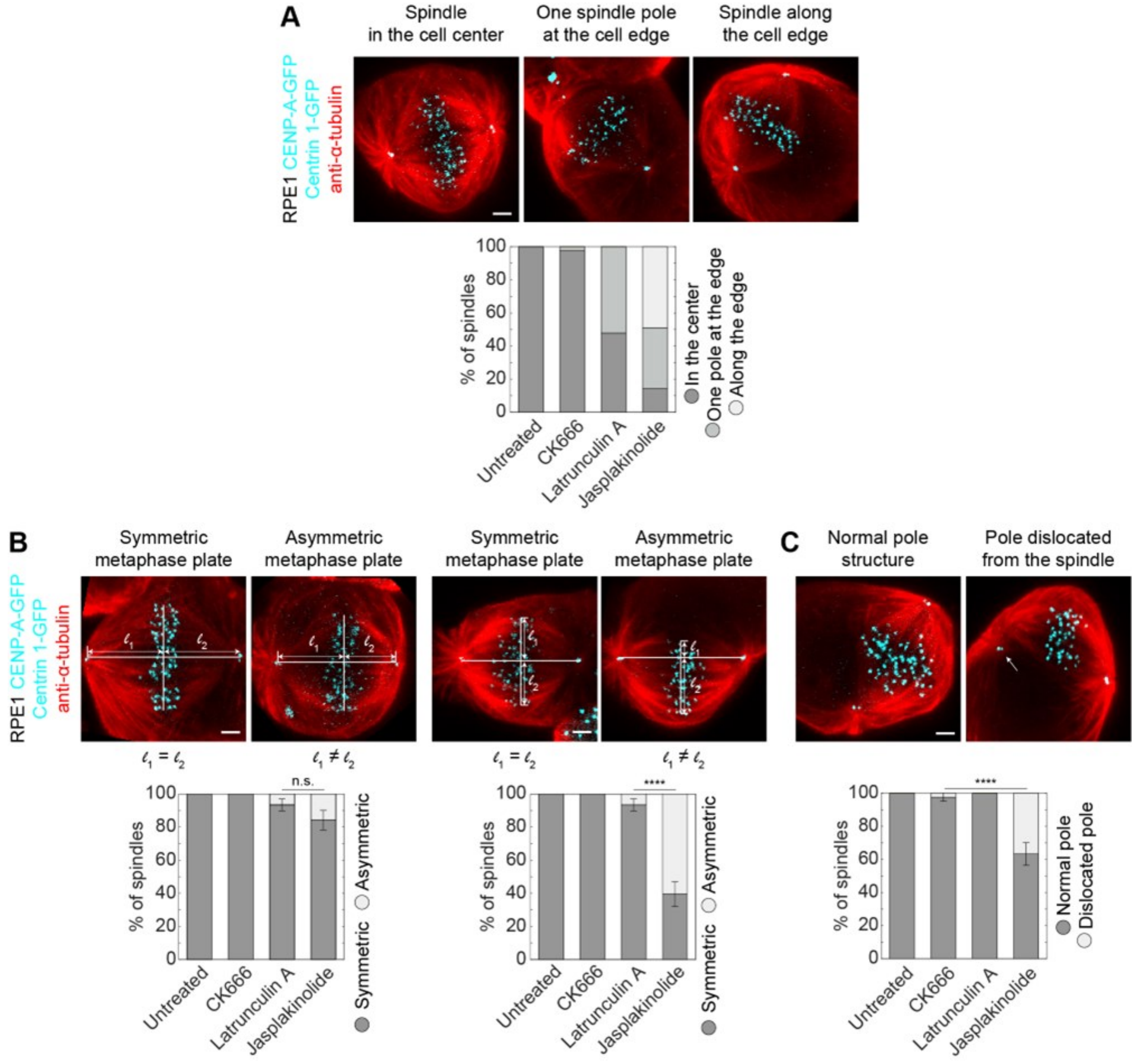

**Figure 45. Inhibition of actin polymerization and depolymerization impair spindle architecture.** (A - C) STED superresolution images of actin stained with SiR-actin (not shown) and microtubules immunostained for α-tubulin (red) in RPE1 cells stably expressing CENP-A-GFP (cyan, confocal) in late prometaphase and metaphase. All cells shown as an example are treated with jasplakinolide. Images show single z-planes of cells. (A) Percentage of spindles positioned in the cell center (dark gray), having one pole near cell edge (gray) and positioned along cell edge (light gray). Number of cells: 17 untreated, 41 CK666-, 46 latrunculin A- and 49 jasplakinolide-treated cells. (B) Percentage of spindles with symmetric (dark gray) or asymmetric (light gray) metaphase plate. The criteria for symmetric and asymmetric metaphase plate position is denoted on images above the graph. Number of cells: 17 untreated, 41 CK666-, 46 latrunculin A- and 43 (left graph) and 48 (right graph) jasplakinolide-treated cells. (C) Percentage of spindles with normal pole structure (dark gray) and dislocated pole (light gray). Example of dislocated pole is denoted with white arrow. Number of cells: 17 untreated, 41

**Figure 45. [continued from the previous page]** CK666-, 46 latrunculin A- and 49 jasplakinolide-treated cells. All results were obtained from three independent experiments, except for untreated cells where one independent experiment was performed. Statistical analysis: proportion Z test; p-value legend:<0.0001 (****), 0.0001–0.001 (***), 0.001–0.01 (**), 0.01–0.05 (*), ≥0.05 (ns). Scale bars, 2 µm.

Lastly, I analysed the spindle pole structure in images of fixed cells because jasplakinolide caused abnormal pole movement in live-cell imaging (Figure 45C). Pole displacement was defined as the relocation of the whole pole structure, including centrin signal along with astral microtubules, away from the spindle body (Figure 45C, displaced pole depicted with arrow). The percentage of cells with displaced pole was consistent between fixed and live-cell imaging (Figure 45C and Figure 43C, 36.7 ± 6.9% and 33.3 ± 6.4% of cells had displaced pole in fixed and live cells, respectively). This phenotype was not detected in other treatments (Figure 45C). These results suggest that actin stabilization impairs spindle pole structure. However, immunostaining in Figure 44 revealed that actin aggregates caused by jasplakinolide occupy a large volume of the cell and might serve as a mechanical constraint, causing spindle pole displacement during spindle elongation in mitosis.

### 4.13. The role of myosin X in spindle pole architecture

Myosin X has been demonstrated to have a role in bridging the microtubules and actin in *Xenopus* spindles and is required for normal pole structure (Woolner et al., 2008). Based on this fact, I hypothesized that it also might have a role in maintaining the pole structure in mitotic spindles. To test my hypothesis, I depleted myosin X in RPE1 cells stably expressing CENP-A-GFP and Centrin1-GFP and immunostained them with anti-α-tubulin antibody and SiR-actin (Figure 46A). Two-color STED microscopy revealed that spindle architecture remained unchanged after myosin X depletion (compare control cells in Figure 44A and myosin depleted cells in Figure 46A). Actin filaments were still present within the spindle and spindle pole morphology remained the same. Next, I checked if the siRNA depletion was efficient. I immunostained RPE1 cells stably expressing CENP-A-GFP and Centrin1-GFP with anti-myosin X antibody (Figure 46B). Based on the literature (Woolner et al., 2008), myosin X should be present at spindle poles, but antibody showed non-specific binding throughout the whole cell. Because of that, the results obtained for myosin X depletion are not reliable and this should be further tested in the future.

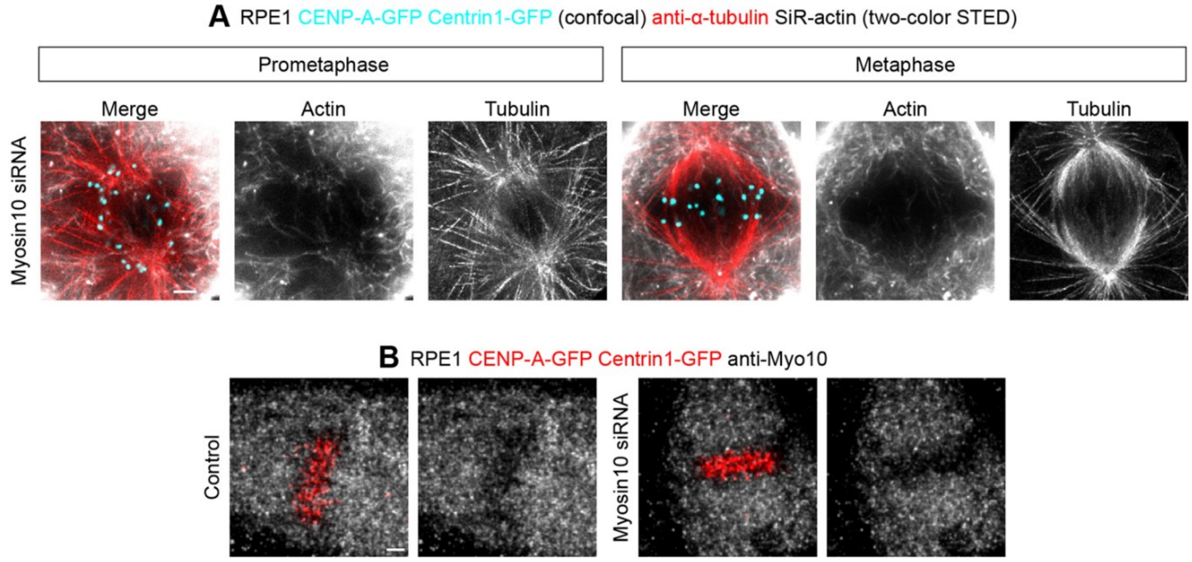

**Figure 46. Depletion efficiency of myosin X siRNA could not be assessed because of unspecific antibody binding.** (A) Two-color STED superresolution images of actin stained with SiR-actin (gray) and microtubules immunostained for α-tubulin (red) in myosin X-depleted RPE1 cells stably expressing CENP-A-GFP and Centrin1-GFP (both in cyan, confocal) in early prometaphase and metaphase. Single channels of actin and tubulin are shown next to the merged images. Images show single z-planes of cells. (B) Confocal images of control and myosin X-depleted RPE1 cells stably expressing CENP-A-GFP and Centrin1-GFP (both in red) and immunostained with anti-myosin X antibody (gray). Scale bars, 2 µm.

# 5. DISCUSSION

In this dissertation, I propose a model of the metaphase spindle in which the bridging fiber, which laterally connects sister k-fibers, forms by augmin-based nucleation of microtubules along the existing microtubules. The newly nucleated microtubules in the bridging fiber create an antiparallel overlap in which the microtubules slide apart, generating a pushing force that the bridging fiber exerts on its k-fibers. In doing so, the bridging fiber works together with k-fibers to produce tension and maintain the appropriate orientation of sister kinetochores parallel to the spindle axis, thereby preventing merotelic attachments and ensuring mitotic fidelity (Figure 47).

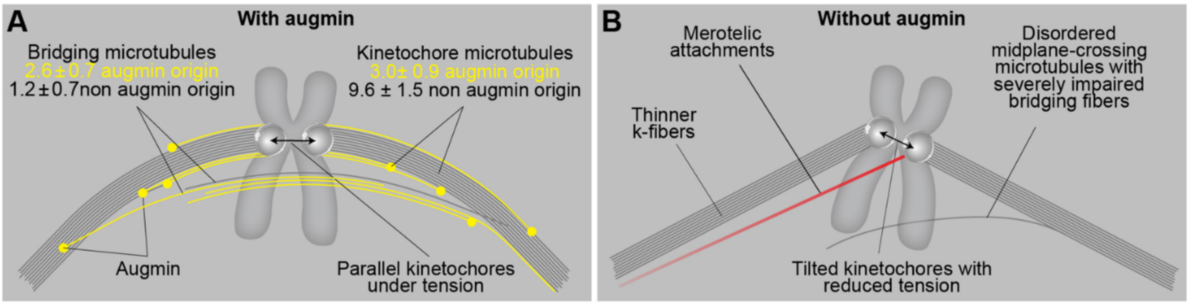

**Figure 47. A model of augmin-dependent nucleation of bridging microtubules with their contribution to mitotic fidelity.** (A) Bridging microtubules are to a large extent formed by augmin-dependent nucleation. They ensure the alignment of sister kinetochores parallel to the spindle axis and the interkinetochore tension. Augmin-nucleated microtubules (yellow) and microtubules nucleated through other pathways (gray) in bridging and k-fibers are shown together with the number of microtubules in each group, as estimated from HAUS6 depletion experiments (See Results). (B) Impaired structure of bridging fibers upon augmin depletion leads to weaker interkinetochore tension and increased tilt of the kinetochores, which puts kinetochores at risk of interacting with additional microtubules (red), resulting in merotelic attachments.

My work shows that the depletion of the augmin complex by silencing the HAUS6 or HAUS8 subunits causes severe thinning of bridging fibers in metaphase spindles, combined with the appearance of wavy and disordered midplane-crossing microtubules. Thus, I conclude that the predominant nucleation of bridging microtubules by the augmin complex enables their directional bundling along the sister k-fibers, in agreement with previous observations on directionality of microtubule growth (David et al., 2019; Kamasaki et al., 2013). K-fibers are also thinner in the absence of augmin, though to a lesser extent, indicating that they are largely nucleated in an augmin-independent manner, at the centrosome or kinetochores and chromosomes. This is in agreement with previous electron microscopy studies of mammalian spindles, where k-fiber microtubules are observed to typically reach the centrosome, while sometimes also extending from the kinetochores with their minus ends within the spindle (Kiewisz et al., n.d.; McDonald et al., 1992; Sikirzhytski et al., 2018), the latter likely representing a combination of microtubules nucleated either at the kinetochores or by the augmin complex. In contrast, most midplane-crossing microtubules, which likely correspond to bridging fibers, start at different points along the k-fiber (Mastronarde et al., 1993). Electron tomography of spindles in RPE1 cells confirms this result by showing that microtubule minus ends are found along the k-fiber, less than 50 nm from the k-fiber wall and at a distance 2–4 µm from the pole (O'Toole et al., 2020). As I found that the same number of microtubules in bridging and k-fibers is nucleated by augmin, I propose that the existing microtubules orient the growth of augmin-nucleated microtubules (David et al., 2019; Kamasaki et al., 2013), which later become kinetochore microtubules if their plus end binds to the kinetochore or bridging microtubules if they grow past the kinetochore and interact with the bridging or kinetochore microtubules on the other side. However, as there are less microtubules in the bridging fiber to begin with, augmin-mediated nucleation becomes the predominant pathway of their nucleation.

Previous work shows that augmin depletion results in a decrease of interkinetochore distance (Uehara et al., 2009; Zhu et al., 2008), a readout of tension, but it remains unclear if this is due to impaired k-fibers or perturbation of other microtubules. Treatment of cells with a microtubule-destabilizing agent that results in thinner k-fibers causes a reduction of the interkinetochore tension (Dudka et al., 2018), supporting the former possibility. However, a similar effect on the interkinetochore tension was observed upon perturbation of the bridging fiber by removing the microtubule crosslinker PRC1 (Jagrić et al., 2021; Kajtez et al., 2016; Polak et al., 2017), in agreement with the latter possibility. When looking at a subset of kinetochore pairs that have a bridging fiber and those that do not, I find that the tension was more compromised in the latter group. Notably, tension is independent of the k-fiber thickness within each group and depends on the presence or the absence of bridging fibers even when the effect of k-fibers is excluded. Although my experiments cannot directly discern the exact contribution of the bridging and k-fiber impairment in the decrease of tension on kinetochores, they reveal that augmin-generated bridging microtubules have a significant and specific role in the maintenance of interkinetochore tension.

Considering the importance of the interkinetochore tension for the accuracy of cell division (Lampson and Grishchuk, 2017), the maintenance of tension by the bridging fiber might represent an important mechanism for silencing of the spindle assembly checkpoint (Musacchio and Salmon, 2007; Nicklas et al., 1995), supported by the fact augmin-depleted cells with characteristically compromised bridging fibers have extensive mitotic delays (Wu et al., 2008). However, recent work suggests that the reduction of interkinetochore tension caused by k-fiber thinning does not necessarily lead to checkpoint activation, but instead may sometimes result in reduced anaphase A speed caused by low microtubule occupancy, followed by a subsequent increase in lagging chromosomes (Dudka et al., 2018). As proteins involved in bridging fiber nucleation and crosslinking, including HAUS6, HAUS8, and PRC1 have all been linked to various types of cancer (ICGC/TCGA, 2020, retrieved by using cBioPortal (Cerami et al., 2012; Gao et al., 2013)), it is plausible that impairment of bridging fibers also leads to such increase in lagging chromosomes and contributes to aneuploidy in cancers. Indeed, once the checkpoint is weakened by Mad2 depletion, lagging chromosomes that appear following augmin depletion have a reduced interkinetochore distance, which is consistent with previous findings on lazy chromosomes (Sen et al., 2021). However, contrary to previous findings in cells with intact bridging fibers, in which there is no connection between lagging chromosomes and tilt of their kinetochores (Sen et al., 2021), I find that kinetochores of lagging chromosomes in augmin-depleted cells predominantly form a large tilt with respect to the spindle axis. This suggests that the lack of bridging fibers represents a specific mechanism of predisposing the kinetochore to merotelic attachments by tilting the kinetochores and exposing their surface to the microtubules from the opposite pole. The tilted kinetochore pair is more likely to encounter additional microtubules also because midplane-crossing microtubules that form following augmin depletion no longer exhibit directional growth, but are instead wavy and extend in various directions. Once a merotelic attachment forms, it may further amplify the existing tilt due to pulling by additional microtubules in a skewed direction. Moreover, erroneous attachments might be less likely to undergo error correction in augmin-depleted cells, as bridging fibers may serve as tracks that guide Aurora B within the Chromosome Passenger Complex towards the kinetochores to correct the errors (Matković et al., 2022). In addition to predisposing the kinetochore to merotelic attachments through impaired bridging fibers, thinning of k-fibers upon augmin depletion might ultimately be responsible for the inability to resolve merotelic attachments, as strong k-fibers are necessary to ensure proper segregation of kinetochores during anaphase (Dudka et al., 2018). Altogether, my results reveal that augmin is the leading nucleator of bridging fibers and suggest a delicate interplay of bridging and k-fibers in the maintenance of spindle organization, kinetochore tension and mitotic fidelity.

Furthermore, I propose a model where spindle actin is involved in maintaining spindle pole integrity and bipolar cell division. During prometaphase, actin filaments first colocalize with astral microtubules and spindle poles. The colocalization shifts towards the spindle microtubules but remains on spindle poles in late prometaphase and metaphase. This interplay between spindle actin and microtubules ensures proper focusing of spindle poles and bipolar division, a prerequisite for proper chromosome segregation (Figure 48).

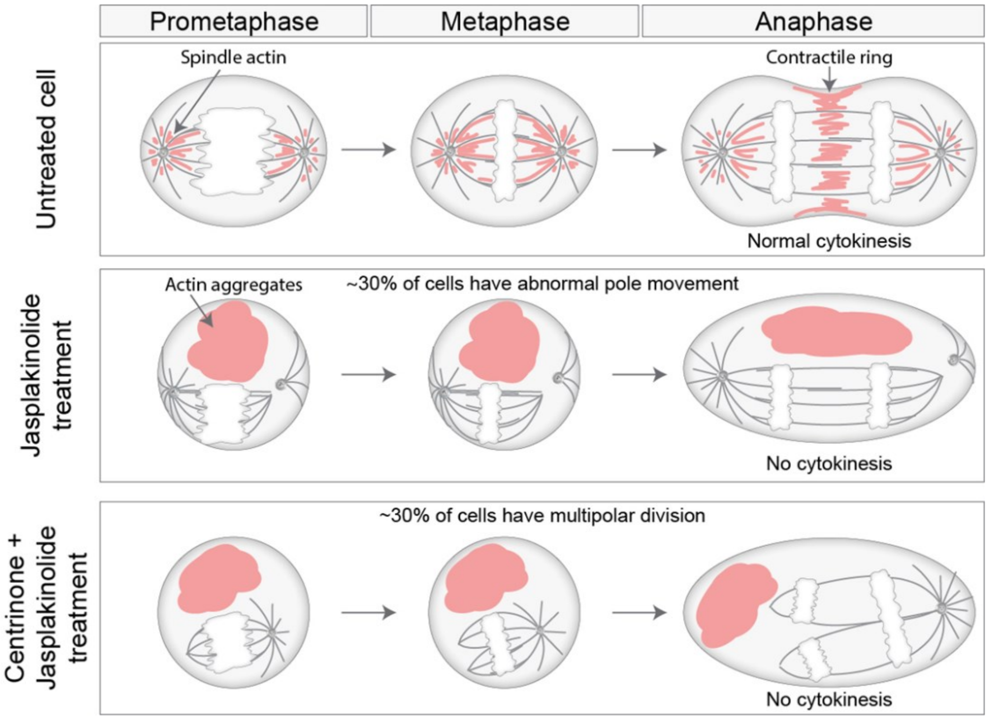

**Figure 48. Spindle actin promotes pole focusing and bipolar cell division.** During prometaphase, actin filaments first colocalize with astral microtubules and spindle poles. The colocalization shifts towards the spindle microtubules but remains on spindle poles in late prometaphase and metaphase. This interplay between spindle actin and microtubules ensures proper focusing of spindle poles and bipolar division, a prerequisite for proper chromosome segregation. Jasplakinolide treatment causes abnormal pole movements and multipolar divisions.

In this dissertation, I utilize two-color STED microscopy to determine the precise spatial distribution of actin filaments and microtubules within the spindle. It is demonstrated that actin colocalizes with nuclear envelope just before NEBD (Booth et al., 2019) and with k-fibers preceding their growth during early prometaphase (Plessner et al., 2019), but when it comes to late prometaphase and metaphase, conventional confocal microscopy techniques were not enough to determine the interplay between spindle actin and microtubules within the metaphase plate area. Here, I demonstrate with high spatial resolution that actin first colocalizes with astral microtubules of nascent spindle, but later this colocalization is shifted towards the spindle microtubules as those astral microtubules most likely become incorporated into the spindle and form distinct microtubule bundles. Furthermore, actin accumulates more around the polar region, in agreement with (Colin et al., 2018; Farina et al., 2016; Inoue et al., 2019).

Several studies have demonstrated that centrosomes serve as an actin organizing centers and that actin regulates the growth of microtubules in that region (Colin et al., 2018; Farina et al., 2019, 2016; Inoue et al., 2019). Interestingly, I demonstrated that shortly after NEBD, when perinuclear actin contracts (Booth et al., 2019), it is also present around the chromosomes as a mesh inside the nucleus. This mesh is later reorganized into the filaments that colocalize with astral microtubules in early prometaphase, which raises the question if actin can serve as a scaffold for microtubule nucleation around chromosomes. It has been proposed that spindle actin precedes growth od microtubules soon after NEBD (Plessner et al., 2019), so it would be interesting to see if spindle actin localized on poles and actin mesh around chromosomes work together to form filaments required for microtubule nucleation, therefore precisely regulating microtubule dynamics during mitosis. Inhibition of actin branching and actin stabilization significantly prolongs mitotic duration, although it does not affect final mitotic fidelity, suggesting that this first step takes longer when actin is not present. However, inhibition of actin polymerization does not prolong mitosis, so my work so far cannot neither confirm nor contradict that actin precedes microtubules and serves as a scaffold for their nucleation. Based on all results, I speculate that in normal conditions actin guides nucleation of astral microtubules in nascent spindle, but in its absence, microtubules can still normally nucleate without major issues.

When actin polymerization and branching are inhibited, there is no effect on spindle architecture or mitotic fidelity, which is in agreement with the literature (Colin et al., 2018; Lancaster et al., 2013; Uzbekov et al., 2002). The major effect on spindle architecture is on spindle poles when actin was stabilized by jasplakinolide. In this case, the pole movement is abnormal and pole focusing impaired in case without centrioles. These results suggest that spindle actin is involved in preserving spindle pole architecture. However, jasplakinolide causes aggregation of monomeric actin into aggregates, impairs cortical actin and therefore impairs cell architecture. It is known that flat cells often exhibit multipolar spindles (Lancaster et al., 2013), so it would be interesting to see if jasplakinolide-treated cells were more flattened compared to untreated cells and if this multipolar divisions arise from impaired cell morphology. The flattened geometry might also cause the amorphous mass of actin to constrain the spindle near the cell membrane. This physical barrier can press the spindle, so during elongation poles can be dislocated from the spindle body. In the future, it would be interesting to introduce beads, assembled into a mass by magnets, into the healthy cell to see if the effect on spindle poles will be similar. That way it could be discerned if spindle actin has a role in maintaining pole architecture, or the phenotype in my experiments arises from physical barriers inside the cell. One surprising result is that jasplakinolide and latrunculin A treatment produce different effects, although the impaired actin filament structure after the treatments is similar. However, in my experiments cell rounding is not significantly affected in latrunculin A-treated cells, which might be the reason that spindle can assemble normally, and mitotic progression is not impaired.

It was recently proposed that spindle actin has a role in chromosome congression and segregation (Plessner et al., 2019), however I got contrary results with CK666 inhibitor. My results demonstrate that mitotic timing is significantly longer compared to untreated cells, which aligns with this research, however I do not observe any spindle morphology defects or segregation errors. In my experiments, the actin filament morphology after CK666 treatment does not change significantly, explaining my results. Since I use the same cell type and the same concentration of inhibitor as used in (Plessner et al., 2019), I cannot currently explain the observed differences. Actin branching in the future can be impaired by using different concentrations and timing of CK666 inhibitor to see if it impacts spindle assembly and chromosome segregation.

All inhibitors used in the thesis have effect not only on spindle actin, but also on other actin types throughout the cell – cortical actin, actin clouds and retraction fibers. Because of that, many phenotypes I got in my thesis cannot be solely attributed to the spindle actin. For example, it is known that impairment of cortical actin and actin clouds impairs spindle positioning and orientation within the cell (Kunda and Baum, 2009), which is also visible in my experiments when I use latrunculin A and jasplakinolide. In the future experiments, more focus should be put onto perturbing only spindle actin to determine its role in mitotic progression. Since low temperatures are known to depolymerize microtubules and actin filaments (DeLuca et al., 2006; Pokorná et al., 2004; Sacristan et al., 2018; Silkworth et al., 2011), it would be interesting to see if different timing and temperature exposures could depolymerize only thin spindle actin filaments in mitotic cells. One of the approaches would also be to use a photoswitchable versions of actin inhibitors, like opto-latrunculin (Vepřek et al., 2023) and opto-jasplakinolide (Borowiak et al., 2020), to depolymerize and stabilize actin filaments specifically in the spindle region, respectively. Additionally, more experiments with myosin X and FAM110A should be done in the future because it was demonstrated that they bind both actin and microtubules simultaneously (Aquino-Perez et al., 2024, p. 11; Woolner et al., 2008).

In acentrioal meiotic systems, spindle actin replaces the functions of astral microtubules and plays a significant role in spindle migration, anchoring and rotation (Uraji et al., 2018). It is recently demonstrated that it is also involved in chromosome congression and segregation (Mogessie and Schuh, 2017), a role which is demonstrated also for spindle actin in somatic cells (Booth et al., 2019; Plessner et al., 2019). However, my results show that spindle actin is involved in the maintenance of pole architecture and preventing multipolar divisions, while the effect on spindle architecture and chromosome movements is not that evident. These effects can also arise from other actin types and mechanisms, as discussed previously, which raises a question if spindle actin in somatic cells serves just as an actin pool that accumulates during mitosis and is needed for contraction ring later in anaphase. However, it would be interesting to see what factors regulate that accumulation. So far, my experiments suggest spindle actin's role in spindle pole focusing and bipolar divisions by forming fine filaments in the polar region and along spindle microtubules.

# 6. CONCLUSION

In this thesis, I employed stimulated emission depletion (STED) superresolution imaging and cutting edge live-cell imaging to determine the role of augmin and spindle actin in chromosome congression, spindle architecture and mitotic fidelity. I demonstrated that augmin is vital for the formation of uniformly arranged parallel units consisting of sister kinetochore fibers connected by a bridging fiber. This ordered geometry helps both prevent and resolve merotelic attachments. Whereas augmin-nucleated bridging fibers prevent merotelic attachments by creating a nearly parallel and highly bundled microtubule arrangement unfavorable for creating additional attachments, augmin-nucleated k-fibers produce robust force required to resolve errors during anaphase. STED microscopy revealed that bridging fibers were impaired twice as much as k-fibers following augmin depletion. The complete absence of bridging fibers from a significant portion of kinetochore pairs, especially in the inner part of the spindle, resulted in the specific reduction of the interkinetochore distance. Regarding the role of spindle actin in spindle architecture, I showed that after nuclear envelope breakdown, actin surrounds chromosomes and soon becomes colocalized with astral microtubules and spindle poles in early prometaphase. In late prometaphase and metaphase, the colocalization shifts to the spindle microtubules. Actin stabilization causes abnormal pole behaviour during mitosis, with poles being displaced away from the spindle pole and moving through the cytoplasm. Additionally, in case when centrioles are absent, spindle actin facilitates pole focusing.

Taken together, I propose a model where augmin promotes mitotic fidelity by generating assemblies consisting of bridging and kinetochore fibers that align sister kinetochores to face opposite poles, thereby preventing erroneous attachments. On the other hand, spindle actin, by forming fine filaments in the polar region and along spindle microtubules, promotes spindle pole focusing and bipolar cell divisions.

To conclude, my research provided deeper insights into the roles of augmin and spindle actin during mitosis. It completed the picture of augmin's role in nucleating different classes of microtubules and revealed a mechanism required for proper chromosome segregation. Furthermore, I uncovered previously unknown roles of spindle actin during mitosis in mammalian cells. Future research will address newly emerging questions about the molecular factors that regulate distribution of spindle actin during mitosis and contribute to its role.

# 7. REFERENCES

Aillaud, C., Bosc, C., Peris, L., Bosson, A., Heemeryck, P., Van Dijk, J., Le Friec, J., Boulan, B., Vossier, F., Sanman, L.E., Syed, S., Amara, N., Couté, Y., Lafanechère, L., Denarier, E., Delphin, C., Pelletier, L., Humbert, S., Bogyo, M., Andrieux, A., Rogowski, K., Moutin, M.-J., 2017. Vasohibins/SVBP are tubulin carboxypeptidases (TCPs) that regulate neuron differentiation. Science 358, 1448–1453. https://doi.org/10.1126/science.aao4165

Alberts, B., Johnson, A., Lewis, J., Morgan, D., Raff, M., Roberts, K., Walter, P., 2015. Molecular biology of the cell, Sixth edition. ed. Garland Science, Taylor and Francis Group, New York, NY.

Almeida, A.C., Soares-de-Oliveira, J., Drpic, D., Cheeseman, L.P., Damas, J., Lewin, H.A., Larkin, D.M., Aguiar, P., Pereira, A.J., Maiato, H., 2022. Augmin-dependent microtubule self-organization drives kinetochore fiber maturation in mammals. Cell Reports 39, 110610. https://doi.org/10.1016/j.celrep.2022.110610

Andrews, P.D., Ovechkina, Y., Morrice, N., Wagenbach, M., Duncan, K., Wordeman, L., Swedlow, J.R., 2004. Aurora B regulates MCAK at the mitotic centromere. Dev Cell 6, 253–268. https://doi.org/10.1016/s1534-5807(04)00025-5

Antonio, C., Ferby, I., Wilhelm, H., Jones, M., Karsenti, E., Nebreda, A.R., Vernos, I., 2000. Xkid, a Chromokinesin Required for Chromosome Alignment on the Metaphase Plate. Cell 102, 425–435. https://doi.org/10.1016/S0092-8674(00)00048-9

Aquino-Perez, C., Safaralizade, M., Podhajecky, R., Wang, H., Lansky, Z., Grosse, R., Macurek, L., 2024. FAM110A promotes mitotic spindle formation by linking microtubules with actin cytoskeleton. Proceedings of the National Academy of Sciences 121, e2321647121. https://doi.org/10.1073/pnas.2321647121

Asthana, J., Cade, N.I., Normanno, D., Lim, W.M., Surrey, T., 2021. Gradual compaction of the central spindle decreases its dynamicity in PRC1 and EB1 gene-edited cells. Life Sci. Alliance 4, e202101222. https://doi.org/10.26508/lsa.202101222

Azoury, J., Lee, K.W., Georget, V., Rassinier, P., Leader, B., Verlhac, M.-H., 2008. Spindle positioning in mouse oocytes relies on a dynamic meshwork of actin filaments. Curr Biol 18, 1514–1519. https://doi.org/10.1016/j.cub.2008.08.044

Barford, D., 2020. Structural interconversions of the anaphase-promoting complex/cyclosome (APC/C) regulate cell cycle transitions. Curr Opin Struct Biol 61, 86–97. https://doi.org/10.1016/j.sbi.2019.11.010

Barisic, M., Aguiar, P., Geley, S., Maiato, H., 2014. Kinetochore motors drive congression of peripheral polar chromosomes by overcoming random arm-ejection forces. Nat Cell Biol 16, 1249–1256. https://doi.org/10.1038/ncb3060

Barisic, M., Silva e Sousa, R., Tripathy, S.K., Magiera, M.M., Zaytsev, A.V., Pereira, A.L., Janke, C., Grishchuk, E.L., Maiato, H., 2015. Microtubule detyrosination guides chromosomes during mitosis. Science 348, 799–803. https://doi.org/10.1126/science.aaa5175

Booth, A.J., Yue, Z., Eykelenboom, J.K., Stiff, T., Luxton, G.G., Hochegger, H., Tanaka, T.U., 2019. Contractile acto-myosin network on nuclear envelope remnants positions human chromosomes for mitosis. eLife 8, e46902. https://doi.org/10.7554/eLife.46902

Borowiak, M., Küllmer, F., Gegenfurtner, F., Peil, S., Nasufovic, V., Zahler, S., Thorn-Seshold, O., Trauner, D., Arndt, H.-D., 2020. Optical manipulation of F-actin with photoswitchable small molecules. J Am Chem Soc 142, 9240–9249. https://doi.org/10.1021/jacs.9b12898

Breitsprecher, D., Goode, B.L., 2013. Formins at a glance. J Cell Sci 126, 1–7. https://doi.org/10.1242/jcs.107250

Bringmann, H., Hyman, A.A., 2005. A cytokinesis furrow is positioned by two consecutive signals. Nature 436, 731–734. https://doi.org/10.1038/nature03823

Brust-Mascher, I., Sommi, P., Cheerambathur, D.K., Scholey, J.M., 2009. Kinesin-5-dependent poleward flux and spindle length control in Drosophila embryo mitosis. Mol Biol Cell 20, 1749–1762. https://doi.org/10.1091/mbc.e08-10-1033

Bubb, M.R., Senderowicz, A.M., Sausville, E.A., Duncan, K.L., Korn, E.D., 1994. Jasplakinolide, a cytotoxic natural product, induces actin polymerization and competitively inhibits the binding of phalloidin to F-actin. J Biol Chem 269, 14869–14871.

Bubb, M.R., Spector, I., Beyer, B.B., Fosen, K.M., 2000. Effects of Jasplakinolide on the Kinetics of Actin Polymerization: AN EXPLANATION FOR CERTAIN IN VIVO OBSERVATIONS*. Journal of Biological Chemistry 275, 5163–5170. https://doi.org/10.1074/jbc.275.7.5163

Buđa, R., Vukušić, K., Tolić, I.M., 2017. Dissection and characterization of microtubule bundles in the mitotic spindle using femtosecond laser ablation, in: Lecuit, T. (Ed.), Methods in Cell Biology, Cell Polarity and Morphogenesis. Academic Press, pp. 81–101. https://doi.org/10.1016/bs.mcb.2016.11.007

Calarco-Gillam, P.D., Siebert, M.C., Hubble, R., Mitchison, T., Kirschner, M., 1983. Centrosome development in early mouse embryos as defined by an autoantibody against pericentriolar material. Cell 35, 621–629. https://doi.org/10.1016/0092-8674(83)90094-6

Carazo-Salas, R.E., Guarguaglini, G., Gruss, O.J., Segref, A., Karsenti, E., Mattaj, I.W., 1999. Generation of GTP-bound Ran by RCC1 is required for chromatin-induced mitotic spindle formation. Nature 400, 178–181. https://doi.org/10.1038/22133

Cerami, E., Gao, J., Dogrusoz, U., Gross, B.E., Sumer, S.O., Aksoy, B.A., Jacobsen, A., Byrne, C.J., Heuer, M.L., Larsson, E., Antipin, Y., Reva, B., Goldberg, A.P., Sander, C., Schultz, N., 2012. The cBio cancer genomics portal: an open platform for exploring multidimensional cancer genomics data. Cancer Discov 2, 401–404. https://doi.org/10.1158/2159-8290.CD-12-0095

Cheeseman, I.M., Chappie, J.S., Wilson-Kubalek, E.M., Desai, A., 2006. The conserved KMN network constitutes the core microtubule-binding site of the kinetochore. Cell 127, 983–997. https://doi.org/10.1016/j.cell.2006.09.039

Cheeseman, I.M., Desai, A., 2008. Molecular architecture of the kinetochore–microtubule interface. Nat Rev Mol Cell Biol 9, 33–46. https://doi.org/10.1038/nrm2310

Cimini, D., Howell, B., Maddox, P., Khodjakov, A., Degrassi, F., Salmon, E.D., 2001. Merotelic Kinetochore Orientation Is a Major Mechanism of Aneuploidy in Mitotic Mammalian Tissue Cells. J Cell Biol 153, 517–528.

Colin, A., Singaravelu, P., Théry, M., Blanchoin, L., Gueroui, Z., 2018. Actin-Network Architecture Regulates Microtubule Dynamics. Current Biology 28, 2647-2656.e4. https://doi.org/10.1016/j.cub.2018.06.028

Conduit, P.T., Wainman, A., Raff, J.W., 2015. Centrosome function and assembly in animal cells. Nat Rev Mol Cell Biol 16, 611–624. https://doi.org/10.1038/nrm4062

Coué, M., Brenner, S.L., Spector, I., Korn, E.D., 1987. Inhibition of actin polymerization by latrunculin A. FEBS Lett 213, 316–318. https://doi.org/10.1016/0014-5793(87)81513-2

Dancker, P., Löw, I., Hasselbach, W., Wieland, T., 1975. Interaction of actin with phalloidin: polymerization and stabilization of F-actin. Biochim Biophys Acta 400, 407–414. https://doi.org/10.1016/0005-2795(75)90196-8

David, A.F., Roudot, P., Legant, W.R., Betzig, E., Danuser, G., Gerlich, D.W., 2019. Augmin accumulation on long-lived microtubules drives amplification and kinetochore-directed growth. J Cell Biol 218, 2150–2168. https://doi.org/10.1083/jcb.201805044

DeLuca, J.G., Gall, W.E., Ciferri, C., Cimini, D., Musacchio, A., Salmon, E.D., 2006. Kinetochore microtubule dynamics and attachment stability are regulated by Hec1. Cell 127, 969–982. https://doi.org/10.1016/j.cell.2006.09.047

Deng, M., Li, R., 2009. Sperm chromatin-induced ectopic polar body extrusion in mouse eggs after ICSI and delayed egg activation. PLoS One 4, e7171. https://doi.org/10.1371/journal.pone.0007171

di Pietro, F., Echard, A., Morin, X., 2016. Regulation of mitotic spindle orientation: an integrated view. EMBO Rep 17, 1106–1130. https://doi.org/10.15252/embr.201642292

Dogterom, M., Koenderink, G.H., 2019. Actin–microtubule crosstalk in cell biology. Nat Rev Mol Cell Biol 20, 38–54. https://doi.org/10.1038/s41580-018-0067-1

Dudka, D., Noatynska, A., Smith, C.A., Liaudet, N., McAinsh, A.D., Meraldi, P., 2018. Complete microtubule–kinetochore occupancy favours the segregation of merotelic attachments. Nat Commun 9, 2042. https://doi.org/10.1038/s41467-018-04427-x

Dumont, J., Million, K., Sunderland, K., Rassinier, P., Lim, H., Leader, B., Verlhac, M.-H., 2007. Formin-2 is required for spindle migration and for the late steps of cytokinesis in mouse oocytes. Dev Biol 301, 254–265. https://doi.org/10.1016/j.ydbio.2006.08.044

Elbaz, J., Reizel, Y., Nevo, N., Galiani, D., Dekel, N., 2010. Epithelial cell transforming protein 2 (ECT2) depletion blocks polar body extrusion and generates mouse oocytes containing two metaphase II spindles. Endocrinology 151, 755–765. https://doi.org/10.1210/en.2009-0830

Farina, F., Gaillard, J., Guérin, C., Couté, Y., Sillibourne, J., Blanchoin, L., Théry, M., 2016. The centrosome is an actin-organizing center. Nat Cell Biol 18, 65–75. https://doi.org/10.1038/ncb3285

Farina, F., Ramkumar, N., Brown, L., Samandar Eweis, D., Anstatt, J., Waring, T., Bithell, J., Scita, G., Thery, M., Blanchoin, L., Zech, T., Baum, B., 2019. Local actin nucleation tunes centrosomal microtubule nucleation during passage through mitosis. EMBO J 38, e99843. https://doi.org/10.15252/embj.201899843

Ferreira, L.T., Maiato, H., 2021. Prometaphase. Seminars in Cell & Developmental Biology 117, 52–61. https://doi.org/10.1016/j.semcdb.2021.06.004

Foe, V.E., von Dassow, G., 2008. Stable and dynamic microtubules coordinately shape the myosin activation zone during cytokinetic furrow formation. J Cell Biol 183, 457–470. https://doi.org/10.1083/jcb.200807128

Gabel, C.A., Li, Z., DeMarco, A.G., Zhang, Z., Yang, J., Hall, M.C., Barford, D., Chang, L., 2022. Molecular architecture of the augmin complex. Nat Commun 13, 5449. https://doi.org/10.1038/s41467-022-33227-7

Ganem, N.J., Upton, K., Compton, D.A., 2005. Efficient mitosis in human cells lacking poleward microtubule flux. Curr Biol 15, 1827–1832. https://doi.org/10.1016/j.cub.2005.08.065

Gao, J., Aksoy, B.A., Dogrusoz, U., Dresdner, G., Gross, B., Sumer, S.O., Sun, Y., Jacobsen, A., Sinha, R., Larsson, E., Cerami, E., Sander, C., Schultz, N., 2013. Integrative analysis of complex cancer genomics and clinical profiles using the cBioPortal. Sci Signal 6, pl1. https://doi.org/10.1126/scisignal.2004088

Gloerich, M., Bianchini, J.M., Siemers, K.A., Cohen, D.J., Nelson, W.J., 2017. Cell division orientation is coupled to cell–cell adhesion by the E-cadherin/LGN complex. Nat Commun 8, 13996. https://doi.org/10.1038/ncomms13996

Goldschmidt-Clermont, P.J., Furman, M.I., Wachsstock, D., Safer, D., Nachmias, V.T., Pollard, T.D., 1992. The control of actin nucleotide exchange by thymosin beta 4 and profilin. A potential regulatory mechanism for actin polymerization in cells. Mol Biol Cell 3, 1015–1024.

Goley, E.D., Welch, M.D., 2006. The ARP2/3 complex: an actin nucleator comes of age. Nat Rev Mol Cell Biol 7, 713–726. https://doi.org/10.1038/nrm2026

Goshima, G., Mayer, M., Zhang, N., Stuurman, N., Vale, R.D., 2008. Augmin: a protein complex required for centrosome-independent microtubule generation within the spindle. J Cell Biol 181, 421–429. https://doi.org/10.1083/jcb.200711053

Goshima, G., Wollman, R., Goodwin, S.S., Zhang, N., Scholey, J.M., Vale, R.D., Stuurman, N., 2007. Genes required for mitotic spindle assembly in Drosophila S2 cells. Science 316, 417–421. https://doi.org/10.1126/science.1141314

Gregan, J., Polakova, S., Zhang, L., Tolić-Nørrelykke, I.M., Cimini, D., 2011. Merotelic kinetochore attachment: causes and effects. Trends in Cell Biology 21, 374. https://doi.org/10.1016/j.tcb.2011.01.003

Gregory, S.L., Ebrahimi, S., Milverton, J., Jones, W.M., Bejsovec, A., Saint, R., 2008. Cell division requires a direct link between microtubule-bound RacGAP and Anillin in the contractile ring. Curr Biol 18, 25–29. https://doi.org/10.1016/j.cub.2007.11.050

Hardwick, K.G., Johnston, R.C., Smith, D.L., Murray, A.W., 2000. MAD3 encodes a novel component of the spindle checkpoint which interacts with Bub3p, Cdc20p, and Mad2p. J Cell Biol 148, 871–882. https://doi.org/10.1083/jcb.148.5.871

Hayward, D., Metz, J., Pellacani, C., Wakefield, J.G., 2014. Synergy between multiple microtubule-generating pathways confers robustness to centrosome-driven mitotic spindle formation. Dev Cell 28, 81–93. https://doi.org/10.1016/j.devcel.2013.12.001

Heald, R., Tournebize, R., Blank, T., Sandaltzopoulos, R., Becker, P., Hyman, A., Karsenti, E., 1996. Self-organization of microtubules into bipolar spindles around artificial chromosomes in Xenopus egg extracts. Nature 382, 420–425. https://doi.org/10.1038/382420a0

Hell, S.W., Wichmann, J., 1994. Breaking the diffraction resolution limit by stimulated emission: stimulated-emission-depletion fluorescence microscopy. Opt Lett 19, 780–782. https://doi.org/10.1364/ol.19.000780

Hetrick, B., Han, M.S., Helgeson, L.A., Nolen, B.J., 2013. Small molecules CK-666 and CK-869 inhibit actin-related protein 2/3 complex by blocking an activating conformational change. Chem Biol 20, 701–712. https://doi.org/10.1016/j.chembiol.2013.03.019

Homma, K., Saito, J., Ikebe, R., Ikebe, M., 2001. Motor function and regulation of myosin X. J Biol Chem 276, 34348–34354. https://doi.org/10.1074/jbc.M104785200

Howell, B.J., McEwen, B.F., Canman, J.C., Hoffman, D.B., Farrar, E.M., Rieder, C.L., Salmon, E.D., 2001. Cytoplasmic dynein/dynactin drives kinetochore protein transport to the spindle poles and has a role in mitotic spindle checkpoint inactivation. J Cell Biol 155, 1159–1172. https://doi.org/10.1083/jcb.200105093

Huff, J., 2015. The Airyscan detector from ZEISS: confocal imaging with improved signal-to-noise ratio and super-resolution. Nat Methods 12, i–ii. https://doi.org/10.1038/nmeth.f.388

Inoue, D., Obino, D., Pineau, J., Farina, F., Gaillard, J., Guerin, C., Blanchoin, L., Lennon-Duménil, A., Théry, M., 2019. Actin filaments regulate microtubule growth at the centrosome. EMBO J 38. https://doi.org/10.15252/embj.201899630

Jagrić, M., Risteski, P., Martinčić, J., Milas, A., Tolić, I.M., 2021. Optogenetic control of PRC1 reveals its role in chromosome alignment on the spindle by overlap length-dependent forces. eLife 10, e61170. https://doi.org/10.7554/eLife.61170

Ji, Z., Gao, H., Yu, H., 2015. Kinetochore attachment sensed by competitive Mps1 and microtubule binding to Ndc80C. Science 348, 1260–1264. https://doi.org/10.1126/science.aaa4029

Joglekar, A.P., 2016. A Cell Biological Perspective on Past, Present and Future Investigations of the Spindle Assembly Checkpoint. Biology 5, 44. https://doi.org/10.3390/biology5040044

Kajtez, J., Solomatina, A., Novak, M., Polak, B., Vukušić, K., Rüdiger, J., Cojoc, G., Milas, A., Šumanovac Šestak, I., Risteski, P., Tavano, F., Klemm, A.H., Roscioli, E., Welburn, J., Cimini, D., Glunčić, M., Pavin, N., Tolić, I.M., 2016. Overlap microtubules link sister k-fibres and balance the forces on bi-oriented kinetochores. Nat Commun 7, 10298. https://doi.org/10.1038/ncomms10298

Kamasaki, T., O'Toole, E., Kita, S., Osumi, M., Usukura, J., McIntosh, J.R., Goshima, G., 2013. Augmin-dependent microtubule nucleation at microtubule walls in the spindle. J Cell Biol 202, 25–33. https://doi.org/10.1083/jcb.201304031

Kapoor, T.M., Lampson, M.A., Hergert, P., Cameron, L., Cimini, D., Salmon, E.D., McEwen, B.F., Khodjakov, A., 2006. Chromosomes Can Congress to the Metaphase Plate Before Biorientation. Science 311, 388–391. https://doi.org/10.1126/science.1122142

Khodjakov, A., Cole, R.W., Oakley, B.R., Rieder, C.L., 2000. Centrosome-independent mitotic spindle formation in vertebrates. Curr Biol 10, 59–67. https://doi.org/10.1016/s0960-9822(99)00276-6

Khodjakov, A., Copenagle, L., Gordon, M.B., Compton, D.A., Kapoor, T.M., 2003. Minus-end capture of preformed kinetochore fibers contributes to spindle morphogenesis. Journal of Cell Biology 160, 671–683. https://doi.org/10.1083/jcb.200208143

Kiewisz, R., Fabig, G., Conway, W., Baum, D., Needleman, D., Müller-Reichert, T., n.d. Three-dimensional structure of kinetochore-fibers in human mitotic spindles. eLife 11, e75459. https://doi.org/10.7554/eLife.75459

Kimmy Ho, C.-M., Hotta, T., Kong, Z., Tracy Zeng, C.J., Sun, J., Julie Lee, Y.-R., Liu, B., 2011. Augmin Plays a Critical Role in Organizing the Spindle and Phragmoplast Microtubule Arrays in Arabidopsis. The Plant Cell 23, 2606–2618. https://doi.org/10.1105/tpc.111.086892

Kirschner, M., Mitchison, T., 1986. Beyond self-assembly: From microtubules to morphogenesis. Cell 45, 329–342. https://doi.org/10.1016/0092-8674(86)90318-1

Kita, A.M., Swider, Z.T., Erofeev, I., Halloran, M.C., Goryachev, A.B., Bement, W.M., 2019. Spindle-F-actin interactions in mitotic spindles in an intact vertebrate epithelium. Mol Biol Cell 30, 1645–1654. https://doi.org/10.1091/mbc.E19-02-0126

Klar, T.A., Hell, S.W., 1999. Subdiffraction resolution in far-field fluorescence microscopy. Opt Lett 24, 954–956. https://doi.org/10.1364/ol.24.000954

Kollman, J.M., Merdes, A., Mourey, L., Agard, D.A., 2011. Microtubule nucleation by γ-tubulin complexes. Nat Rev Mol Cell Biol 12, 709–721. https://doi.org/10.1038/nrm3209

Kraus, J., Travis, S.M., King, M.R., Petry, S., 2023. Augmin is a Ran-regulated spindle assembly factor. Journal of Biological Chemistry 299, 104736. https://doi.org/10.1016/j.jbc.2023.104736

Kunda, P., Baum, B., 2009. The actin cytoskeleton in spindle assembly and positioning. Trends in Cell Biology 19, 174–179. https://doi.org/10.1016/j.tcb.2009.01.006

Kwon, M., Bagonis, M., Danuser, G., Pellman, D., 2015. Direct Microtubule-Binding by Myosin-10 Orients Centrosomes toward Retraction Fibers and Subcortical Actin Clouds. Dev Cell 34, 323–337. https://doi.org/10.1016/j.devcel.2015.06.013

Lampson, M.A., Grishchuk, E.L., 2017. Mechanisms to Avoid and Correct Erroneous Kinetochore-Microtubule Attachments. Biology (Basel) 6, E1. https://doi.org/10.3390/biology6010001

Lan, W., Zhang, X., Kline-Smith, S.L., Rosasco, S.E., Barrett-Wilt, G.A., Shabanowitz, J., Hunt, D.F., Walczak, C.E., Stukenberg, P.T., 2004. Aurora B phosphorylates centromeric MCAK and regulates its localization and microtubule depolymerization activity. Curr Biol 14, 273–286. https://doi.org/10.1016/j.cub.2004.01.055

Lancaster, O.M., Le Berre, M., Dimitracopoulos, A., Bonazzi, D., Zlotek-Zlotkiewicz, E., Picone, R., Duke, T., Piel, M., Baum, B., 2013. Mitotic Rounding Alters Cell Geometry to Ensure Efficient Bipolar Spindle Formation. Developmental Cell 25, 270–283. https://doi.org/10.1016/j.devcel.2013.03.014

Lawo, S., Bashkurov, M., Mullin, M., Ferreria, M.G., Kittler, R., Habermann, B., Tagliaferro, A., Poser, I., Hutchins, J.R.A., Hegemann, B., Pinchev, D., Buchholz, F., Peters, J.-M., Hyman, A.A., Gingras, A.-C., Pelletier, L., 2009. HAUS, the 8-subunit human Augmin complex, regulates centrosome and spindle integrity. Curr Biol 19, 816–826. https://doi.org/10.1016/j.cub.2009.04.033

Lechler, T., Mapelli, M., 2021. Spindle positioning and its impact on vertebrate tissue architecture and cell fate. Nat Rev Mol Cell Biol 22, 691–708. https://doi.org/10.1038/s41580-021-00384-4

Li, J., Dallmayer, M., Kirchner, T., Musa, J., Grünewald, T.G.P., 2018. PRC1: Linking Cytokinesis, Chromosomal Instability, and Cancer Evolution. Trends Cancer 4, 59–73. https://doi.org/10.1016/j.trecan.2017.11.002

Li, Y., Yu, W., Liang, Y., Zhu, X., 2007. Kinetochore dynein generates a poleward pulling force to facilitate congression and full chromosome alignment. Cell Res 17, 701–712. https://doi.org/10.1038/cr.2007.65

Liu, D., Lampson, M.A., 2009. Regulation of kinetochore-microtubule attachments by Aurora B kinase. Biochem Soc Trans 37, 976–980. https://doi.org/10.1042/BST0370976

Liu, D., Vader, G., Vromans, M.J.M., Lampson, M.A., Lens, S.M.A., 2009. Sensing Chromosome Bi-Orientation by Spatial Separation of Aurora B Kinase from Kinetochore Substrates. Science 323, 1350–1353. https://doi.org/10.1126/science.1167000

Liu, L., Trimarchi, J.R., Oldenbourg, R., Keefe, D.L., 2000. Increased birefringence in the meiotic spindle provides a new marker for the onset of activation in living oocytes. Biol Reprod 63, 251–258. https://doi.org/10.1095/biolreprod63.1.251

Lu, H., Zhao, Q., Jiang, H., Zhu, T., Xia, P., Seffens, W., Aikhionbare, F., Wang, D., Dou, Z., Yao, X., 2014. Characterization of Ring-Like F-Actin Structure as a Mechanical Partner for Spindle Positioning in Mitosis. PLOS ONE 9, e102547. https://doi.org/10.1371/journal.pone.0102547

Lukinavičius, G., Reymond, L., D'Este, E., Masharina, A., Göttfert, F., Ta, H., Güther, A., Fournier, M., Rizzo, S., Waldmann, H., Blaukopf, C., Sommer, C., Gerlich, D.W., Arndt, H.-D., Hell, S.W., Johnsson, K., 2014. Fluorogenic probes for live-cell imaging of the cytoskeleton. Nat Methods 11, 731–733. https://doi.org/10.1038/nmeth.2972

MacLean-Fletcher, S., Pollard, T.D., 1980. Mechanism of action of cytochalasin B on actin. Cell 20, 329–341. https://doi.org/10.1016/0092-8674(80)90619-4

Magidson, V., O'Connell, C.B., Lončarek, J., Paul, R., Mogilner, A., Khodjakov, A., 2011. The spatial arrangement of chromosomes during prometaphase facilitates spindle assembly. Cell 146, 555–567. https://doi.org/10.1016/j.cell.2011.07.012

Maiato, H., Gomes, A.M., Sousa, F., Barisic, M., 2017. Mechanisms of Chromosome Congression during Mitosis. Biology (Basel) 6, 13. https://doi.org/10.3390/biology6010013

Maiato, H., Rieder, C.L., Khodjakov, A., 2004. Kinetochore-driven formation of kinetochore fibers contributes to spindle assembly during animal mitosis. J Cell Biol 167, 831–840. https://doi.org/10.1083/jcb.200407090

Maresca, T.J., Groen, A.C., Gatlin, J.C., Ohi, R., Mitchison, T.J., Salmon, E.D., 2009. Spindle assembly in the absence of a RanGTP gradient requires localized CPC activity. Curr Biol 19, 1210–1215. https://doi.org/10.1016/j.cub.2009.05.061

Maro, B., Johnson, M.H., Pickering, S.J., Flach, G., 1984. Changes in actin distribution during fertilization of the mouse egg. J Embryol Exp Morphol 81, 211–237.

Mastronarde, D.N., McDonald, K.L., Ding, R., McIntosh, J.R., 1993. Interpolar spindle microtubules in PTK cells. J Cell Biol 123, 1475–1489. https://doi.org/10.1083/jcb.123.6.1475

Matković, J., Ghosh, S., Ćosić, M., Eibes, S., Barišić, M., Pavin, N., Tolić, I.M., 2022. Kinetochore- and chromosome-driven transition of microtubules into bundles promotes spindle assembly. Nat Commun 13, 7307. https://doi.org/10.1038/s41467-022-34957-4

Matthies, H.J., McDonald, H.B., Goldstein, L.S., Theurkauf, W.E., 1996. Anastral meiotic spindle morphogenesis: role of the non-claret disjunctional kinesin-like protein. J Cell Biol 134, 455–464. https://doi.org/10.1083/jcb.134.2.455

Mayr, M.I., Hümmer, S., Bormann, J., Grüner, T., Adio, S., Woehlke, G., Mayer, T.U., 2007. The human kinesin Kif18A is a motile microtubule depolymerase essential for chromosome congression. Curr Biol 17, 488–498. https://doi.org/10.1016/j.cub.2007.02.036

McDonald, K.L., O'Toole, E.T., Mastronarde, D.N., McIntosh, J.R., 1992. Kinetochore microtubules in PTK cells. J Cell Biol 118, 369–383. https://doi.org/10.1083/jcb.118.2.369

McIntosh, J.R., 2016. Mitosis. Cold Spring Harb Perspect Biol 8, a023218. https://doi.org/10.1101/cshperspect.a023218

McKinley, K.L., Sekulic, N., Guo, L.Y., Tsinman, T., Black, B.E., Cheeseman, I.M., 2015. The CENP-L-N Complex Forms a Critical Node in an Integrated Meshwork of Interactions at the Centromere-Kinetochore Interface. Mol Cell 60, 886–898. https://doi.org/10.1016/j.molcel.2015.10.027

Mitchison, T. j, 2005. Mechanism and function of poleward flux in Xenopus extract meiotic spindles. Philosophical Transactions of the Royal Society B: Biological Sciences 360, 623–629. https://doi.org/10.1098/rstb.2004.1616

Mitchison, T.J., 1992. Actin based motility on retraction fibers in mitotic PtK2 cells. Cell Motility 22, 135–151. https://doi.org/10.1002/cm.970220207

Mitsushima, M., Aoki, K., Ebisuya, M., Matsumura, S., Yamamoto, T., Matsuda, M., Toyoshima, F., Nishida, E., 2010. Revolving movement of a dynamic cluster of actin filaments during mitosis. Journal of Cell Biology 191, 453–462. https://doi.org/10.1083/jcb.201007136

Miyamoto, D.T., Perlman, Z.E., Burbank, K.S., Groen, A.C., Mitchison, T.J., 2004. The kinesin Eg5 drives poleward microtubule flux in Xenopus laevis egg extract spindles. J Cell Biol 167, 813–818. https://doi.org/10.1083/jcb.200407126

Mogessie, B., Scheffler, K., Schuh, M., 2018. Assembly and Positioning of the Oocyte Meiotic Spindle. Annu Rev Cell Dev Biol 34, 381–403. https://doi.org/10.1146/annurev-cellbio-100616-060553

Mogessie, B., Schuh, M., 2017. Actin protects mammalian eggs against chromosome segregation errors. Science 357, eaal1647. https://doi.org/10.1126/science.aal1647

Mollinari, C., Kleman, J.-P., Jiang, W., Schoehn, G., Hunter, T., Margolis, R.L., 2002. PRC1 is a microtubule binding and bundling protein essential to maintain the mitotic spindle midzone. J Cell Biol 157, 1175–1186. https://doi.org/10.1083/jcb.200111052

Musacchio, A., Salmon, E.D., 2007. The spindle-assembly checkpoint in space and time. Nat Rev Mol Cell Biol 8, 379–393. https://doi.org/10.1038/nrm2163

Nicklas, R.B., Ward, S.C., Gorbsky, G.J., 1995. Kinetochore chemistry is sensitive to tension and may link mitotic forces to a cell cycle checkpoint. J Cell Biol 130, 929–939. https://doi.org/10.1083/jcb.130.4.929

Nieuwenhuis, J., Adamopoulos, A., Bleijerveld, O.B., Mazouzi, A., Stickel, E., Celie, P., Altelaar, M., Knipscheer, P., Perrakis, A., Blomen, V.A., Brummelkamp, T.R., 2017. Vasohibins encode tubulin detyrosinating activity. Science 358, 1453–1456. https://doi.org/10.1126/science.aao5676

Novak, M., Polak, B., Simunić, J., Boban, Z., Kuzmić, B., Thomae, A.W., Tolić, I.M., Pavin, N., 2018. The mitotic spindle is chiral due to torques within microtubule bundles. Nat Commun 9, 3571. https://doi.org/10.1038/s41467-018-06005-7

O'Toole, E., Morphew, M., McIntosh, J.R., 2020. Electron tomography reveals aspects of spindle structure important for mechanical stability at metaphase. MBoC 31, 184–195. https://doi.org/10.1091/mbc.E19-07-0405

Ou, G.S., Chen, Z.L., Yuan, M., 2002. Jasplakinolide reversibly disrupts actin filaments in suspension-cultured tobacco BY-2 cells. Protoplasma 219, 168–175. https://doi.org/10.1007/s007090200018

Pavin, N., Tolić, I.M., 2016. Self-Organization and Forces in the Mitotic Spindle. Annu Rev Biophys 45, 279–298. https://doi.org/10.1146/annurev-biophys-062215-010934

Petry, S., 2016. Mechanisms of Mitotic Spindle Assembly. Annu Rev Biochem 85, 659–683. https://doi.org/10.1146/annurev-biochem-060815-014528

Petry, S., Groen, A.C., Ishihara, K., Mitchison, T.J., Vale, R.D., 2013. Branching microtubule nucleation in Xenopus egg extracts mediated by augmin and TPX2. Cell 152, 768–777. https://doi.org/10.1016/j.cell.2012.12.044

Petry, S., Pugieux, C., Nédélec, F.J., Vale, R.D., 2011. Augmin promotes meiotic spindle formation and bipolarity in Xenopus egg extracts. Proc Natl Acad Sci U S A 108, 14473–14478. https://doi.org/10.1073/pnas.1110412108

Pfender, S., Kuznetsov, V., Pleiser, S., Kerkhoff, E., Schuh, M., 2011. Spire-type actin nucleators cooperate with Formin-2 to drive asymmetric oocyte division. Curr Biol 21, 955–960. https://doi.org/10.1016/j.cub.2011.04.029

Plessner, M., Knerr, J., Grosse, R., 2019. Centrosomal Actin Assembly Is Required for Proper Mitotic Spindle Formation and Chromosome Congression. iScience 15, 274–281. https://doi.org/10.1016/j.isci.2019.04.022

Pokorná, J., Schwarzerová, K., Zelenková, S., Petrášek, J., Janotová, I., Čapková, V., Opatrný, Z., 2004. Sites of actin filament initiation and reorganization in cold-treated tobacco cells. Plant, Cell & Environment 27, 641–653. https://doi.org/10.1111/j.1365-3040.2004.01186.x

Polak, B., Risteski, P., Lesjak, S., Tolić, I.M., 2017. PRC1-labeled microtubule bundles and kinetochore pairs show one-to-one association in metaphase. EMBO Rep 18, 217–230. https://doi.org/10.15252/embr.201642650

Poser, I., Sarov, M., Hutchins, J.R.A., Hériché, J.-K., Toyoda, Y., Pozniakovsky, A., Weigl, D., Nitzsche, A., Hegemann, B., Bird, A.W., Pelletier, L., Kittler, R., Hua, S., Naumann, R., Augsburg, M., Sykora, M.M., Hofemeister, H., Zhang, Y., Nasmyth, K., White, K.P., Dietzel, S., Mechtler, K., Durbin, R., Stewart, A.F., Peters, J.-M., Buchholz, F., Hyman, A.A., 2008. BAC TransgeneOmics: a high-throughput method for exploration of protein function in mammals. Nat Methods 5, 409–415. https://doi.org/10.1038/nmeth.1199

Prosser, S.L., Pelletier, L., 2017. Mitotic spindle assembly in animal cells: a fine balancing act. Nat Rev Mol Cell Biol 18, 187–201. https://doi.org/10.1038/nrm.2016.162

Prota, A.E., Magiera, M.M., Kuijpers, M., Bargsten, K., Frey, D., Wieser, M., Jaussi, R., Hoogenraad, C.C., Kammerer, R.A., Janke, C., Steinmetz, M.O., 2013. Structural basis of tubulin tyrosination by tubulin tyrosine ligase. J Cell Biol 200, 259–270. https://doi.org/10.1083/jcb.201211017

Raybin, D., Flavin, M., 1975. An enzyme tyrosylating alpha-tubulin and its role in microtubule assembly. Biochem Biophys Res Commun 65, 1088–1095. https://doi.org/10.1016/s0006-291x(75)80497-9

Redemann, S., Pecreaux, J., Goehring, N.W., Khairy, K., Stelzer, E.H.K., Hyman, A.A., Howard, J., 2010. Membrane invaginations reveal cortical sites that pull on mitotic spindles in one-cell C. elegans embryos. PLoS One 5, e12301. https://doi.org/10.1371/journal.pone.0012301

Risteski, P., Božan, D., Jagrić, M., Bosilj, A., Pavin, N., Tolić, I.M., 2022. Length-dependent poleward flux of sister kinetochore fibers promotes chromosome alignment. Cell Rep 40, 111169. https://doi.org/10.1016/j.celrep.2022.111169

Risteski, P., Jagrić, M., Pavin, N., Tolić, I.M., 2021. Biomechanics of chromosome alignment at the spindle midplane. Current Biology 31, R574–R585. https://doi.org/10.1016/j.cub.2021.03.082

Rosenblatt, J., Cramer, L.P., Baum, B., McGee, K.M., 2004. Myosin II-Dependent Cortical Movement Is Required for Centrosome Separation and Positioning during Mitotic Spindle Assembly. Cell 117, 361–372. https://doi.org/10.1016/S0092-8674(04)00341-1

Sacristan, C., Ahmad, M.U.D., Keller, J., Fermie, J., Groenewold, V., Tromer, E., Fish, A., Melero, R., Carazo, J.M., Klumperman, J., Musacchio, A., Perrakis, A., Kops, G.J., 2018. Dynamic kinetochore size regulation promotes microtubule capture and chromosome biorientation in mitosis. Nat Cell Biol 20, 800–810. https://doi.org/10.1038/s41556-018-0130-3

Sampath, S.C., Ohi, R., Leismann, O., Salic, A., Pozniakovski, A., Funabiki, H., 2004. The chromosomal passenger complex is required for chromatin-induced microtubule stabilization and spindle assembly. Cell 118, 187–202. https://doi.org/10.1016/j.cell.2004.06.026

Schaar, B.T., Chan, G.K.T., Maddox, P., Salmon, E.D., Yen, T.J., 1997. CENP-E Function at Kinetochores Is Essential for Chromosome Alignment. J Cell Biol 139, 1373–1382.

Schuh, M., Ellenberg, J., 2008. A new model for asymmetric spindle positioning in mouse oocytes. Curr Biol 18, 1986–1992. https://doi.org/10.1016/j.cub.2008.11.022

Sen, O., Harrison, J.U., Burroughs, N.J., McAinsh, A.D., 2021. Kinetochore life histories reveal an Aurora-B-dependent error correction mechanism in anaphase. Developmental Cell 56, 3082-3099.e5. https://doi.org/10.1016/j.devcel.2021.10.007

Shen, A., Liu, L., Huang, Y., Shen, Z., Wu, M., Chen, X., Wu, X., Lin, X., Chen, Y., Li, L., Cheng, Y., Chu, J., Sferra, T.J., Wei, L., Zhuang, Q., Peng, J., 2022. Down-Regulating HAUS6 Suppresses Cell Proliferation by Activating the p53/p21 Pathway in Colorectal Cancer. Front Cell Dev Biol 9, 772077. https://doi.org/10.3389/fcell.2021.772077

Sikirzhytski, V., Renda, F., Tikhonenko, I., Magidson, V., McEwen, B.F., Khodjakov, A., 2018. Microtubules assemble near most kinetochores during early prometaphase in human cells. Journal of Cell Biology 217, 2647–2659. https://doi.org/10.1083/jcb.201710094

Silkworth, W.T., Nardi, I.K., Paul, R., Mogilner, A., Cimini, D., 2011. Timing of centrosome separation is important for accurate chromosome segregation. MBoC 23, 401–411. https://doi.org/10.1091/mbc.e11-02-0095

Simerly, C., Nowak, G., de Lanerolle, P., Schatten, G., 1998. Differential expression and functions of cortical myosin IIA and IIB isotypes during meiotic maturation, fertilization, and mitosis in mouse oocytes and embryos. Mol Biol Cell 9, 2509–2525. https://doi.org/10.1091/mbc.9.9.2509

Skibbens, R.V., Skeen, V.P., Salmon, E.D., 1993. Directional instability of kinetochore motility during chromosome congression and segregation in mitotic newt lung cells: a push-pull mechanism. J Cell Biol 122, 859–875. https://doi.org/10.1083/jcb.122.4.859

Song, J.-G., King, M.R., Zhang, R., Kadzik, R.S., Thawani, A., Petry, S., 2018. Mechanism of how augmin directly targets the γ-tubulin ring complex to microtubules. J Cell Biol 217, 2417–2428. https://doi.org/10.1083/jcb.201711090

Spector, I., Shochet, N.R., Blasberger, D., Kashman, Y., 1989. Latrunculins--novel marine macrolides that disrupt microfilament organization and affect cell growth: I. Comparison with cytochalasin D. Cell Motil Cytoskeleton 13, 127–144. https://doi.org/10.1002/cm.970130302

Steblyanko, Y., Rajendraprasad, G., Osswald, M., Eibes, S., Jacome, A., Geley, S., Pereira, A.J., Maiato, H., Barisic, M., 2020. Microtubule poleward flux in human cells is driven by the coordinated action of four kinesins. EMBO J 39, e105432. https://doi.org/10.15252/embj.2020105432

Štimac, V., Koprivec, I., Manenica, M., Simunić, J., Tolić, I.M., 2022. Augmin prevents merotelic attachments by promoting proper arrangement of bridging and kinetochore fibers. eLife 11, e83287. https://doi.org/10.7554/eLife.83287

Sudakin, V., Chan, G.K.T., Yen, T.J., 2001. Checkpoint inhibition of the APC/C in HeLa cells is mediated by a complex of BUBR1, BUB3, CDC20, and MAD2. J Cell Biol 154, 925–936. https://doi.org/10.1083/jcb.200102093

Théry, M., Bornens, M., 2006. Cell shape and cell division. Curr Opin Cell Biol 18, 648–657. https://doi.org/10.1016/j.ceb.2006.10.001

Théry, M., Racine, V., Pépin, A., Piel, M., Chen, Y., Sibarita, J.-B., Bornens, M., 2005. The extracellular matrix guides the orientation of the cell division axis. Nat Cell Biol 7, 947–953. https://doi.org/10.1038/ncb1307

Tolić, I.M., Pavin, N., 2016. Bridging the gap between sister kinetochores. Cell Cycle 15, 1169–1170. https://doi.org/10.1080/15384101.2016.1157976

Toyoshima, F., Nishida, E., 2007. Integrin-mediated adhesion orients the spindle parallel to the substratum in an EB1- and myosin X-dependent manner. EMBO J 26, 1487–1498. https://doi.org/10.1038/sj.emboj.7601599

Tulu, U.S., Fagerstrom, C., Ferenz, N.P., Wadsworth, P., 2006. Molecular requirements for kinetochore-associated microtubule formation in mammalian cells. Curr Biol 16, 536–541. https://doi.org/10.1016/j.cub.2006.01.060

Uehara, R., Goshima, G., 2010. Functional central spindle assembly requires de novo microtubule generation in the interchromosomal region during anaphase. J Cell Biol 191, 259–267. https://doi.org/10.1083/jcb.201004150

Uehara, R., Kamasaki, T., Hiruma, S., Poser, I., Yoda, K., Yajima, J., Gerlich, D.W., Goshima, G., 2016. Augmin shapes the anaphase spindle for efficient cytokinetic furrow ingression and abscission. Mol Biol Cell 27, 812–827. https://doi.org/10.1091/mbc.E15-02-0101

Uehara, R., Nozawa, R., Tomioka, A., Petry, S., Vale, R.D., Obuse, C., Goshima, G., 2009. The augmin complex plays a critical role in spindle microtubule generation for mitotic progression and cytokinesis in human cells. Proc Natl Acad Sci U S A 106, 6998–7003. https://doi.org/10.1073/pnas.0901587106

Uraji, J., Scheffler, K., Schuh, M., 2018. Functions of actin in mouse oocytes at a glance. Journal of Cell Science 131, jcs218099. https://doi.org/10.1242/jcs.218099

Ustinova, K., Ruhnow, F., Gili, M., Surrey, T., 2023. Microtubule binding of the human augmin complex is directly controlled by importins and Ran-GTP. J Cell Sci 136, jcs261096. https://doi.org/10.1242/jcs.261096

Uzbekov, R., Kireyev, I., Prigent, C., 2002. Centrosome separation: respective role of microtubules and actin filaments. Biology of the Cell 94, 275–288. https://doi.org/10.1016/S0248-4900(02)01202-9

van Oostende Triplet, C., Jaramillo Garcia, M., Haji Bik, H., Beaudet, D., Piekny, A., 2014. Anillin interacts with microtubules and is part of the astral pathway that defines cortical domains. J Cell Sci 127, 3699–3710. https://doi.org/10.1242/jcs.147504

Vanoosthuyse, V., Hardwick, K.G., 2009. A Novel Protein Phosphatase 1-Dependent Spindle Checkpoint Silencing Mechanism. Curr Biol 19, 1176–1181. https://doi.org/10.1016/j.cub.2009.05.060

Vepřek, N.A., Cooper, M.H., Laprell, L., Yang, E.J.-N., Folkerts, S., Bao, R., Oertner, T.G., Pon, L.A., Zuchero, J.B., Trauner, D.H., 2023. Optical Control of G-Actin with a Photoswitchable Latrunculin. bioRxiv 2023.07.17.549222. https://doi.org/10.1101/2023.07.17.549222

Verma, V., Maresca, T.J., 2019. Direct observation of branching MT nucleation in living animal cells. J Cell Biol 218, 2829–2840. https://doi.org/10.1083/jcb.201904114

Viais, R., Fariña-Mosquera, M., Villamor-Payà, M., Watanabe, S., Palenzuela, L., Lacasa, C., Lüders, J., 2021. Augmin deficiency in neural stem cells causes p53-dependent apoptosis and aborts brain development. Elife 10, e67989. https://doi.org/10.7554/eLife.67989

Vitre, B., Taulet, N., Guesdon, A., Douanier, A., Dosdane, A., Cisneros, M., Maurin, J., Hettinger, S., Anguille, C., Taschner, M., Lorentzen, E., Delaval, B., 2020. IFT proteins interact with HSET to promote supernumerary centrosome clustering in mitosis. EMBO reports 21, e49234. https://doi.org/10.15252/embr.201949234

Vukušić, K., Buđa, R., Bosilj, A., Milas, A., Pavin, N., Tolić, I.M., 2017. Microtubule Sliding within the Bridging Fiber Pushes Kinetochore Fibers Apart to Segregate Chromosomes. Dev Cell 43, 11-23.e6. https://doi.org/10.1016/j.devcel.2017.09.010

Vukusic, K., Tolic, I.M., 2024. A kinetochore-centrosome feedback loop linking CENP-E and Aurora kinases controls chromosome biorientation and congression. bioRxiv 2023.10.19.563150. https://doi.org/10.1101/2023.10.19.563150

Vukušić, K., Tolić, I.M., 2022. Polar Chromosomes—Challenges of a Risky Path. Cells 11, 1531. https://doi.org/10.3390/cells11091531

Vukušić, K., Tolić, I.M., 2021. Anaphase B: Long-standing models meet new concepts. Semin Cell Dev Biol 117, 127–139. https://doi.org/10.1016/j.semcdb.2021.03.023

Walczak, C.E., Cai, S., Khodjakov, A., 2010. Mechanisms of chromosome behaviour during mitosis. Nat Rev Mol Cell Biol 11, 91–102. https://doi.org/10.1038/nrm2832

Wandke, C., Barisic, M., Sigl, R., Rauch, V., Wolf, F., Amaro, A.C., Tan, C.H., Pereira, A.J., Kutay, U., Maiato, H., Meraldi, P., Geley, S., 2012. Human chromokinesins promote chromosome congression and spindle microtubule dynamics during mitosis. J Cell Biol 198, 847–863. https://doi.org/10.1083/jcb.201110060

Wang, Q., Racowsky, C., Deng, M., 2011. Mechanism of the chromosome-induced polar body extrusion in mouse eggs. Cell Div 6, 17. https://doi.org/10.1186/1747-1028-6-17

Wang, W., Chen, L., Ding, Y., Jin, J., Liao, K., 2008. Centrosome separation driven by actin-microfilaments during mitosis is mediated by centrosome-associated tyrosine-phosphorylated cortactin. J Cell Sci 121, 1334–1343. https://doi.org/10.1242/jcs.018176

Waters, J.C., Skibbens, R.V., Salmon, E.D., 1996. Oscillating mitotic newt lung cell kinetochores are, on average, under tension and rarely push. J Cell Sci 109, 2823–2831. https://doi.org/10.1242/jcs.109.12.2823

Watson, E.R., Brown, N.G., Peters, J.-M., Stark, H., Schulman, B.A., 2019. Posing the APC/C E3 Ubiquitin Ligase to Orchestrate Cell Division. Trends Cell Biol 29, 117–134. https://doi.org/10.1016/j.tcb.2018.09.007

Weber, K.L., Sokac, A.M., Berg, J.S., Cheney, R.E., Bement, W.M., 2004. A microtubule-binding myosin required for nuclear anchoring and spindle assembly. Nature 431, 325–329. https://doi.org/10.1038/nature02834

Whitehead, C.M., Winkfein, R.J., Rattner, J. b., 1996. The relationship of HsEg5 and the actin cytoskeleton to centrosome separation. Cell Motility 35, 298–308. https://doi.org/10.1002/(SICI)1097-0169(1996)35:4<298::AID-CM3>3.0.CO;2-3

Wojcik, E., Basto, R., Serr, M., Scaërou, F., Karess, R., Hays, T., 2001. Kinetochore dynein: its dynamics and role in the transport of the Rough deal checkpoint protein. Nat Cell Biol 3, 1001–1007. https://doi.org/10.1038/ncb1101-1001

Wollman, R., Cytrynbaum, E.N., Jones, J.T., Meyer, T., Scholey, J.M., Mogilner, A., 2005. Efficient Chromosome Capture Requires a Bias in the 'Search-and-Capture' Process during Mitotic-Spindle Assembly. Current Biology 15, 828–832. https://doi.org/10.1016/j.cub.2005.03.019

Wong, Y.L., Anzola, J.V., Davis, R.L., Yoon, M., Motamedi, A., Kroll, A., Seo, C.P., Hsia, J.E., Kim, S.K., Mitchell, J.W., Mitchell, B.J., Desai, A., Gahman, T.C., Shiau, A.K., Oegema, K., 2015. Reversible centriole depletion with an inhibitor of Polo-like kinase 4. Science 348, 1155–1160. https://doi.org/10.1126/science.aaa5111

Woolner, S., O'Brien, L.L., Wiese, C., Bement, W.M., 2008. Myosin-10 and actin filaments are essential for mitotic spindle function. J Cell Biol 182, 77–88. https://doi.org/10.1083/jcb.200804062

Wu, G., Lin, Y.-T., Wei, R., Chen, Y., Shan, Z., Lee, W.-H., 2008. Hice1, a novel microtubule-associated protein required for maintenance of spindle integrity and chromosomal stability in human cells. Mol Cell Biol 28, 3652–3662. https://doi.org/10.1128/MCB.01923-07

Wulf, E., Deboben, A., Bautz, F.A., Faulstich, H., Wieland, T., 1979. Fluorescent phallotoxin, a tool for the visualization of cellular actin. Proc Natl Acad Sci U S A 76, 4498–4502. https://doi.org/10.1073/pnas.76.9.4498

Xie, L., Forer, A., 2008. Jasplakinolide, an actin stabilizing agent, alters anaphase chromosome movements in crane-fly spermatocytes. Cell Motility 65, 876–889. https://doi.org/10.1002/cm.20309

Ye, A.A., Deretic, J., Hoel, C.M., Hinman, A.W., Cimini, D., Welburn, J.P., Maresca, T.J., 2015. Aurora A Kinase Contributes to a Pole-Based Error Correction Pathway. Curr Biol 25, 1842–1851. https://doi.org/10.1016/j.cub.2015.06.021

Yi, K., Unruh, J.R., Deng, M., Slaughter, B.D., Rubinstein, B., Li, R., 2011. Dynamic maintenance of asymmetric meiotic spindle position through Arp2/3-complex-driven cytoplasmic streaming in mouse oocytes. Nat Cell Biol 13, 1252–1258. https://doi.org/10.1038/ncb2320

Yüce, O., Piekny, A., Glotzer, M., 2005. An ECT2-centralspindlin complex regulates the localization and function of RhoA. J Cell Biol 170, 571–582. https://doi.org/10.1083/jcb.200501097

Zhu, H., Coppinger, J.A., Jang, C.-Y., Yates, J.R., Fang, G., 2008. FAM29A promotes microtubule amplification via recruitment of the NEDD1-gamma-tubulin complex to the mitotic spindle. J Cell Biol 183, 835–848. https://doi.org/10.1083/jcb.200807046

Zupa, E., Würtz, M., Neuner, A., Hoffmann, T., Rettel, M., Böhler, A., Vermeulen, B.J.A., Eustermann, S., Schiebel, E., Pfeffer, S., 2022. The augmin complex architecture reveals structural insights into microtubule branching. Nat Commun 13, 5635. https://doi.org/10.1038/s41467-022-33228-6

# 8. AUTHOR BIOGRAPHY

Valentina Štimac was born in Rijeka, Croatia on June 14th, 1995. She graduated in 2019 from the Department of Biotechnology, University of Rijeka in Croatia and received her master's degree of Biotechnology in Medicine. She was part of the Laboratory for Molecular Immunology at the Department of Biotechnology where she worked on her master's thesis under the mentorship of Prof. Ivana Munitić. Since 2019, she has been employed as a research assistant at the Ruđer Bošković Institute in the Laboratory of Cell Biophysics under the mentorship of Prof. Iva Tolić and was concurrently enrolled in postgraduate studies Biology at the Faculty of Science, University of Zagreb in Croatia. To date, she has held 6 oral and 9 poster presentations either virtually or in person at 10 international conferences and workshops. At *Cell Bio|An ASCB|EMBO Meeting 2022* in Washington D.C., her talk was selected as one of 16 semi-plenary young scientists' talks from over 500 applicants. Valentina also received the L'Oréal-UNESCO National Program "For Women in Science" award for scientific achievements, the Branimir Jernej award for an outstanding article in the field of molecular biology, biomedicine or neuroscience, the annual Ruđer Bošković Institute award for the best scientific paper, and two scholarships to attend *Cell Bio|An ASCB|EMBO Meeting 2022*. She was also a visiting PhD student at the Danish Cancer Society Research Center in Copenhagen, a member of the organizing committee for Biophysics of Spindle Assembly workshop and took part in science outreach at Ruđer Bošković Institute Open Day.

**List of publications** (*equal contribution):

1. Koprivec, I.*, **Štimac, V.***, Mikec, P., Tolić, I.M. (2024). Microtubule pivoting driven by spindle elongation rescues polar chromosomes to ensure faithful mitosis. *bioRxiv*, 2024.06.16.599200
2. Koprivec, I.*, **Štimac, V.***, Tolić, I.M. (2024). Super-resolution imaging of mitotic spindle microtubules using STED microscopy. *Methods in Molecular Biology*, in press
3. **Štimac, V.***, Koprivec, I.*, Manenica, M., Simunić, J., Tolić, I.M. (2022). Augmin prevents merotelic attachments by promoting proper arrangement of bridging and kinetochore fibers. *eLife*, 11:e83287
4. Klaasen, S.J., Truong, M.A., van Jaarsveld, R.H., Koprivec, I., **Štimac, V.**, de Vries, S.G., Risteski, P., Kodba, S., Vukušić, K., de Luca, K.L., Marques, J.F., Gerrits, E.M., Bakker, B., Foijer, F., Kind, J., Tolić, I.M., Lens, S.M.A., Kops, G.J.P.L. (2022). Nuclear chromosome locations dictate segregation error frequencies. *Nature*, 607, 604–609.